Finite Element Representation of the EEG Forward Problem with Multipole Expansion

- Multipolentwicklung zur Lösung des EEG Vorwärtsproblems
mittels Finiter Elemente -

der Fakultät für Mathematik, Informatik und
Naturwissenschaften der Rheinisch Westfälischen Technischen
Hochschule Aachen zur Erlangung des akademischen Grades
Doktor der Naturwissenschaften im Fachgebiet Mathematik
vorgelegte Dissertation

von:

Anne Hanrath M.Sc RWTH,
aus Aachen

Aachen, 2018

Abstract

Brain activity imaging using Electroencephalography (EEG) is a vital aspect of cognitive science and neurology. However, the reliability of brain activity localization based on EEG data has been a hard endeavor so far. In this dissertation we propose a new, reliable mathematical algorithm for this purpose.

First, we will provide an overview over the biological background of methodology in cognitive science. To localize brain activity from EEG data, we need to solve an elliptic partial differential equation (PDE) with a mathematical dipole as a right–hand side. For this, we use Finite Element Methods (FEM). However, FE cannot discretize a mathematical dipole. We solve this issue with regularization.

Secondly, we list contemporary regularization approaches. The most successful one – the *Venant Approach* – has so far lacked a mathematical and theoretical foundation. This dissertation is expanding that approach both theoretically and practically.

Thirdly, we formulate a new approach using the idea of the *Venant Approach.* It originates from the idea to substitute the mathematical dipole with a distribution of monopoles. Monopoles are placed exactly on FE nodes, using the corresponding monopole loads as FE values.

The substitution of a mathematical dipole with a monopole distribution results in a new PDE. With assumptions for both monopole loads and electrical conductivity in the PDE, we prove that there is a unique solution for the PDE's ultra weak formulation using the duality method.

We can derive a more intuitive way to compute monopoles with the help of multipole expansion. This involves expanding the potential of the mathematical dipole and the potential of the monopole distribution, and comparing the different terms. This new approach is called *Multipole Approach.*

For the *Multipole Approach*, we can give an error bound with an error decay in direction of the boundary for a small sphere of unique conductivity around the dipole location.

Fourthly and finally, we employ the most popular approaches, together with the new Multiple Approach in numerical computations. First, we test with unique conductivity in 2D. Second, we employ the approaches on spherical models with different layers of distinct conductivity in 3D. Finally, we compute a goal function scan on one 3D spherical model.

We study the *Multipole Approach* in different configurations and find the optimal one. In this optimal case, the new approach outperforms the contemporary approaches effortlessly.

Acknowledgements

The process of writing this thesis was a little bit like working like a locust. I gathered all these intelligent and brilliant ideas from a lot of very intelligent and brilliant people and used their ideas, tweaked them, got some ideas here and there myself and applied this to my very own problem.
The whole work is written down here.
Nonetheless, there are people without whom I would not have started the journey of writing this thesis or been able to finish it.

- I would like to thank my supervisor and boss Lars Grasedyck, who offered me my position and helped me through ups and downs, but also always let me do my thing.

- I would like to thank the people of my research team, especially Carsten Wolters and Johannes Vorwerk.

- I would like to thank the people of my Institute; especially the people of my "Doktorarbeit-Selbsthilfegruppe": Angela Klewinghaus, Elisa Friebel, Valentina König and Felix Gruber, with whom I discussed this thesis for hours on end and who helped me stay on track. Moreover, I'd like to thank Felix Gruber for test reading and Johannes Stemick for many discussions about backgrounds, which helped me understand where I was heading

- I would like to thank Carolin Steiner, my diligent proofreader, who was not scared off by my bad english and corrected tirelessly the tons of errors, formulations and wrong commas.

- My heartfelt gratitude goes out to my parents, Petra and Wilhelm Hanrath, who have always been there for me. I additionally thank my Dad for taking the time to test-read my dissertation and discussing it with me

- Finally, I would like to thank the person, who might have suffered even more from me writing this thesis than I have: my husband, Dominic Portain, who helped me through all of it, who encouraged me when I was down, was always there for discussions, plans and in the end even helped me to improve my English - all while taking care of the household and our relocation to Sweden. I do not think I would have finished this without you.

Contents

1 Introduction **7**

1.1 A short summary of the functionality of the brain from a mathematician's perspective . . . 8

2 How to model biological processes in the mathematical world **15**

2.1 From mathematical theory to computer solvable problems – a short overview of the FEM theory . . . 18

2.1.1 Finite Element Methods . . . 18

2.2 Established methods for the regularization of the EEG/MEG forward problem . . . 22

2.2.1 *Subtraction* . . . 22

2.2.2 *Partial Integration* . . . 23

2.2.3 The original *Blurred Dipole* . . . 24

3 The *Principle of Saint Venant* and the multipole expansion **27**

3.1 Existence and uniqueness of a solution for the *Principle of Saint Venant* . . . 29

3.2 Choice of the monopole locations . . . 36

3.3 Multipole expansion to compute the strengths of the monopoles . . . 36

3.3.1 A computational algorithm . . . 39

3.4 Error estimation for the *Multipole Approach* . . . 42

4 Numerical experiments **47**

4.1 Experiments with uniform conductivity in 2D . . . 50

4.1.1 The sensitivity of the approaches with regard to the location of the dipole . . . 52

4.2 Experiments with four–layer sphere models . . . 55

4.3 A goal function scan - a manual inverse algorithm . . . 59

4.4 Pitfalls for Multipole computation . . . 65

4.4.1 The penalty weight and the number of neighbors in 2D experiments . . . 66

4.4.2 Forward experiments in 3D with the penalty term and the number of neighbours . . . 68

4.4.3 Goal function scan . . . 70

4.5 Results of numerical computations with the classical errors 75

5 Summary **83**

6 Appendix A: programming the algorithm **87**

6.1 Implementation in UG4 88

6.1.1 The class *dipole* 88

6.1.2 The class *Blurred_Disc* to compute the *Multipole* and the *Venant Approach* 89

6.1.3 The class *PI_Disc* to compute Partial Integration 90

6.1.4 Error computations with UG4 91

6.2 Implementation in Fieldtrip 91

7 Appendix B: *Adaptive Finite Element Methods* and the *Multipole Approach* **93**

7.1 Adaptive Experiments 96

7.1.1 Global refinement 98

7.1.2 Standard AFEM 98

7.1.3 Goal–oriented AFEM 99

7.1.3.1 Adjoint AFEM 100

7.1.3.2 Goal–oriented computations 102

7.1.4 Computing with a new right–hand side 105

7.1.5 Conclusion of the numerical experiments for the adaptive FE methods 106

1 Introduction

In the neurophilosophic discipline of naturalism the view has emerged that we humans are essentially a carbon based machine. In this context the prevalent opinion is that the neural nervous system is responsible for exerting all control over the human body [8], in which the brain acts as the most relevant control center of the nervous system.

The strongest argument for this idea is the sheer number of neurons: The human brain contains the vast majority of all neurons in the body. Since neurons are widely understood to be the source of complexity, we can limit our scope to this area.

Historically, the brain was studied by comparing head injuries to changes within the human nature. Famously, the personality of railroad worker Phineas Gage turned from very friendly to aggressive after suffering a head injury caused by an explosion [25].

However, the approach of studying injured or disordered brains is inherently limited. Our brain is segmented into different functional areas. Due to Neuroplasticity, neighbouring areas can partially replace missing functions. Additionally, injury of certain brain areas do not lead to change in behavior or personality [10]. Due to these limitations, cognitive science shifted towards studying healthy brains [29]. This approach led us to a deeper understanding of the function of individual brain areas.

One method to study brain activity involves the method of *Electroencephalography* (EEG). This approach exploits the electrochemical processes in active brain regions, recording electric field changes on the scalp. [59]

This EEG activity can be modeled by a *Partial Differential Equation* (PDE) [33]. Deducing the location of brain activity involves solving an inverse problem for this PDE. Solvers of this *Inverse Problem* rely on quick and efficient algorithms to solve the *Forward Problem* [34, 66, 65].

This thesis will improve one of such algorithms and is st as structured as follows. Chapter 1 gives an overview over the brain's localized structure. We introduce the mathematical model which describes the biological processes and we will present the central problem of this thesis, i.e. solving the EEG forward problem with *Finite Element Methods* (FEM). In Chapter 2 we provide a broad overview over previously established algorithms to solve the central problem. In Chapter 3, we dedicate ourselves to improve one of the already existing algorithms vastly, including mathematical analysis. Subsequently, in Chapter 4 we demonstrate experimental results, and come to a conclusion in Chapter 5.

1.1 A short summary of the functionality of the brain from a mathematician's perspective

The facts and mechanisms presented here are broad and are usually included in most basic neuroscience courses. Therefore, they can be researched in most basic textbooks such as for example [49, 78, 30, 25]

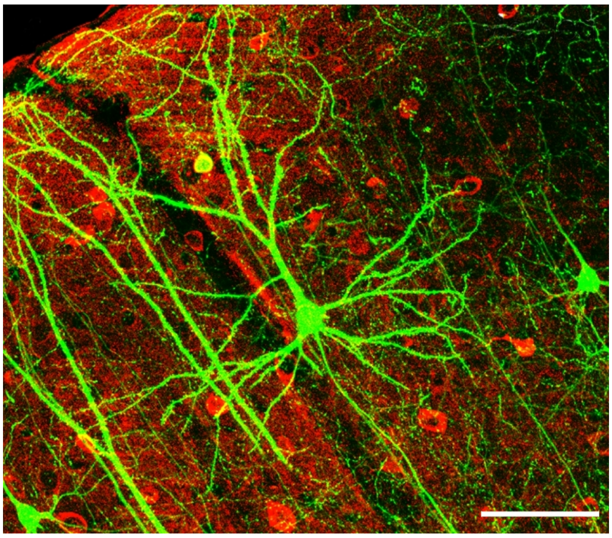

Figure 1.1: A neuron, scale bar: $100\mu m$ [42]. This neuron was made visible with a fluorescence staining method. With the help of this method, it becomes obvious that this neuron has a structure similar to a tree. The almond-shaped part at the top of the "roots" contains the cell core called *soma*. The neuron connects to other neurons via the "stem" and the "branches", which together are called *axon*. With the axon, a neuron can send information to its connected neurons. The information is then received by their so called *dendrites*. We can see the dendrites of the initial neuron as the "roots" in this picture.

The brain consists of 86±8 billion highly interconnected neurons that form strongly clustered and subclustered structures[1]. Each cluster has its own unique responsibility in processing information and controlling the body.

---

[1] Brain Science is speaking about areas instead of clusters. However, since the neurons in an area

The layout of the clusters and subclusters is not arbitrary. Instead, they show very similar patters in different humans. The only factor introducing a strong difference is a person's handedness (left–handed people have a different layout than right–handed people for example [4]). Thus identification of task responsibility of clusters and subclusters is not only possible in general, but also for every individual person.

Figure 1.2: Cytoarchitectonics of human brain according to Brodmann, picture from [17].

The most fundamental cluster structure is shared by virtually all humans and can be discovered by analyzing cortical tissue samples. Korbinian Brodmann examined such samples around 1910 under a microscope. On this base he was able to assemble a map of the cortex describing 52 distinct neuronal clusters [16]. These clusters usually appear in specific locations for every individual human, making Brodmann's map a useful general guide for brain organization.

In the years after Brodmann's discovery, suspicion arose that these different clus-

---

are clustered around each other, the word cluster illustrates what happens more accurately. Therefore, we choose to use this terminology ter types were responsible for distinct and specialized tasks. Several decades later, this suspicion was confirmed. The new field of cognitive science – functional neuroanatomy – was established to conduct research about the functions of specific neuronal clusters.

The established procedure for conducting this research required the test subjects to undergo conscious brain surgery. Then, a small electric current was sent through specific locations of the brain surface and the personal experiences of the experimental subject's response was recorded. Thus, one was able to approximate each cluster's tasks.

With time and more advanced methods, functional neuroanatomy researchers have developed a deeper and more refined understanding of the brain's architecture. Nowadays the cortical map comprises 100 distinct clusters and subclusters. However, this project is not yet complete and more research has to be done.

Modern research is aided by two characteristics of the brain's clusters: Firstly, two distinct clusters do not process the same information and secondly, each and every cluster and subcluster is only involved in a handful of specific tasks.

Therefore, by observing the activity in certain cluster during a wide range of states of the human body and mind we can deduct its functional role. This strong division of responsibilities allows different clusters to work together and accomplish a more complicated cognitive process.

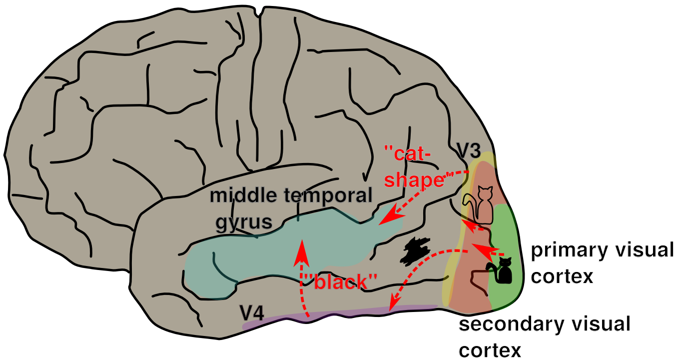

Figure 1.3: Example 1, areas active while identifying the visual stimulus of a black cat.

Example 1. *Suppose there would be a black cat sitting in front of a person.*
The eyes of the person resolve the light patterns into electrical impulses. This visual data is sent to a large cluster in the back of the of the brain, called primary visual cortex (V1).

The V1 will then apply a series of filtering and shape detection functions. Afterwards, it will send the information to the secondary visual cortex (V2)*, located in a broad ring around the V1.*

V2 disassembles the data into shape and color information and sends these data streams to the clusters V3 *and* V4. V3 *is located in the upper front of the V2 while V4 can be found on the lower rear of the brain.*

V4 is a cluster which can be compared to a general library of shapes. In our example, the visual data from V2 activates the subcluster for the shape of a cat. V3 is responsible for determining the color of an object. Again, in our example, the subcluster, which represents the color black, will be activated by the visual data.

The activity of V3 and V4 also activates another cluster, the middle temporal gyrus *(located in the middle of the lower part of the brain). This area receives both shape and color information, which are combined and in turn lead the the activation of a new subcluster. In our example this subcluster represents the generic visual image of a black cat. This is then the moment that the person has a conscious realization that the object in the visual field is, in fact, a real cat.*

Although this whole process happens very quickly and without conscious control, there are imaging techniques which can observe this sequential activities. In principle, if the role and location of each of a person's subclusters were completely known, we could identify the cat in front of this person without having any interaction with the person apart from scanning their brain.

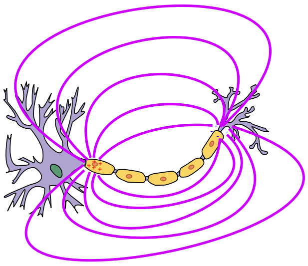

Figure 1.4: [23] The neurons undergo an electrochemical process, which includes electrons moving along the axon, such that an electric field is created.

The biggest obstacle for the research in functional neuroanatomy is that the brain does not process information sequentially. Instead, a large number of processes are active simultaneously all the time. Even when considering only sensory input, we see, hear, smell, taste, feel and think at the same time. The respective data streams produced by all these processes merge together into a chaotic and seemingly arbitrary pattern of activity that spans the whole brain.

Traditionally, this problem is mitigated by repeating the same experiment for multiple instances and with very little content variation. While the experiment is running as much brain activity as possible is recorded. If the experiment is well designed, the brain activity not related to the experiment will be random. Combining the information from all the individual runs then lets this random activity cancel itself out. Ideally, the important and experiment–related activity remains. This is called an evoked responses experiment.

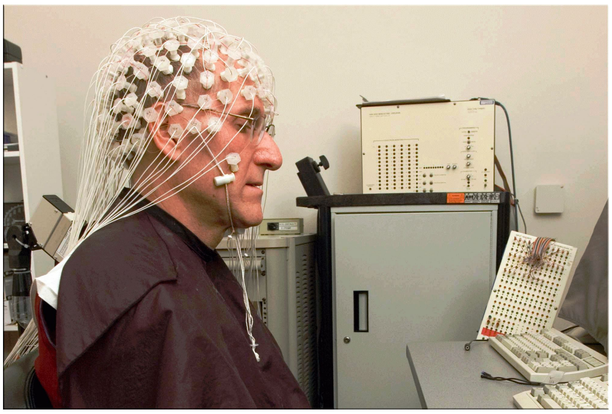

Figure 1.5: The EEG consists of an array of electodes, designed to capture electric fields from human scalps. This picture shows the buddhist monk Barry Kerzin meditating with an EEG on his head, picture from [48].

Two common devices for capturing neuronal activity are the *Electroencephalograph* (EEG) and the *Magnetoencephalograph* (MEG). They are based on measuring electrical fields and magnetic fields, respectively.

The process which helps the EEG and the MEG to be able to detect brain activity involves an electro–chemical process within active neurons. Every active neuron will emit an electric and a magnetic field. Neurons in a cluster are aligned such that the emitted fields will add to each other (called synchronization). This builds an electric and a magnetic field, which is strong enough to survive to the outside. Thus, it can be captured by an EEG or an MEG. Since MEG is a comparably rare technique, we will focus on EEG–based approaches.

The EEG consists of an array of conducting electrodes attached to a cap. This cap is connected to an amplifier and a digitizer, which is connected to a computer. When worn by a test subject, the electrodes make electrical contact with the scalp. The EEG then captures electric field changes on the scalp in quick succession, typically several thousand times per second. The recordings are digitized and sent to the computer for storage and analysis.

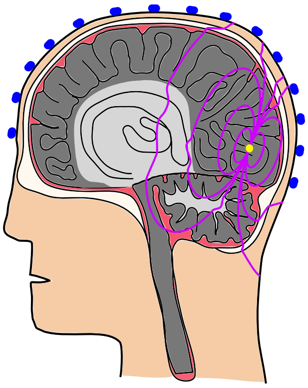

Figure 1.6: The electric field will get deformed on the way from the source to outside of the head. Especially the skull will dampen it enormously, original content.

Provided that the experimental design was successful in excluding non–task activity, directly deducing from the recorded information would only lead to a very rough localization of brain activity. The cause for this problem is that the EEG can only capture the electric field on the top of the human scalp. Active neuronal clusters usually produce an electric field, which would be – in principle – measurable with a simple pair of electrodes inside the head. However, when the electric field finally reaches the scalp, it has already been heavily distorted by the isolating skull layer. This means that the electric field gets dampened and squished and will be deformed when it reaches the sensor positions. Thus, localization of the source might not be so easy.

Therefore, we need a model for the conductivity in every point within the head. Usually those head models are made by using an MRI scan of the person's head. The images from the MRI are then converted into such a model by a software like BESA, Freesurfer or FSL.

To now compute the location of brain activity with the help of this head model and designed studies, we need a good and reliable algorithm. This algorithm will be the focus of the following chapters and the main focus of this dissertation.

Figure 1.7: The head of the participant will first be scanned with an MRI which results in a grayscale image. Then this image will be transformed into a computer–readable head model with layers. On the left–hand side we can see a so–called T1–weighted image of a slice of a head. On the right–hand side we can see a piece of the transformed head model with several layers in different colors. The images were given to me without any restrictions from Dominic Portain of the Max Planck Institute for Human Cognitive and Brain Sciences and display his head.

2 How to model biological processes in the mathematical world

We start off by describing a mathematical model for the electric and magnetic fields – and like almost every time connected electric and magnetic fields are described, the starting points are the famous Maxwell equations [50].

Figure 2.1: James Clerk Maxwell, 1831-1879, via [77].

These equations are a set of partial differential equations which – together with the Lorentz force law – are the base formulas of electrodynamics. They describe the relation between electric and magnetic fields and thus can be used in this context. We do not need to use these equations in their original form, as it is possible to simplify them [85, 33, 72, 15].
We have two preliminaries to consider:

1. **The domain** When we want to solve a mathematical formula, we need a domain on which we want to solve. In our case, we call the domain $\Omega \subset \mathbb{R}^3$. This domain is – in the context of the application – a representation of the head.

2. **The electric conductivity** For every point in our domain, we can define the electric conductivity tensor $\sigma(x)\colon \Omega \to \mathbb{R}^{3\times 3}$. We can assume that $\sigma(x)$ is symmetric, positive and bounded [85]. Moreover $\sigma(x) \in L_\infty(\Omega)$, where $L_\infty(\Omega)$ is the Lebesgue space for $p = \infty$ [3, 28] with

$$L_\infty(\Omega) = \{f : \Omega \to \mathbb{R} | f \text{ is Lebesgue measurable and essentially bounded}\}.$$

Definition 1. *(Preliminarities for the EEG inverse problem)*
Let $\Omega \subset \mathbb{R}^3$ be an open domain and $\partial\Omega := \bar{\Omega} \setminus \Omega$ be the border of Ω. Let $\partial\Omega$ be Lipschitz boundary [14]. Let $\sigma(x)\colon \Omega \to \mathbb{R}^{3\times 3}$ be a positive, symmetric and bounded function on Ω. Let $X_{sens} \subset \partial\Omega$ be a set of m discrete points on the border of Ω.

Then we can define the EEG inverse problem.

Problem 1. ***(The EEG inverse problem)***
Let Ω, σ and X_{sens} be like in Definition 1. Let the scalar potential be $u : \Omega \to \mathbb{R}$. Find the neuronal activity $J : \Omega \to \mathbb{R}$ which fulfills that

$$\begin{aligned} \nabla \cdot (\sigma \nabla u) &= J \, in \; \Omega \\ \sigma \nabla u \cdot n \quad &= 0 \; on \; \partial\Omega. \end{aligned} \tag{2.0.1}$$

Let $u|_{X_{sens}} := u_{sens}$ be given.

To solve this problem we have to overcome certain pitfalls until we reach the problem we actually want to solve.
First, this is an inverse problem. As opposed to forward problems, inverse problems are usually more complicated to solve.
However, the forward solutions of (2.0.1) are linear with regard to the neuronal activity, which can be exploited to compute inverse solutions.
Inverse solvers like MNE, LORETA, sLORETA and HBM [34, 66, 65, 47] do exactly this. Using those, we mostly solve the inverse problem as follows:

1. In the first step, we place numerous different dipole locations in the brain area. Then we compute the forward solutions at those locations for the unit vectors as moments. The solutions get saved mostly within a so–called lead field matrix and can be computed within an offline step. This is convenient since this is the part with significant computational costs.

2. In the second step, the algorithm then cleverly computes the most fitting constellation of brain activity locations among those already computed solutions. The algorithm therefore uses the lead field matrix and the measured values from the sensors u_{sens}.

The existing solvers differ most during the second step, but they all need a good, quick and smooth forward problem solver.
It therefore makes sense for us to optimize the computations for the forward problem.

Problem 2. ***(The EEG Forward problem)***
Let $\Omega \in \mathbb{R}^3$ *and* $\sigma(x)\colon \Omega \to \mathbb{R}^{3\times 3}$ *be like Definition 1. The EEG forward problem is to find the scalar potential* $u : \Omega \to \mathbb{R}$ *which solves the equation*

$$\begin{aligned} \nabla \cdot (\sigma \nabla u) &= J \, in \, \Omega \\ \sigma \nabla u \cdot n \quad &= 0 \, on \, \partial\Omega. \end{aligned} \tag{2.0.2}$$

where J *is the model for the given neuronal activity in the brain.*

Realistically, the left–hand side of (2.0.2) portrays the flow of the electrical field. The right–hand side portrays the influence on this flow by neuronal activity.
In 1988, de Munck, van Dijk, and Spekreijse, showed [57] that the model of a *mathematical dipole* is sufficient as a model for the right hand side. In contrast to a mathematical dipole, the biological electrical source has a physical extend and is no point singularity. However, the neurons in a subcluster are aligned in such a way that using a mathematical dipole as a model for this is an appropriate approximation. Until now, this has been working well in practical applications.
The *mathematical dipole* is a point source with a location and a direction and can be described mathematically as a directional derivative of a Dirac delta distribution, which can be written sloppily as

$$\delta_y(x) := \begin{cases} \infty, & x = y \\ 0, & \text{otherwise.} \end{cases}$$

Let x_0 be the location of the dipole and its direction, the so–called moment $\overrightarrow{M} \in \mathbb{R}^3$. Then the dipole is

$$J(x) = \nabla \cdot (\overrightarrow{M} \, \delta_{x_0}(x)). \tag{2.0.3}$$

Other possible models for the right hand side exist, such as the *Feynman Dipole* [62], which is composed of two monopoles of opposite, but same absolute strength with a small distance to each other:

$$J_{Fey}(x) = (q\delta_{x_+}(x) - q\delta_{x_-}(x)),$$

where $x_+ \in \Omega$ and $x_- \in \Omega$ are the locations of the source, respective sink.

Both dipole models are not in $L_2(\Omega)$, which is the Lebesgue space for $p = 2$ [3, 28], with

$$L_2(\Omega) := \{f : \Omega \to \mathbb{R} | f \text{ is Lebesgue measurable and } \left(\int_\Omega |f|^2\right)^{1/2} \leq \infty\}$$

This usually is a problem for standard FEM theory. We will later see how to work around this.

2.1 From mathematical theory to computer solvable problems – a short overview of the FEM theory

Like with many problems arising from real world applications, we cannot compute a solution for the EEG forward problem analytically simply because it does not exist in the sense of an analytical formula.

Therefore, an approximation to the real solution can be satisfactory, provided the approximation fulfills certain criteria – like having a good error bound.

The still most often used approach is a three or four compartment *Boundary Element Method* (BEM) approach [40, 75]. In BEM, most often nested compartments of isotropic conductivity are assumed, but newest investigations showed that BEM can also offer more flexibility, e.g. with regard to junctions [74, 41]. However, BEM have shortcomings, namely that they have difficulties with the anisotropy within the white matter compartment and with modeling the folded brain surface. Therefore, the usage of FEM can be beneficial to bypass those specific shortcomings of BEM altogether.

FEM do not have any requirements for the different electrical conducting layers and are suitable for anisotropic conductivity. However, applying FEM to the EEG/MEG forward problem also requires tricks, which are already commonly applied.

2.1.1 Finite Element Methods

We only want to provide a short overview of the fundamentals of FEM. For a deeper understanding of general FEM good text books are available such as for example [20, 14, 27, 63, 12, 13].

For the purpose of this chapter we consider a general linear elliptic equation. We will discuss the differences to the EEG forward problem (2.0.2) and the arising difficulties for the FE Ansatz in the end.

Problem 3. *Testproblem*
Let Ω be an open domain and $\sigma : \Omega \to R$ be positive and bounded. Find $u : \Omega \to R$

which solves

$$\begin{aligned} \nabla \cdot (\sigma \nabla u) &= f \, in \; \Omega \\ \sigma \nabla u \cdot n &= 0 \, on \; \partial\Omega. \end{aligned} \tag{2.1.1}$$

for $f \in L_2(\Omega)$.

The next step is to weaken the idea of a solution. This idea is realized with a *variational formulation.*

FE spaces are often defined in the context of *Sobolev Space*s [3, 28]. This theory is based on the idea of weak derivatives. Let $L^1_{loc}(\Omega)$ be the space of locally summable functions [28].

Definition 2. *weak derivative,([28], (5.2.1))*
Suppose $u, v \in L^1_{loc}(\Omega)$ *and* $\alpha = (\alpha_1, \ldots, \alpha_n)$ *is a multi–index of order* $|\alpha| = \alpha_1 + \ldots + \alpha_n = k$. *We say that* v *is the* α*th-weak partial derivative of* u, *written*

$$D^\alpha u = \frac{\partial^{\alpha_1}}{\partial x_1^{\alpha_1}} \cdots \frac{\partial^{\alpha_n}}{\partial x_1^{\alpha_n}} u = v, \tag{2.1.2}$$

provided

$$\int_\Omega u D^\alpha \phi dx = (-1)^{|\alpha|} \int_\Omega v \phi dx \tag{2.1.3}$$

for all test fuctions $\phi \in C_c^\infty(\Omega)$.

Here, $C_c^\infty(\Omega)$ is the space of all infinitely differentiable functions with compact support in Ω.

A *Sobolev Space* is then defined as

Definition 3. *Sobolev Space, ([28],(5.2.2))*
The Sobolev Space $W^{k,p}(\Omega)$ *consists of all locally summable functions* $f : \Omega \to R$, *such that for each multi–index* α *with* $\alpha < k$, $D^\alpha f$ *exists in the weak sense, and belongs to* $L^p(\Omega)$.

Remark 1. *([28],(5.2.2)(i))*
We can use the notion $H^k(\Omega) = W^{k,2}(\Omega)$.

We use the Standard *Sobolev Space* $H^1(\Omega)$.

We define a test space V as a subset of this Sobolev Space with

$$V := \{v \in H^1(\Omega) | \nabla \cdot (\sigma \nabla v) \in H^1_0(\Omega) \text{ and } \sigma \nabla v \cdot n = 0 \text{ on } \partial\Omega\}.$$

This test space is only used for theoretical purposes. We can show that by using this test space we have nice properties for the EEG/MEG forward problem. Later, for experimental purposes, we will use a test space with fewer constrains.

Let $v \in V$. To obtain a variational formulation of (2.1.1) we then multiply both sides of the first equation of (2.1.1) with v and integrate over Ω.
On the left hand side we use Green's Formula [20] and the natural boundary data to acquire

$$\begin{aligned}\int_\Omega \nabla \cdot (\sigma \nabla u) v dx &= \int_\Omega \sigma \nabla u \nabla v dx - \int_\Omega \sigma \nabla u \cdot n dx \\ &= \int_\Omega \sigma \nabla u \nabla v dx.\end{aligned}$$

This is a bilinear form. If we use the $\sigma(x)$ of assumptions 1, we can assume that it is positive, symmetrical and bounded. Therefore, we obtain a bounded, and thus, continuous and coercive linear form [14].
For the right–hand side we get

$$\langle f, v\rangle = \int_\Omega f v dx$$

which yields a linear functional, if $f \in L_2(\Omega)$.
The next step is then to solve the variational formulation instead of the original problem (2.1.1). For theoretical purposes, the solution u should be the element of $H^{-1}(\Omega)$ which is the dual to the space $H^1_0(\Omega) := \{f \in H^1(\Omega) | f|_{\partial\Omega} = 0\}$ [3, 28]. This function space is rather big and it might seem to be unnecessarily big at first glance. However, we will in further theoretical analysis see that this is required. For now we just want to find a $u \in H^{-1}(\Omega)$ which fulfills

$$\int_\Omega \sigma \nabla u \nabla v dx = \int_\Omega f v dx$$

for any $v \in V$.
Due to the *Neumann Boundary Conditions*, this problem does not have a unique solution. If a solution exists, it is unique up to a constant.
To ameliorate this, we introduce a function $\eta \in H^1_0(\Omega)$ with $\int_\Omega \eta dx = 1$ and want u to fulfill $\int_\Omega \eta\ u\ \ dx = 0$.
The variational formulation will give us the so–called weak solution

Problem 4. *Find* $u \in \{v \in H^{-1}(\Omega) | \int_\Omega \eta v dx = 0\}$*, such that*

$$\int_\Omega \sigma \nabla u \nabla v dx = \int_\Omega f v dx \textit{ for any } v \in V.$$

This problem 4 can be understood as a problem with a bilinear form

$$a(u,v) = \int_\Omega \sigma \nabla u \nabla v dx \text{ for } u \in \{v \in H^{-1}(\Omega) | \int_\Omega \eta v dx = 0\}, v \in V \tag{2.1.4}$$

on the left–hand side and a functional

$$l(v) = \int_\Omega f v dx \tag{2.1.5}$$

on the right–hand side. We can conclude with [13] that every solution of the original forward problem (2.1.1) is a solution of problem 4 as well. Therefore, one solves only problem 4.
Nevertheless, we know from the Lax-Milgram-Lemma [20] or also called Lax-Milgram-Theorem [14] that there exists a solution and is unique if $f \in L_2(\Omega)$ (which then means that the solution is in $H^1(\Omega)$).

Theorem 1. *(Lax-Milgram ([14],(2.7.7)))*
Given a Hilbert space $(V, (\cdot, \dot{}))$, a continuous and coercive bilinear form $a(\cdot,\cdot)$ and a continuous linear functional $F \in V'$, there exists a unique $u \in V$ such that

$$a(u,v) = F(v) \text{ for all } v \in V.$$

Originally, we wanted to find a solution within the space $\{v \in H^{-1}(\Omega) | \int_\Omega \eta v \, dx = 0\}$. Since an analytical solution does not exist within this space, we need an approximation.

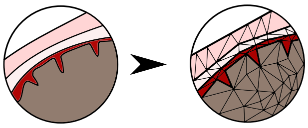

Figure 2.2: Sketch of an exemplary discretization of a small 2D portion of a head model.

Therefore, we define a sequence of discretizations of the domain Ω as $\Omega_{h_1}, \Omega_{h_2}, \ldots$ with hexahedra or tetrahedra. We can create $\Omega_{h_{n+1}}$ from Ω_{h_n} by refining all hexahedra or tetrahedra uniformly. h_n ($n \in \mathbb{N}$) is the indicator of the elements' diameter in the discretization and $h_n \to 0$ for $n \to \infty$. On each discretization we then define the FE space $\mathbb{X}(\Omega_{h_n}), n \in \mathbb{N}$. On each of those $n \in \mathbb{N}$ discretizations we then can solve 2.1.4 and thus get a solution $u_{h_n} \in \mathbb{X}(\Omega_{h_n}), n \in \mathbb{N}$.
Now we call the process *Finite Element Method* to compute the approximations $u_{h_n} \in \mathbb{X}(\Omega_h)$ with $u_{h_n} \to u$ for $h_n \to 0$. We can conclude this due to theorems which embed Sobolev Spaces into each other [28].

Unfortunately, we can not employ this scheme directly to the EEG forward problem since the right–hand side is too complicated.
The model for the neuronal activity (2.0.3) is a mathematical dipole, which means that $J(x) \notin L_2(\Omega)$. Therefore, we cannot do a variational formulation as described above. We need a regularization first, such that FE Methods becomes possible.

2.2 Established methods for the regularization of the EEG/MEG forward problem

Different methods are already in use for regularizing the dipolar right–hand side to make it suitable for FEM – each with its own drawbacks.
Here, we shall concentrate on the most popular methods, namely the *Subtraction Approach*, the *Partial Integration Approach* and the *Blurred Dipole Approach*. Recently, the *Blurred Dipole Approach* was called the *Venant Approach* or *St. Venant Approach*.
Admittedly, there are other interesting methods that are not used as often, such as discretizations with spline interpolation [39].

2.2.1 *Subtraction*

The *Subtraction Approach* is the best performing and mathematically best understood approach [44, 85, 88, 26].
For uniform conductivity, problem 2 has an analytical solution.
Let $\sigma_0 = \sigma(x_0)$ be the constant conductivity around the dipole at location $x_0 \in \Omega$ which fulfills that $\sigma(x) = \sigma_0$ for $x \in B_{r_0}(x_0)$. $x \in B_{r_0}(x_0)$ is the ball of radius $r_0 \in \mathbb{R}^+$ around the dipole location x_0. For $\Omega \subset \mathbb{R}^3$ the function

$$u_0(x) = \frac{1}{4 * \pi * \sqrt{\sigma_0}} \cdot \frac{\langle M, \sigma_0^{-1}(x_0 - x)\rangle}{\langle \sigma_0^{-1}(x - x_0), (x - x_0)\rangle^{3/2}}$$

fulfills that

$$\nabla \cdot (\sigma \nabla u_0) = J \text{ in } B_{r_0}(x_0).$$

Therefore, within $B_{r_0}(x_0)$, we can split the solution u of (2.0.2) into

$$u = u_0 + u_{\text{corr}}.$$

Then we can subtract the solution u_0 from the whole problem (2.0.2) (hence the name) and get a partial differential equation for u_{corr}, which is

$$\begin{aligned} \nabla \cdot (\sigma \nabla u_{\text{corr}}) &= \nabla \cdot ((\sigma_0 - \sigma)\nabla u_0) && \text{in } \Omega \\ \langle \sigma \nabla u_{\text{corr}}, n\rangle &= -\langle \sigma \nabla u_0, n\rangle && \text{on } \partial\Omega \end{aligned} \tag{2.2.1}$$

Since $\sigma_0 = \sigma(x)$ for all elements in $B_{r_0}(x_0)$, the right–hand side vanishes at the critical points and therefore the partial differential equation can be solved for u_{corr} with standard FE Solvers.
After computing u_{corr}, we compute the wanted solution u by adding u_0 to u_{corr}. This approach is very accurate, since it only depends on the approximation which we compute in 2.2.1.
The new right–hand side fulfills that $\nabla \cdot ((\sigma_0 - \sigma)\nabla u_0) \in L_2(\Omega)$, so standard FE theory will guarantee good approximation results.
Also, the convergence rate on simple volume conductor models with uniform conductivity for this approach is quadratic for linear FE, which is the best convergence rate one can expect [88].
Even if those theoretical results are very promising, the *Subtraction Approach* has disadvantages when used in practice.
One drawback is that the smaller the radius r_0 gets, the less regularization can be achieved [44]. However, the biological structures in the brain allow layers of differing electrical conductivity in areas where neurons are located. Therefore, this method might be less accurate by design.
The major disadvantage of this approach is that it generates many entries in the FE Matrices. This will lead to rather long computational times. Thus, the approach is not practical for computations on finer grids, as will be necessary for the EEG forward problem.
Therefore, in practice one chooses approaches which have a lower computational time than the *Subtraction Approach.*

2.2.2 *Partial Integration*

The *Partial Integration Approach* is a direct approach using integration by parts [79, 70].
In this approach we use the standard FE approach to get a weak formulation and multiply both sides of (2.0.2) with the FE Basis Functions and integrate.
We thus obtain

$$\int_\Omega \nabla \cdot (\sigma(x)\nabla u)\varphi_i \, dx = \int_\Omega \nabla \cdot (\overrightarrow{M} \, \delta_{x_0}(x))\varphi_i \, dx.$$

There we can integrate, use Green's Theorem and apply the boundary conditions, which yields

$$\int_\Omega \sigma(x)\nabla u \nabla\varphi_i \, dx = \int_\Omega (\overrightarrow{M} \, \delta_{x_0}(x))\nabla\varphi_i \, dx.$$

For the right–hand side we can then observe that

$$\int_\Omega (\overrightarrow{M} \, \delta_{x_0}(x))\nabla\varphi_i \, dx = \langle M, \nabla\varphi_i(x_0)\rangle.$$

We can use this identity as the discretization of the right–hand side and have

$$(f_h)_i = \begin{cases} \langle M, \nabla\varphi_i(x_0)\rangle, & \text{if } x_0 \in \operatorname{supp}(\varphi_i) \\ 0, & \text{else} \end{cases} .$$

The weak formulation of this ansatz has a unique solution in $L_q(\Omega)$ for $1 \leq q < \frac{3}{2}$ under the condition that the electric conductivity fulfills the condition that $\sigma(x) \in W^{1,\infty}(B_{r_0}(x_0))$ [79][1].

In experiments this ansatz will lead to rather sparse right–hand sides, because there are just 4 FE nodal functions for tetrahedral meshes where the dipole lies in the support. This means computational costs are rather low.

This ansatz has linear convergence rates for uniform conductivity, which we will later on see in experiments and is suitable for *Adaptive Finite Elements*, but mostly in 2D [70].

2.2.3 The original *Blurred Dipole*

The *Blurred Dipole* was first described by [18] under the name of *Blurred Dipole Approach* but was renamed and is currently better known under the name *Venant Approach* or *St Venant Approach* [43, 86, 87, 53]. The basic idea is to substitute the dipolar right–hand side with a distribution of monopoles. Since this dissertation is dedicated to improving this ansatz, a deeper explanation is given in Chapter 3.

The idea to use different monopoles to describe another load combination is not new. In the theory of elasticity the *Principle of Saint Venant* does exactly this [71]. It says: Statically equivalent loads have very similar effects and become more and more alike the further away from the sources the observer is. It is commonly used in the context of electrostatics in the context of PDEs [54, 46].

Let there be $n \in \mathbb{N}$ monopole locations, which we will name $x_1, \ldots, x_n$. Those positions are chosen dependent on the FE grid. x_1 is the node nearest to the dipole location x_0. $x_2, \ldots, x_n$ are those nodes connected to x_1 sharing either an edge or a face or a volume.

Then for each monopole we assign a strength $q_1, \ldots, q_n$. Those numbers $q_1, \ldots, q_n$ are computed with a linear system of equations.

For each dimension $l = 1, 2, 3$ the $q_1, \ldots, q_n$ have to fulfill the conditions

$${}^{l}(T)_j = \sum_{i=1}^{n} ((x_i - x_0)_j)^l q_i, \quad j = 1, 2, 3$$

where ${}^{l}(T)_j$ is defined as ${}^{0}T = \overrightarrow{0}, {}^{1}T = \overrightarrow{M}$ and ${}^{2}T = \overrightarrow{0}$.

---

[1] $W^{1,\infty}(B_{r_0}(x_0))$ is a Sobolev Space defined along [28]

Then a Tikhonov-regularization is done as is common in solving inverse problems [45]. By doing this, a penalty term is added to ensure stability. This penalty term has the form

$$\lambda^2 \left\| \begin{pmatrix} \mathrm{diag}(|x_{1,1}|, \cdots, |x_{n,1}|) \\ \mathrm{diag}(|x_{1,2}|, \cdots, |x_{n,2}|) \\ \mathrm{diag}(|x_{1,3}|, \cdots, |x_{n,3}|) \end{pmatrix} \cdot \overrightarrow{q} \right\|_2^2 \to \min$$

for a certain $\lambda \in \mathbb{R}$, which can be chosen arbitrarily.
The conditions and the penalty term together can be solved with common linear equation solvers.
In [81] we can find a more detailed explanation of this approach. It is often considered to be a very good source modeling approach for the EEG and MEG forward problem [43, 86, 87].
The *Venant Approach* was used in some forward and inverse studies [84, 19, 22, 82, 51]. Here, the approach had to deal with artifacts, but yielded the best results.
The main part of this dissertation is dedicated to deducting the approach from the very first step and to improving the algorithm.
We will prove that the PDE with the new right–hand side has a unique solution in certain function spaces and will improve the computations of the $q_1, \ldots, q_n$ such that those artifacts vanish.

3 Everything looks the same from far away - The *Principle of Saint Venant* and the multipole expansion

So far, one of the best regularizations used in practice – the blurred dipole – centers around the idea that from far away there are several possible sources which can emit an electric field similar enough to the one emited by a mathematical dipole source. The idea to substitute the mathematical dipole with a monopole distribution is a better approximation of the reality than the mathematical dipole. The mathematical dipole is a model which is used because it proved to be good enough [57] – however, there is no mathematical dipole in the brain. Instead, there are active neurons organized within clusters which all undergo electrochemical processes. Thus, a monopole distribution could be an appropriate way to adapt the dipole to the biological process.
We begin by repeating the problem we are working on.
Problem 2. (The EEG Forward problem, repetition)
Let $\Omega \in \mathbb{R}^3$ *and* $\sigma(x)\colon \Omega \to \mathbb{R}^{3\times 3}$ *be like Definition 1. The EEG forward problem is to find the scalar potential* $u : \Omega \to \mathbb{R}$ *which solves the equation*

$$\begin{aligned} \nabla \cdot (\sigma \nabla u) &= J \, in \, \Omega \\ \sigma \nabla u \cdot n \quad &= 0 \, on \, \partial\Omega. \end{aligned}$$

where there exists a $x_0 \in \Omega$ *and a* $\overrightarrow{M}$ *such that*

$$J(x) = \nabla \cdot (\overrightarrow{M} \, \delta_{x_0}(x)).$$

For the purpose of this chapter, we put the dipole into a fixed location.

Assumption 1. *Let the dipole location be the origin:*

$$x_0 = \begin{pmatrix} 0 \\ 0 \\ 0 \end{pmatrix}$$

Remark 2. *Of course, we cannot always assume that the dipole is located at the origin, since this is also dependent on the coordinate system we choose. However,* *in case that the location of the dipole is not the origin, we could transform the coordinates such that the dipole is in the origin of the newly chosen coordinate system.*

We then choose a number of monopoles.

Assumption 2. *Let* $n \in \mathbb{N}$ *be fixed. Let* $x_1, \dots, x_n \in \Omega$ *be fixed. Additionally, we have* $q_1, \dots, q_n \in \mathbb{R}$.

The model of the activity caused by this monopole distribution can then be described by

$$J_{\text{monopoles}}(x) = \sum_{i=1}^{n} q_i \delta_{x_i}(x). \tag{3.0.1}$$

Substituting J with the $J_{\text{monopoles}}$ yields the new problem.
The idea to use multipole expansion to represent point charges is not new. In the context of atomistic modeling and simulation methods this method is called *Optimal Point Charge Approximation* [5, 37].
In the context of solving the EEG/MEG forward problem, however, this approach is new. Therefore, we will call it *Multipole Approach* to distinguish it from the already existing *Venant/Blurred Dipole Approach.*

Problem 5. *(***The Multipole forward problem***)*
Let $\Omega \in \mathbb{R}^3$ *and* $\sigma(x)\colon \Omega \to \mathbb{R}^{3\times 3}$ *be like Definition 1. Find the scalar potential* $u : \Omega \to \mathbb{R}$ *which solves the equation*

$$\begin{aligned} \nabla \cdot (\sigma \nabla u) &= \sum_{i=1}^{n} q_i \;\; \delta_{x_i}(x) \;\; \textit{in } \Omega \\ \sigma \nabla u \cdot n \quad &= 0 \qquad\qquad\quad \textit{on } \partial\Omega. \end{aligned} \tag{3.0.2}$$

There are several questions to answer before we can start to solve the problem using FEM.

1. **Solution**: Does a (weak) solution to Problem 5 exist? Is the solution unique? And in which function spaces does the solution lie?
2. **Computation**: How should one choose $n \in \mathbb{N}$, $x_1, \dots, x_n \in \Omega$ and how should we compute the $q_1, \dots, q_n \in \mathbb{R}$?
3. **Accuracy**: How good is the substitution of using a monopole distribution instead of a mathematical dipole?

Whereas the answer to [**Solution**] is independent of the choice of the monopole locations, we can only deduct the [**Accuracy**], if we know how to do the [**Computation**].

3.1 Existence and uniqueness of a solution for the *Principle of Saint Venant*

Before we get to the explanation on how to choose the monopoles, it is important to prove the existence and the uniqueness of a solution for this problem.

The final goal is to do FE. Therefore, the interesting question is whether this solution exists in such a way that we can approximate it with FE.

The answer to this lies in the (ultra-)weak solution for the problem, which we will see later.

Let the following condition hold for the weights of the monopole distribution:

Assumption 3. *Let* $q_1, \dots, q_n$ *fulfil*

$$\sum_{i=1}^{n} q_i = 0.$$

This condition will ensure the compatibility condition of the Neumann Problem later on.

Let there be a subdomain $B \subset \Omega$, which fulfills the weak cone property [2] and $\bigcup_{i=1}^{n} B_{r_i}(x_i) = B \subsetneq \Omega$. Additionally we assume that $B_{r_i} \cap B_{r_j} = \emptyset$ for $i \neq j$

To simplify, let

$$B_i := B_{r_i}(x_i). \tag{3.1.1}$$

Consider the linear space

$$X := \{\psi_k \in H^1(\Omega) \mid \psi_k \in H^3(B) \cap C^0(B) \text{ and } \langle(\sigma \nabla \psi_k), n\rangle = 0 \text{ on } \partial\Omega\} \tag{3.1.2}$$

with constant σ on $\partial\Omega$ ($H^1(\Omega), H^3(B), C^0(B)$ according to [28]). Our goal will be that this space is a test space for the FE. So far it has not been motivated, but we will need these properties of the space later on. Therefore, it is already defined here.

As a first step we bring the equation (3.0.2) into a(n ultra–)weak formulation and multiply both sides by $\varphi \in X$ and integrate over Ω. Then we apply the Gauss–Green Theorem [28] for integration twice. The border integrals vanish both times, $\int_{\partial\Omega}(\sigma\nabla u)\ n\ \varphi\ dx = 0$ because of the definition of problem (3.0.2) and $\int_{\partial\Omega}(\sigma\nabla\varphi)\ \cdot$

$n \cdot u dx = 0$ because of the definition of X. So we get that

$$\begin{aligned}\int_\Omega \nabla \cdot (\sigma \nabla u)\ \varphi\ \ dx &= -\int_\Omega \sigma\ \nabla u\ \nabla \varphi\ dx + \int_{\partial\Omega} (\sigma \nabla u)\ n\ \varphi\ dx \\ &= -\int_\Omega \sigma\ \nabla u\ \nabla \varphi\ dx \\ &= \int_\Omega u\ \nabla \cdot (\sigma \nabla \varphi)\ dx + \int_{\partial\Omega} (\sigma \nabla \varphi)\ n\ u\ dx \\ &= \int_\Omega u\ \nabla \cdot (\sigma \nabla \varphi)\ dx.\end{aligned}$$

On the right–hand side we multiply with $\varphi \in X$ as well and integrate over Ω to obtain

$$\int_\Omega \sum_{i=1}^n q_i\ \delta_{x_i}(x)\varphi(x)dx = \sum_{i=1}^n q_i \varphi(x_i)$$

because the integrals are finite and $\varphi \in C^0(B_{r_i}(x_i))$ for all $i \in \{1, \ldots, n\}$.
Since the problem (3.0.2) has pure Neumann data, the solution cannot be unique. This is fixed with a third condition.
We introduce a function $\eta \in H_0^1(\Omega)$ with $\int_\Omega \eta dx = 1$ and want u to fulfill $\int_\Omega \eta\ u\ \ dx = 0$.
The (ultra) weak formulation is then to find a $u \in H^{-1}(\Omega)$, such that

$$\begin{aligned}\langle u, \nabla \cdot (\sigma \nabla \varphi)\rangle &= \sum_{i=1}^n q_i \varphi(x_i) \\ \langle \eta, u\rangle &= 0.\end{aligned} \tag{3.1.3}$$

Theorem 2. *Let assumption 3 hold. Then there exists a solution u of* (3.1.3). *Moreover, $u \in L^q(\Omega)$ for $1 \leq q \leq 2$.*

The proof is analogous to the proof of existence and uniqueness of the solution of the subtraction approach [79]. The idea remains the same, namely to use the duality method. We will construct a dual problem and proof that the solution of the dual problem has the required traits. However, since we have a different problem, we have to use slightly different sources in standard literature to verify our claims.

Proof. Our first step is to generate a sequence of functions whose limit is the *Dirac Delta Distribution.* Therefore, let $\delta_{i_k} \in C_0^\infty(B_i)$ (B_i as defined in (3.1.1)), $\delta_{i_k} \geq 0$, $\int_\Omega \delta_{i_k} dx = 1$ and $\int_\Omega \delta_{i_k} \psi_k dx \to \psi(x_i)$ for $\psi \in C_0^\infty(\Omega)$([28]), $i = 1, ..., n$ and $k \in \mathbb{N}$ and supp $\delta_{i_{k+1}} \subsetneq$ supp δ_{i_k}.

Consider the new elliptic Neumann problem: Find $u_k \in H^1(\Omega)$ such that

$$\begin{aligned} \nabla \cdot (\sigma \nabla u_k) &= \sum_{i=1}^{n} q_i \, \delta_{i_k}(x) && \text{in } \Omega \\ \sigma \nabla u_k \cdot n &= 0 && \text{on } \partial\Omega, \\ \int_\Omega u_k \eta dx &= 0. \end{aligned} \tag{3.1.4}$$

This problem is well–posed and it fulfills the compatibility condition [28], which is

$$\int_\Omega \sum_{i=1}^{n} q_i \delta_{i_k} dx = \sum_{i=1}^{n} q_i \int_\Omega \delta_{i_k} dx = \sum_{i=1}^{n} q_i \underbrace{=}_{\text{Assumption 3}} 0.$$

Therefore, a solution exists [28] and we use $H^1(\Omega)$ functions for the weak ansatz. We then have

$$\int_\Omega u_k \, \nabla \cdot (\sigma \nabla \varphi) dx = \sum_{i=1}^{n} q_i \varphi(x_i).$$

The proof uses the u_k–duality product, which is comprised of the product with the dual to u_k, which we call ψ_k.

Therefore we define a new problem (why exactly this problem will be seen later on). Let $\psi \in H_0^1(\Omega)$. Then find $\hat{\varphi}$ which solves the problem

$$\begin{aligned} \nabla \cdot (\sigma \nabla \hat{\varphi}) &= \psi_k - \eta \int_\Omega \psi_k dx && \text{in } \Omega \\ \langle \sigma \nabla \hat{\varphi}, n \rangle &= 0 && \text{on } \partial\Omega, \\ \int_\Omega \hat{\varphi} dx &= 0. \end{aligned} \tag{3.1.5}$$

The solution $\hat{\varphi}$ exists and is unique, because (3.1.5) fulfills the compatibility condition [28]

$$\int_\Omega \psi_k dx - \left(\int_\Omega \psi_k dx \right) \eta = \int_\Omega \psi_k dx - \left(\int_\Omega \psi_k dx \right) \int_\Omega \eta dx = 0 = \int_{\partial\Omega} 0 dx.$$

If $\hat{\varphi} \in X$, then it is a sufficient test function for the original problem (3.1.4). $\hat{\varphi} \in H^1(\Omega)$ is given. $\langle \sigma \nabla \hat{\varphi}, n \rangle = 0$, because of the definition of the problem.

The only remaining problem is to show that $\hat{\varphi} \in H^3(B)$. We will show this, with the help of established theorems.

$\left(\int_\Omega \psi_k dx - (\int_\Omega \psi_k dx) \eta \right) \in H^1(\Omega)$ and under the assumption that $\sigma \in C^2(B_i)$ for all i we can conclude with [28, 6.3.1, Thm 2] that $\hat{\varphi} \in H^3(B_i)$.

Since for all i B_i fulfills the weak cone property, $H^3(B_i)$ is embedded into $C^0(B_i)$ and thus $\hat{\varphi} \in C^0(B_i)$ [2, 1].
Hence, $\hat{\varphi}$ fulfills all properties for X.
The next step is to get an estimate for $\|\hat{\varphi}\|_{C^0(B)}$.
$B = \bigcap_{i=1}^{n} B_i$ and $\bigcap_{i=1}^{n} B_i = \emptyset$, therefore $\|\hat{\varphi}\|_{C^0(B)} = \sum_{i=1}^{n} \|\hat{\varphi}\|_{C^0(B_i)}$.
For each B_i we can apply the embedding estimate and get that

$$\|\hat{\varphi}\|_{C^0(B_i)} \leq C \|\hat{\varphi}\|_{H^3(B_i)}$$

We further can use the estimation of [28, 6.3.1, Thm 2] and assess

$$\|\hat{\varphi}\|_{H^3(B_i)} \leq \tilde{C} \left(\left\| \psi_k - \eta \int_\Omega \psi_k dx \right\|_{H^1(B_i)} + \|\hat{\varphi}\|_{L^2(B_i)} \right).$$

For the last part we estimate

$$\|\hat{\varphi}\|_{L^2(B_i)}^2 \leq C \|\nabla \hat{\varphi}\|_{L^2(B_i)}^2$$

due to the Poincaré inequality.
Further we evaluate

$$\begin{aligned}
\|\nabla \hat{\varphi}\|_{L^2(B_i)}^2 &= \frac{1}{\beta} \left(\int_\Omega \sigma \nabla \hat{\varphi} \nabla \hat{\varphi} dx \right) \\
&= \frac{1}{\beta} \left(\int_\Omega \left(\psi_k - (\int_\Omega \psi_k dx) \eta dx \right) \hat{\varphi} \right) \\
&\leq \left\| \psi_k - \eta \int_\Omega \psi_k dx \right\|_{L^2(\Omega)} \cdot \|\hat{\varphi}\|_{L^2(\Omega)} \\
&\leq \left\| \psi_k - \eta \int_\Omega \psi_k dx \right\|_{H^1(\Omega)} \cdot \|\hat{\varphi}\|_{L^2(\Omega)} \\
\Rightarrow \quad \|\hat{\varphi}\|_{L^2(\Omega)} &\leq \left\| \psi_k - \int_\Omega \psi_k dx \right\|_{H^1(\Omega)}.
\end{aligned}$$

So we really only have to get an estimate for $\|\psi_k - (\int_\Omega \psi_k dx)\eta\|_{H^1(B_i)} \leq \|\psi\|_{H^1(B_i)} + \|(\int_\Omega \psi)\eta\|_{H^1(B_i)}$. This is done with

$$\begin{aligned}
\|\psi_k - (\int_\Omega \psi_k dx)\eta\|_{H^1(B_i)} &\leq \|\psi\|_{H^1(B_i)} + \|(\int_\Omega \psi_k dx)\eta\|_{H^1(B_i)} \\
&\leq \|\psi\|_{H^1(B_i)} + \left| (\int_\Omega \psi_k dx) \right| \|\eta\|_{H^1(B_i)} \\
&\leq \|\psi\|_{H^1(B_i)} + C\|\psi\|_{L^2(B_i)} \\
&\leq \|\psi\|_{H^1(B_i)} + \tilde{C}\|\psi\|_{H^1(B_i)},
\end{aligned}$$

for constants $C, \tilde{C}$, which do not depend on φ or ψ.
Therefore we can conclude that

$$\|\hat{\varphi}\|_{C^0(B_i)} \leq C_i \|\psi\|_{H^1(\Omega)}. \tag{3.1.6}$$

Because it is true for every $i = 1, \dots, n$, it also holds for the sum and we yield

$$\|\hat{\varphi}\|_{C^0(B)} \leq C \|\psi\|_{H^1(\Omega)} \tag{3.1.7}$$

for a constant C.
Then we can compute the duality product $|\langle u_k, \psi_k \rangle|$. Since [28, Thm.5.9.1 (iii)] it is the same as the L^2 product, i.e.

$$\begin{aligned}
|\langle u_k, \psi_k \rangle| &= \left| \int_\Omega u_k \quad \psi_k dx \right| \\
&= \left| \int_\Omega u_k \quad \psi_k dx - \left(\int_\Omega \psi_k dx \right) \underbrace{\int_\Omega u_k \ \eta}_{=0} \right| \\
&= \left| \int_\Omega u_k \ \left(\psi_k - \eta \int_\Omega \psi_k dx \right) dx \right|
\end{aligned}$$

Because u_k is a test function for the 2nd equation we can transform the last line to

$$\left| \int_\Omega u_k \ \left(\psi_k - \eta \int_\Omega \psi_k dx \right) dx \right| = \left| \int_\Omega \ u_k \nabla \cdot (\sigma \nabla \hat{\varphi}) dx \right|$$

Further $\hat{\varphi}$ is a test function for the 2nd equation such that

$$\left| \int_\Omega \ u_k \nabla \cdot (\sigma \nabla \hat{\varphi}) dx \right| = \int_\Omega \sum_{i=1}^n q_i \delta_{i_k} \hat{\varphi} dx.$$

We choose k such that supp $\delta_{i_k} \subset B$ for all i and have

$$\begin{aligned}
\int_\Omega \sum_{i=1}^n q_i \delta_{i_k} \hat{\varphi} dx &\leq \sum_{i=1}^n |q_i| \|\hat{\varphi}\|_{C^0(B_i)} \underbrace{\int_\Omega \delta_{i_k} dx}_{=1} \\
&\leq C \|\hat{\varphi}\|_{C^0(B)} \sum_{i=1}^n |q_i|
\end{aligned}$$

Finally we apply the estimate (3.1.7) from above and get that

$$C \|\hat{\varphi}\|_{C^0(B)} \sum_{i=1}^n |q_i| \leq c_0 \left(\sum_{i=1}^n |q_i| \right) \|\psi\|_{H^1(\Omega)}.$$

This means that u_k is bounded in the H^{-1}–norm with

$$\|u_k\|_{H^{-1}(\Omega)} = \sup_{\psi \in H_0^1(\Omega)} \frac{|\langle u_k, \psi_k \rangle|}{\|\psi\|_{H^1(\Omega)}} \leq c_0 \left(\sum_{i=1}^{n} |q_i| \right).$$

This holds for all $k \in \mathbb{N}$, which gives a bounded sequence in $H^{-1}(\Omega)$.
$H^{-1}(\Omega)$ has a weak*-topology ([3], C_0^∞ is separable and dense in H^1 is C^∞ completed with the H^1-norm) and therefore, we can assume the existence of a weak*-convergent subsequence in $H^{-1}(\Omega)$, which we also call u_k.
Let $u \in H^{-1}$ be the limit of u_k.
Then

$$\begin{aligned}
&\int_\Omega u_k \nabla \cdot (\sigma \nabla \hat{\varphi}) dx = \langle u_k, \nabla \cdot (\sigma \nabla \hat{\varphi}) \rangle \rightharpoonup^* \langle u, \nabla \cdot (\sigma \nabla \hat{\varphi}) \rangle \\
&\int_\Omega \sum_{i=1}^{n} q_i \delta_{i_k} \varphi dx \qquad\qquad\qquad\qquad \rightharpoonup^* \sum_{i=1}^{n} q_i \varphi(x_i) \quad \text{because } \hat{\varphi} \in C^0(B)
\end{aligned}$$

for any $\hat{\varphi} \in X$.
Additionally,

$$0 = \int_\Omega u_k \; \eta dx = \langle u_k, \eta \rangle \rightharpoonup^* \langle u, \eta \rangle.$$

Since u satisfies every condition of (3.1.4), it has to be a solution.
The last step is now to repeat this proof and assume that $\psi \in L^p(\Omega)$ for a certain p.
Since we have the weak cone property of B, we know that $W^{2,p}(B)$ is embedded in $C^0(B)$ for $p \geq 2$. Therefore $\varphi \in W^{2,p}(B)$ means that the estimate (3.1.7) changes to

$$\|\hat{\varphi}\|_{C^0(B_i)} \leq c_0 \|\psi\|_{L(B_i)}.$$

This then leads to the estimate

$$\begin{aligned}
|\langle u_k, \psi_k \rangle| &= \left| \int_\Omega u_k \;\; \psi_k dx \right| \\
&\leq \sum_{i=1}^{n} |q_i| \|\hat{\varphi}\|_{C^0(B_i)} \underbrace{\int_\Omega \delta_{i_k} dx}_{=1} \\
&\leq c_0 \left(\sum_{i=1}^{n} |q_i| \right) \|\psi\|_{L^p(\Omega)}
\end{aligned}$$

and thus

$$\|u_k\|_{L^q(\Omega)} = \sup_{\psi \in L_p(\Omega)} \frac{|\langle u_k, \psi_k \rangle|}{\|\psi\|_{L_p(\Omega)}} \leq c_0 \left(\sum_{i=1}^{n} |q_i| \right)$$

for q with $\frac{1}{p} + \frac{1}{q} = 1$. Now the argument with the limits is repeated like above. $\square$

Theorem 3. *Let assumption 3 hold. Then the solution $u \in L^q$ of theorem 2 is unique.*

Proof. Any solution $u \in L^q$ of theorem 2 fulfills the duality product

$$\begin{aligned} |\langle u, \psi \rangle| &= \left| \int_\Omega u \quad \psi dx \right| \\ &\leq \sum_{i=1}^{n} |q_i| \|\hat{\varphi}\|_{C^0(\Omega)} \underbrace{\int_\Omega \delta_{i_k} dx}_{=1} \\ &\leq c_0 \left(\sum_{i=1}^{n} |q_i| \right) \|\psi\|_{L_p(\Omega)} \end{aligned}$$

for a $\psi \in H_0^1(\Omega)$.
Therefore, we obtain the a-priori estimate

$$\|u\|_{L_q(\Omega)} = \sup_{\psi \in L_p(\Omega)} \frac{|\langle u, \psi \rangle|}{\|\psi\|_{L_p(\Omega)}} \leq c_0 \left(\sum_{i=1}^{n} |q_i| \right).$$

Now let u_1 and u_2 be two solutions. Set $\Phi(x) = u_1(x) - u_2(x)$.
Then Φ also fulfills the pure Neumann conditions and

$$\int_\Omega \Phi \nabla \cdot (\sigma \nabla \varphi) dx = 0 \quad \text{for all } \varphi \in X.$$

We then obtain

$$\|\Phi\|_{H^{-1}(\Omega)} \leq c_0 \sum_{i=1}^{n} |q_i - q_i| = 0$$

and therefore $\Phi = 0$ in $L^q(\Omega)$.

$\square$

This proof only shows that there exists a weak solution of the problem 3.0.2, which is unique. It does not say anything about how good the new approximation is in regard to the old problem (2.0.2). It neither gives an error bound nor does it say anything about a solution of the old problem. For an error bound one has to know how to choose the monopoles and how the strengths of the monopoles should be computed. So that is our next step.

Remark 3. *Theorem 2 and theorem 3 are independent of the choice of the monopoles. They are valid for the* Venant Approach *as well as the new approach.*

3.2 Choice of the monopole locations

So far, we just assumed some random number of monopoles and monopole locations. What we want to do is to place monopoles onto FE nodes. It makes sense to use the FE next to the dipole location x_0.
In the context of the *Venant Approach*, the nodes are chosen as follows:
x_1 is the node nearest to the dipole location x_0. $x_2, \dots, x_n$ are those nodes connected to x_1 with either an edge or a face or a volume.
Here, n is not fixed and completely dependent on the FE grid.
Secondly, one could define a $n \in \mathbb{N}$ and compute those FE nodes which are the n closest to the dipole location.
Thirdly, one could mix both heuristics.
We will see different strategies for the *Multipole Approach* later in the chapter 4.
Using this, the right–hand side - the monopole distribution - can then be discretized as

$$\mathbf{J}_h = \sum_{i=1}^{n} (J_h)_i \cdot \varphi_i(x),$$

with

$$(J_h)_j = \begin{cases} q_j, & \text{if } x_j \in \{x_1, \dots, x_n\} \\ 0, & \text{else.} \end{cases}$$

The missing information is the $q_i, \dots, q_n \in \mathbb{R}$.
The *Venant Approach* [18] described in chapter 2.2.3 provides one way to compute those.
We use a new way to compute this monopole distribution. We start at the potential of the dipole and the monopole distribution and use common multipole expansion to compare those. By doing this, we are able to describe an algorithm for the computation of the monopole loads $q_i, \dots, q_n$ corresponding to the locations $x_1, \dots, x_n$.

3.3 Multipole expansion to compute the strengths of the monopoles

The original problem was to compute u_{dip} for the mathematical dipole and solve the equation

$$
\begin{aligned}
\nabla \cdot (\sigma \nabla u_{dip}) &= \nabla \cdot (\overrightarrow{M}\ \delta_{x_0}(x)) \ \text{ in } \Omega \\
\sigma \nabla u_{dip} \cdot n &= 0 \qquad\qquad\qquad \text{on } \partial\Omega.
\end{aligned}
$$

for $u_{dip} \in L_2(\Omega)$, compare (2.0.2).
Instead we now want to compute u_{mon} for the monopole problem and solve

$$
\begin{aligned}
\nabla \cdot (\sigma \nabla u_{mon}) &= \sum_{i=1}^{n} q_i \ \ \delta_{x_i}(x) \ \text{ in } \Omega \\
\sigma \nabla u_{mon} \cdot n &= \qquad\qquad 0 \quad \text{on } \partial\Omega.
\end{aligned}
$$

for u_{mon}.
The u symbolizes the electric potential. In the first equation u_{dip} is the electric potential of the dipole and in the second equation u_{mon} is the electric potential of a monopole distribution.
Those potentials should be the same. To ensure this, we use Multipole expansion to expand the dipole potential and the monopole distribution potential.
For this, we require the assumption

Assumption 4. *Let* $\mathbb{R}^+$. *Let* $x_1, \dots, x_n, x_+, x_- \in \Omega_h$ *fulfill that a small ball around the origin with radius* $\delta \in \mathbb{R}^{>0}$ *exists such that* $x_1, \dots, x_n \in B_\delta(0) := \{x \in \Omega_h \mid |x| < \delta\}$ *and a* $\sigma_0 \in \mathbb{R}^+$ *such that*

$$
\sigma(x) = \sigma_0 \ \text{ for all } x \in B_\delta(0). \tag{3.3.1}
$$

We define δ_0 *as the maximal* $\delta \in \mathbb{R}$ *such that* (3.3.1) *holds.*

We will also need the definition

Definition 4. *For the expansion of the monopole distribution we define*

$$
\delta_1 := \inf \{\delta \in \mathbb{R} \mid \delta_0 \geq \delta_1 > \max\{|x_1|, \dots, |x_n|\}\} . \tag{3.3.2}
$$

For error estimation it is important that $\delta_1 > \max\{|x_1|, \dots, |x_n|\}$.
We define $\sigma(x) := \sigma_0 \in \mathbb{R}^{>0}$ as in assumption 4. Let the dipole location be the origin of the coordinate system.
The potentials are not in the function space $L_2(\Omega)$ – neither at the location of the dipole, nor at the locations of the monopoles, so we are not able to use this norm. But we are not interested in the fact that the error in the potentials is minimal at those locations. We are only interested in the fact that the error at the EEG's sensor positions is minimal.
As explained before, we cannot make error estimations for the case of homogeneous conductivity but we are able to estimate the error on the surface of the small same-conductivity ball around the dipole location.

So we choose the norm

$$\|v\|_* := \|v\|_{L_2(B_{\delta_0}(0)\setminus B_{\delta_1}(0))}. \tag{3.3.3}$$

The potential of the dipole, which is also the solution of 2, can be represented by the fundamental solution

$$\Phi_{\mathrm{D}}(x) = \frac{1}{4\pi\sigma_0} \cdot \frac{\langle \overrightarrow{M}, x\rangle}{|x|^3}. \tag{3.3.4}$$

This potential is a pure dipole potential and cannot be expanded further. Every moment except the dipole moment is zero.
The potential of the monopole distribution is

$$\Phi_{\mathrm{M}}(x) = \frac{1}{4 \cdot \sigma_0 \pi} \cdot \sum_{i=1}^{n} \frac{q_i}{\|x - x_i\|_2}. \tag{3.3.5}$$

For this potential we use multipole expansion to make it easy to compare with the dipole potential.
Multipole expansion transforms the potential of the monopole distribution into an infinite sum, where every summand is the respective higher order moment [31].
We then can conclude with the definitions of the scalar product and the l_2-Norm, that

$$\begin{aligned}\frac{1}{\|x - x_i\|_2} &= (|x|^2 + |x_i|^2 - 2\langle x_i, x\rangle)^{-1/2}\\ &= |x| \left(1 + \frac{|x_i|^2}{|x|^2} - \frac{\langle 2 \cdot x_i, x\rangle}{|x|^2}\right)^{-1/2}\end{aligned}$$

for all $i \in \{1, \dots, n\}$.
With the last factor we have used the Taylor expansion with the simplified function $(1+y)^{-1/2}$, where we substituted $\frac{|x_i|^2}{|x|^2} - \frac{\langle 2\cdot x_i, x\rangle}{|x|^2}$ with y.
This Taylor expansion can be used only for $y < 1$, which means that $|x| \gg |x_i|$ must hold.
Inserting and re-substituting gives the expression

$$\Phi_{\mathrm{M}}(x) = \frac{1}{4\pi\sigma_0} \sum_{l=1}^{\infty} \sum_{i=1}^{n} \frac{q_i \cdot |x_i|^l}{|x|^{l+1}} \mathcal{P}_l(\cos(\theta_i)), \tag{3.3.6}$$

where $\mathcal{P}_l(x)$ are the *Legendre Polynomials* of order $l \in \mathbb{N}$ and θ_i is the angle between the position vectors of the evaluation point x and the monopole location x_i.

Ideally, we would then want to compute the strength of the monopole distribution in such a way that the potentials are the same.
This would mean to solve the problem

Problem 6. *Given are the monopole locations $x_1, \dots, x_n$ and the dipole potential Φ_D. Compute $q_1, \dots, q_n$ such that*

$$\|\Phi_D - \Phi_M\|_* = \min_{(\tilde{q}_1,\dots,\tilde{q}_n)} \left\| \frac{1}{4\pi\sigma_0} \cdot \frac{\langle \overrightarrow{M}, x\rangle}{|x|^3} - \frac{1}{4\pi\sigma_0} \sum_{l=1}^{\infty} \sum_{i=1}^{n} \frac{\tilde{q}_i \cdot |x_i|^l}{|x|^{l+1}} \mathcal{P}_l(cos(\theta_i)) \right\|_* .$$

We can minimize the norm with the help of comparing the coefficients of both expansions.
Unfortunately, this would require solving an infinite sum of equations.

3.3.1 A computational algorithm

To compute the loads q_i with a computable algorithm, we have to reduce the problem to a finite number of sums.
The dipole potential contains only the second order term – every other term is equal to zero. Terms within the monopole expansion decay with at least $\frac{1}{\delta_0^l}$. Hence, the decision to cut the potential of the monopoles after the third term seems reasonable.
What remains is to compute $q_1, \dots, q_n$ fulfilling

$$\left\| \Phi_D(x) - \frac{1}{4\pi\sigma_0} \sum_{l=0}^{2} \sum_{i=1}^{n} \frac{q_i \cdot |x_i|^l}{|x|^{l+1}} \mathcal{P}_l(cos(\theta_i)) \right\|_* \rightarrow min.$$

Let $\tilde{\Phi}_M(x) := \frac{1}{4\pi\sigma_0} \sum_{l=0}^{2} \sum_{i=1}^{n} \frac{q_i \cdot |x_i|^l}{|x|^{l+1}} \mathcal{P}_l(\cos(\theta_i))$. With the definition of the scalar product we acquire

$$\begin{aligned}
\tilde{\Phi}_{\mathrm{M}}(x) = & \frac{1}{4\pi\sigma_0 |x|} \sum_{i=1}^{n} q_i \\
& + \frac{1}{4\pi\sigma_0 |x|^2} \left\langle \sum_{i=1}^{n} q_i \cdot x_i, \frac{x}{|x|} \right\rangle \\
& + \frac{1}{4\pi\sigma_0 2|x|^3} \left\langle \frac{x}{|x|}, \frac{\sum_{i=1}^{n} q_i \left(3x_i \otimes x_i - |x_i|^2 \, I_{3\times 3}\right)}{2} \frac{x}{|x|} \right\rangle .
\end{aligned}$$

If one then compares both potentials, one has to fulfill the following conditions:

$$\begin{aligned}
0 &= \frac{1}{4\pi\sigma_0|x|} \sum_{i=1}^{n} q_i \\
\frac{1}{4\pi\sigma_0}\frac{\langle\overrightarrow{M},x\rangle}{|x|^3} &= \frac{1}{4\pi\sigma_0|x|^2}\left\langle \sum_{i=1}^{n} q_i x_i, \frac{x}{|x|} \right\rangle \\
0 &= \frac{1}{4\pi\sigma_0 2|x|^3}\left\langle \frac{x}{|x|}, \frac{\sum_{i=1}^{n} q_i \left(3x_i \otimes x_i - |x_i|^2 I_{3\times 3}\right)}{2} \cdot \frac{x}{|x|} \right\rangle .
\end{aligned} \tag{3.3.7}$$

These conditions should hold for all $x \in \Omega$, so they are transformed into equations independent of x, namely

$$\begin{aligned}
0 &= \sum_{i=1}^{m} q_i \\
\overrightarrow{M} &= \sum_{i=1}^{m} q_i x_i \\
0_{3x3} &= \sum_{i=1}^{m} \frac{q_i}{2}\left(3x_i \otimes x_i - |x_i|^2 I_{3\times 3}\right)
\end{aligned} \tag{3.3.8}$$

We can interpret these conditions as linear equations of $q_1, \dots, q_n$ and thus we get a matrix V and vectors $\overrightarrow{q}$ and $\overrightarrow{t}$ such that

$$\underbrace{\begin{pmatrix} 0 \\ \overrightarrow{M}_1 \\ \overrightarrow{M}_2 \\ \overrightarrow{M}_3 \\ 0 \\ \\ \vdots \\ \\ 0 \end{pmatrix}}_{=:\overrightarrow{t}} = \underbrace{\begin{pmatrix}
1 & 1 & \dots & 1 \\
x_{11} & x_{21} & \dots & x_{n1} \\
x_{12} & x_{22} & \dots & x_{n2} \\
x_{13} & x_{23} & \dots & x_{n3} \\
3 \cdot {x_1}_1^2 - |x_1|^2 & 3 \cdot {x_2}_1^2 - |x_2|^2 & \dots & 3 \cdot {x_n}_1^2 - |x_n|^2 \\
3 \cdot {x_1}_2^2 - |x_1|^2 & 3 \cdot {x_2}_2^2 - |x_2|^2 & \dots & 3 \cdot {x_n}_2^2 - |x_n|^2 \\
3 \cdot {x_1}_3^2 - |x_1|^2 & 3 \cdot {x_2}_3^2 - |x_2|^2 & \dots & 3 \cdot {x_n}_3^2 - |x_n|^2 \\
3 \cdot x_{11} \cdot x_{12} & 3 \cdot x_{21} \cdot x_{22} & \dots & 3 \cdot x_{n1} \cdot x_{n2} \\
3 \cdot x_{11} \cdot x_{13} & 3 \cdot x_{21} \cdot x_{23} & \dots & 3 \cdot x_{n1} \cdot x_{n3} \\
3 \cdot x_{13} \cdot x_{12} & 3 \cdot x_{23} \cdot x_{22} & \dots & 3 \cdot x_{n3} \cdot x_{n2}
\end{pmatrix}}_{=:V} \cdot \underbrace{\begin{pmatrix} q_1 \\ q_2 \\ \\ \vdots \\ \\ \vdots \\ \\ q_n \end{pmatrix}}_{=:\overrightarrow{q}} . \tag{3.3.9}$$

Computing the $\overrightarrow{q}$ now means to minimize the functional

$$F(\overrightarrow{q}) = \|V \cdot \overrightarrow{q} - \overrightarrow{t}\|_2^2 \to \text{min.} \tag{3.3.10}$$

Solving this alone might lead to problems. If there happen to be fewer monopole locations than multipole conditions, the system would be underdetermined and would provide rather unstable results.
We would like to have stable results in the sense of regularization theory. That means that high spatial frequency components in the q-vector should be penalized to obtain low energy solutions.
To ensure such results a $1 > \lambda > 0$ and $W \in \mathbb{R}^{3n \times n}$ is chosen with

$$W = \begin{pmatrix} \operatorname{diag}(|x_{1,1}|, \cdots, |x_{n,1}|) \\ \operatorname{diag}(|x_{1,2}|, \cdots, |x_{n,2}|) \\ \operatorname{diag}(|x_{1,3}|, \cdots, |x_{n,3}|) \end{pmatrix}. \tag{3.3.11}$$

This is added within a penalty term $\lambda^2 ||W \cdot \overrightarrow{q}||_2^2$ which should be minimized additionally.
It ensures stability and a certain degree of smoothness for the monopoles. Monopole locations farther away will get assigned smaller strength values.
With the added penalty term, we compute the strength of the monopoles while minimizing the functional

$$F_\lambda(\overrightarrow{q}) = ||\overrightarrow{t} - V \cdot \overrightarrow{q}||_2^2 + \lambda ||W \cdot \overrightarrow{q}||_2^2 \tag{3.3.12}$$

for $\overrightarrow{q}$.
λ can be chosen arbitrarily. It indicates how much the $q_1, \ldots, q_n$ will be smoothed and is needed for good results. The bigger λ gets, the less important the multipole conditions will become. In experiments later on it is shown that a λ in the range of 10^{-4} to 10^{-10} is a good choice, although there are cases where a bigger λ should be chosen.
The functional itself can be solved with a lot of different methods like the QR-algorithm or the minimum norm estimate.

Remark 4. *The* Venant Approach *and the* Multipole Approach *share the first four conditions*

$$\begin{aligned} 0 &= \sum_{i=1}^{m} q_i \text{ and} \\ \overrightarrow{M} &= \sum_{i=1}^{m} q_i x_i. \end{aligned} \tag{3.3.13}$$

Remark 5. *If* $x_0 \neq \begin{pmatrix} 0 \\ 0 \\ 0 \end{pmatrix}$, *then for computational purposes we can use* $x_1 - x_0, \ldots, x_n - x_0$ *in the computations.*

3.4 Error estimation for the *Multipole Approach*

It remains to answer the last question from earlier:
[**Accuracy**]: How good is the substitution of using a monopole distribution instead of a mathematical dipole?
For answering this question, we can give an error bound.

Theorem 4. *Let assumptions 3 and 4 hold, $x_1, \dots, x_n$ be the monopole locations, and $q_1, \dots, q_n$ fulfill the conditions*

$$\begin{aligned} \overrightarrow{M} &= \sum_{i=1}^{m} q_i x_i \\ 0_{3x3} &= \sum_{i=1}^{m} \frac{q_i}{2} \left(3x_i \otimes x_i - |x_i|^2 I_{3\times 3} \right). \end{aligned}$$

Then the error between the potential of the monopole distribution $\Phi_M(x)$ and the potential of the dipole $\Phi_D(x)$ is

$$\|\Phi_D(x) - \Phi_M(x)\|_* \leq C \frac{1}{\delta_0} \left(\frac{1}{1 - \frac{|x_{max}|}{\delta_0}} \right)$$

with $C \in \mathbb{R}$ and $C = C(\sigma_0, n, q_{\max}, \Omega)$.

Proof. The error we want to evaluate is

$$\|\Phi_D(x) - \Phi_M(x)\|_*,$$

but we actually didn't compute Φ_M, but rather $\tilde{\Phi}_M$. So we add and subtract $\tilde{\Phi}_M$ and estimate with the help of the triangle inequality:

$$\begin{aligned} \|\Phi_D(x) - \Phi_M(x)\|_* &= \|\Phi_D(x) - \tilde{\Phi}_M + \tilde{\Phi}_M - \Phi_M(x)\|_* \\ &\leq \|\Phi_D(x) - \tilde{\Phi}_M\|_* + \|\Phi_M(x) - \tilde{\Phi}_M\|_*. \end{aligned}$$

Thus, the error can be estimated by the sum of two others: the approximation error and the model error.
We can not control the model error $\|\Phi_M(x) - \tilde{\Phi}_M(x)\|_*$. It only depends on the choice of the model for the brain activity.
The approximation error can be written as

$$\|\Phi_D(x) - \tilde{\Phi}_M\|_* = \left\| \frac{1}{4\pi\sigma_0} \frac{\langle \overrightarrow{M}, x \rangle}{|x|^3} - \frac{1}{4\pi\sigma_0} \sum_{l=1}^{3} \sum_{i=1}^{n} \frac{q_i |x_i|^l}{|x|^{l+1}} \mathcal{P}_l(\cos(\theta_i)) \right\|_*$$

And since the error at a point is only determined by the difference of the moments we evaluate

$$\begin{aligned}\|\Phi_D(x) - \tilde{\Phi}_M(x)\|_* &= \left\| \frac{1}{4\pi\sigma_0} \frac{\langle \overrightarrow{M}, x\rangle}{|x|^3} - \frac{1}{4\pi\sigma_0} \sum_{l=1}^{3} \sum_{i=1}^{n} \frac{q_i |x_i|^l}{|x|^{l+1}} \mathcal{P}_l(\cos(\theta_i)) \right\|_* \\ &\leq C(\Omega) \min_{\overrightarrow{q} \in \mathbb{R}^n} \|\overrightarrow{t} - V \cdot \overrightarrow{q}\|_2^2 + \lambda^2 \|W \cdot \overrightarrow{q}\|_2^2.\end{aligned}$$

This is an error we can minimize by the choice of the algorithm to compute the $\overrightarrow{q} = (q_1, \dots, q_n)$. Thus, we can theoretically ensure that it is smaller then the model error $\|\Phi_M(x) - \tilde{\Phi}_M(x)\|_*$.

Because we obtain $\tilde{\Phi}(x)$ through truncation of $\Phi(x)$ after the first three summands, we get that

$$\|\Phi_M(x) - \tilde{\Phi}_M(x)\|_* = \left\| \underbrace{\frac{1}{4\pi\sigma_0}}_{=:C(\sigma_0)} \sum_{l=3}^{\infty} \sum_{i=1}^{n} \frac{q_i |x_i|^l}{|x|^{l+1}} P_l(\cos\theta_i) \right\|_*$$

We then make use of the fact that the inner sum is finite and that *Legendre Polynomials* are bounded on the interval $[-1, 1]$ by the value 1 to get

$$C(\sigma_0) \left\| \sum_{l=3}^{\infty} \sum_{i=1}^{n} \frac{q_i |x_i|^l}{|x|^{l+1}} P_l(\cos\theta_i) \right\|_* \leq C(\sigma_0) \left\| \sum_{l=3}^{\infty} n \cdot \frac{q_{\max} |x_{\max}|^l}{|x|^{l+1}} \right\|_* .$$

Further we can combine all constants and yield

$$C(\sigma_0) \cdot \left\| \sum_{l=3}^{\infty} n \cdot \frac{q_{\max} |x_{\max}|^l}{|x|^{l+1}} \right\|_* \leq C(\sigma_0, n, q_{\max}) \left\| \sum_{l=3}^{\infty} \frac{|x_{\max}|^l}{|x|^{l+1}} \right\|_* .$$

Now we exploit that $x \in B_{\delta_0}(x_0)$ such that

$$
\begin{aligned}
C(\sigma_0, n, q_{\max}) \left\| \sum_{l=1}^{\infty} \frac{|x_{\max}|^l}{|x|^{l+1}} \right\|_* &\leq C(\Omega, n, q_{\max}) \left\| \sum_{l=3}^{\infty} \frac{|x_{\max}|^l}{\delta_0^{l+1}} \right\|_* \\
&\leq C(\sigma_0, n, q_{\max}, \Omega) \frac{1}{\delta_0} \sum_{l=3}^{\infty} \frac{|x_{\max}|^l}{\delta_0^l} \\
&\leq C(\sigma_0, n, q_{\max}, \Omega) \frac{1}{\delta_0} \sum_{l=1}^{\infty} \frac{|x_{\max}|^l}{\delta_0^l} \\
&\leq C(\sigma_0, n, q_{\max}, \Omega) \frac{1}{\delta_0} \left(\frac{1}{1 - \frac{|x_{\max}|}{\delta_0}} \right).
\end{aligned}
$$

□

In an EEG forward problem setting we will have conductivity jumps which might have an error propagation not covered by this estimate. Therefore, the computation of this kind of error for numerical experiments does not make sense.

Nevertheless, the estimate helps us to understand the *Multipole Approach* more deeply.

It shows that the size of error decreases when the difference between $|x_{\max}|$ and δ_0 increases. By definition: $\frac{|x_{\max}|}{\delta_0} < 1$ – if the area of uniform conductivity is bigger, this fraction is much smaller.

If we compute on uniform conductivity, this implication is especially relevant. The estimator is maximal at the border of $B_{|x_{\max}|}(x_0)$ (if $|x_{\max}| \approx \delta_0$) and decreases towards the border of the domain we compute on, where the sensors are located (if $\frac{|x_{\max}|}{<} < \delta_0$).

This is convenient for us, since we are interested in a minimal error at the sensor locations.

For cases which do not include uniform conductivity but several layers, we can achieve a big difference between $|x_{\max}|$ and δ_0 by ensuring the grid we compute on fulfills the following:

- Firstly, the area of the monopole distribution should be as small as possible.
- Secondly, the area of uniform conductivity should be as big as possible.

From a FEM perspective, we cannot control the area of uniform conductivity. This is determined by the different electrically conducting layers of the head and the location of the brain activity within those layers.

However, we can control the area of the monopole distribution by choosing the grid resolution. Since we place the monopoles onto FE nodes, a fine grid resolution around the dipole will ensure that all monopoles are placed in a very small area. A coarse grid resolution widens the area where monopoles are placed and such decreases the distance to the next conductivity jump. In this case a more refined grid in that area seems to be a better choice.

4 Numerical experiments

The *Multipole Approach* is eventually intended to be used in live applications for EEG source reconstruction. To show its suitability for this purpose, we need to compare numerical results of the *Multipole Approach* with the results of other contemporary approaches.
In this chapter, we will continuously make the following assumptions:

Assumption 5. *Let Ω_h be a triangulation of the domain Ω, where the EEG forward problem should be solved. Let $m \in \mathbb{N}$ be the number of FE nodes and let that also be the number of degrees of freedom. Let $n_{Multipole} \in \mathbb{N}$ be the number of computed Monopoles for the* Multipole Approach *and let n_{Venant} be the number of computed monopoles for the* Venant Approach*.*

This assumption is relatively strict, since that means that we are restricted to using linear FE basis functions. However, the application of CG-Methods using a linear basis is common, so this does not pose a problem.

Remark 6. *The* Multipole Approach *and the* Venant Approach *are very similar. They stem from the same idea to substitute the dipole with a distribution of monopoles. They differ in the computation of the monopoles. Superficially, the* Multipole Approach *appears to be more computationally expensive since it requires solving a system of $10 * n_{Multipole}$ equations plus penalty term, while the* Venant Approach *only requires solving $7 * n_{Venant}$ equations plus penalty term. However, for one FE step we require the solution of a secondary system containing m^2 equations, which usually dwarfs the primary equation system by orders of magnitude ($n_{Multipole}, n_{Venant} << m$) and $n_{Multipole}, n_{Venant} \in [1, 20]$. Therefore, the differences in computational load between these two approaches can be neglected in practice.*
We will later see that $n_{Multipole}$ differs from n_{Venant}.

We concentrate on comparing the accuracy of the *Multipole Approach* with the other contemporary approaches.
Therefore, we will examine the *Multipole Approach* in four different settings, all designed to test different aspects.

1. First, we test how well every approach resolves the mathematical dipole. These computations can be done in 2D. For this purpose, we establish a

regularly spaced 2D grid of vertices and assign a uniform conductivity. In this setting, we know the analytical solution (meaning we can compute the best approximation with regard to the energy norm just by interpolating the analytic solution as well). For convenience, we prescribe Dirichlet boundary conditions. We place a dipole, compute the forward solutions, and compare the accuracy to the analytic solution. This procedure should give us a good impression of how well a dipole can be approximated with the different approaches.

2. Second, we compare the forward solutions of the *Multipole Approach*, the *Venant Approach*, and the *Partial Integration Approach* on 3D sphere models. We know from De Munck and Peters [58] that the pointwise solution for this type of model can be precisely calculated with a series expansion. Therefore, sphere models offer the possibility to test the approaches with layers of varying electric conductivity. Additionally, we need to prescribe the original *Neumann boundary conditions*. This kind of numerical computation illustrates just how precise the approach is in forward computations.

3. Third, we compute a so–called *goal function scan* on the forward solutions of the *Venant Approach* and the *Multipole Approach* on a path of the previously used 3D sphere models. This procedure can be understood as a brute force inverse solution search routine. Thus, the numerical results can demonstrate how well the approach will do in non-manual inverse computations, without actually having to use a suitable inverse solver.

4. Fourth, we have an overview about possible pitfalls with the *Multipole Approach*. We shed light on how parameter choices influence the forward solution, and propose a heuristic setting for yielding agreeable results.

5. Fifth and last, we revisit the numerical experiments in 3D and the goal function scan in the context of different error measures.

The *Multipole Approach*, *Venant Approach* and *Partial Integration Approach* are implemented into the C++ library *UG4* [80, 68] within the plugin *konnekfem*. The FE grids were generated using the software library *ProMesh* [67]. Additionally, we use the matlab library *fieldtrip* [64] to compute the De Munck and Peters Sphere solution [58]. More details about our usage of the UG4 plugin *konnekfem*, as well as the multipole routines for fieldtrip, can be found in the appendix.
For the *Multipole Approach* and the *Venant Approach* we use monopole locations fulfilling the so called *Venant Condition* exclusively [51]. This is the case if all monopole locations are located within one sphere layer.

In the 2D computations, we measure the accuracy with an L_2 error on a certain area within the grid. This area is contained in various triangles located at the border of the domain.

For the 3D computations, we calculate the discrete values of the FE solution at m different sensor positions u_{sens}. We measure the accuracy by calculating the l_2 error to the reference values of a De Munck and Peters sphere solution u_{DM}. This error is defined by

$$l_2(u_{\text{sens}}, u_{\text{DM}}) := \|u_{\text{sens}} - u_{\text{DM}}\|_2.$$

In other research, two different error measures are commonly used: the (discrete) RDM (short for *Relative Difference Measure*) and the (discrete) MAG (short for *Magnitude Error*) [52]. Those errors are equivalent to the discrete l_2 error. Due to the equivalence, we limit our primary experiments to measuring the absolute discrete l_2 error. Computations for alternative error measures can be found in last section of this chapter.

The graphics for the analysis of the results are plotted with the python library *matplotlib* [35].

We can distinguish between several types of plots. To image the differences between the *Multipole Approach* and the other contemporary approaches we use violin plots with categorical axis. Here, a linear and a logarithmic scaled axis would either place the violins too close or too remote to each other, such that the plots could not highlight the differences as efficiently.

4.1 Experiments with uniform conductivity in 2D

The first experiments are intended to determine the resolution of the dipole approximation. For this purpose, our domain is a $2cm \times 2cm$ 2D square grid with uniform conductivity.

We place the dipole onto the Finite Element node in the middle of the grid and choose a homogeneous conductivity of 1 S/m.

In this scenario, the exact solution is the fundamental solution (3.3.4)

$$\Phi_{\mathrm{D}}(x) = \frac{1}{4\pi\sigma_0} \cdot \frac{\langle \overrightarrow{M}, x\rangle}{|x|^3}.$$

We prescribe Dirichlet boundary conditions with respect to this exact solution.

The error is measured as a continuous L_2-error on a small area between the chosen source location and the boundary, which is colored green in figure 4.1. We compute the forward solution for 32 different dipole moments on each monopole location.

In *UG4* we use P1 Finite Elements. The solver is a gmg–cg with a V-cycle and accuracy 10^{-12}. The monopole's strength is computed within ug4 with the LAPACK QR-algorithm [6].

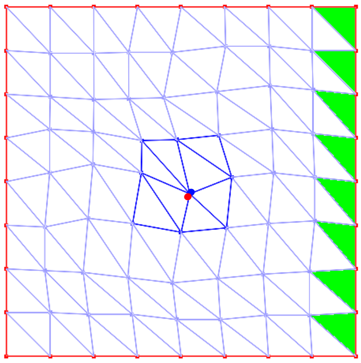

Figure 4.1: The grid used for 2D forward computations with uniform conductivity. The small dipole in the center of the grid shows the dipole location. The red lines show the border of the domain where the *Dirichlet Boundary Condition* is prescribed. We measure the L_2 error within the green triangles.

We compute the Finite Element solution on the grid, compute the L_2-Error, refine the grid, and repeat the process five times.

The *Multipole* and the *Venant Approach* are both computed with a penalty term weight of $\lambda = 1e-8$.

First, we compare the convergence rates of the mean error. The results are pictured in figure 4.2. As reference, we plot the FE interpolation of the analytical solution (3.3.4). This is the best FE representation available on the grid for linear FE.
The *Partial Integration* and the *Venant Approach* are able to gain linear convergence, whereas the *Multipole Approach* features a quadratic convergence rate here, the best possible rate for linear FE. Thus, the *Multipole Approach* is, on average, more accurate than the *Venant* or the *Partial Integration Approach*.

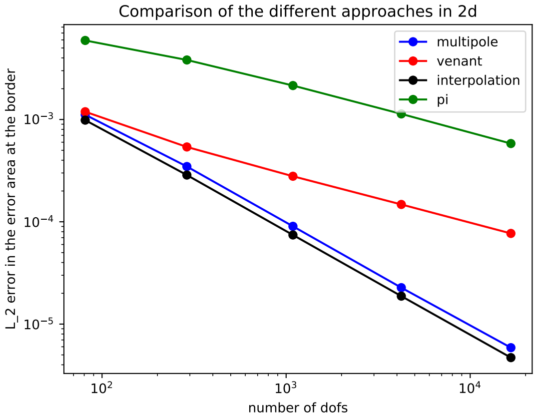

Figure 4.2: Comparison between the *Partial Integration*, the *Venant* and the *Multipole Approach* and interpolation of the analytical solution. We compute 32 forward solutions for sources at one position with 32 different moments and compare the mean L_2-error on the area of interest. The *Partial Integration*, the *Venant Approaches* are able to gain linear convergence rates. The *Multipole Approach* is able to gain quadratic convergence and therefore yields a similar result as the interpolation.

In 4.3 we plot the L_2-Errors for each of the 32 moments in a violin plot to yield additional information. We see the *Partial Integration Approach* in green, the *Venant Approach* in red, the *Multipole approach* in blue and the interpolation in black violin plots. The mean values (displayed as a horizontal black line) are the same in the violin plot and in the other plot. However, the violin plots look differently.
The *Partial Integration Approach*'s error distribution is identical in every refinement step. In most cases, the FE forward solution tends to spread across the upper part of the violin plot. The lower section is slightly longer.
For *the Venant Approach*, most forward solutions converge linearly, as can be seen by the bigger bulk around the mean error. However, there are some moments for

which the forward solutions reach the same accuracy as with the *Multipole Approach* and yield almost a quadratic convergence rate. Thus, the error spectrum grows with every step and gets much wider.

The forward solutions for *the Multipole Approach* show a narrow error spectrum. Notably, the error variance becomes wider with a finer grid. We can observe the same behavior as with the *Venant Approach*: there are some forward solutions which have a slightly better convergence rate and thus the spectrum widens. However, the differences between outliers and the mean are smaller and only become more prominent on finer grids.

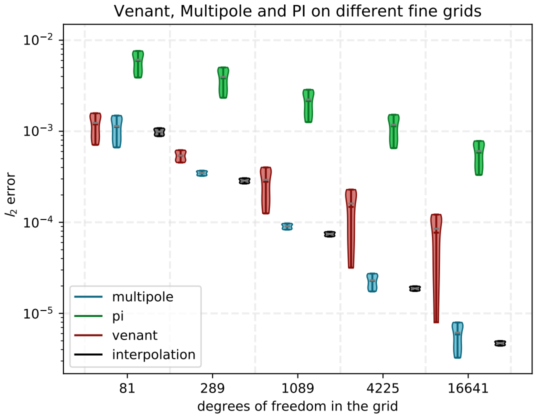

Figure 4.3: Comparison between the *Partial Integration*, the *Venant* and the *Multipole Approach* and interpolation of the analytical solution. We compute 32 forward solutions for sources at one position with 32 different moments and plot the violin plots for the L_2-error on the error area.

These results imply that the *Multipole Approach* is the best method for resolving the mathematical dipole and, thus, could be the most suitable approach for computing the *Forward Solution* with the help of FE.

4.1.1 The sensitivity of the approaches with regard to the location of the dipole

During the previous section's computations, the dipole was placed directly onto an FE node in the middle of the grid. This type of placement is ideal for the *Venant Approach* [44]. We want to know if this configuration is ideal for the *Multipole Approach* as well.

Therefore, we repeat the computations from the previous section, but with one

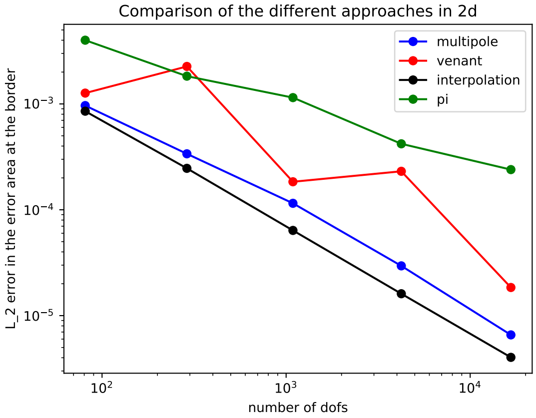

Figure 4.4: Comparison between the *Partial Integration*, the *Venant*, the *Multipole Approach* and interpolation of the analytical solution. We compute 32 forward solutions for sources at one position and 32 different moment and compare the mean L_2-error on the area of interest. The dipole is not placed on a FE node, but changes the distance to the next FE node during refinement. Therefore, the *Partial Integration* and the *Venant Approach* produce irregularities. The *Multipole Approach* has still a better convergence rate and converges similar to the interpolation.

difference: instead of placing the dipole onto an FE node, we position it at a distance of 0.086 cm from the next FE node. In our grid, the distance between nodes is in the region of $0.25 - 0.41$ cm, so this chosen location is not close to the center of a triangle.

From the result plots of the means in figure 4.4 it becomes obvious that none of the three approaches remains unaffected from the change of the dipole location. The *Venant Approach* shows an oscillating convergence behavior and is in some resolutions on average less accurate than the *Partial Integration Approach*. The *Partial Integration Approach* also shows some very small irregularities. Those irregularities show the opposing behavior to the *Venant approach*. When the accuracy of the *Venant approach* increases, the accuracy of the *Partial Integration Approach* decreases and vice versa. This might be due to the optimal placements for either the *Venant Approach* (dipole location on FE node) or the *Partial Integration Approach* (dipole location in the middle of a cell)..

In comparison, the *Multipole Approach* does not produce any irregularities. It loses the convergence rate in the first three steps. However, for a finer grid, the *Multipole Approach* again shows quadratic convergence rates but with a lesser accuracy than

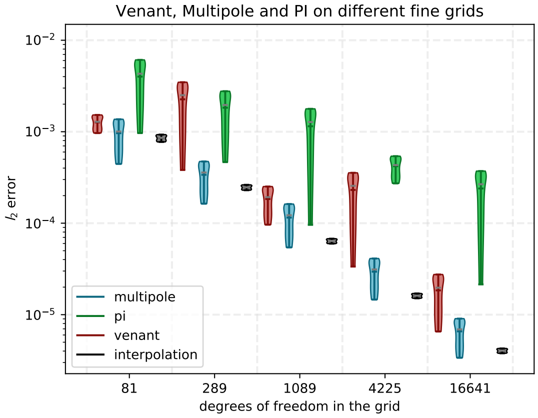

Figure 4.5: Comparison between the *Partial Integration*, the *Venant* and the *Multipole Approach* as well as the interpolation of the analytical solution for an non-node dipole location in a violin plot for 32 moments.

before.

The violin plots reveal another difference to figure 4.3: The error spectrum is wider for nearly all three approaches in figure 4.5, especially for the *Partial Integration* and the *Venant Approach*. Most of the outliers show a higher accuracy level – especially on coarser grids. In this specific aspect, the *Partial Integration* and the *Venant Approach* are able to provide a similar accuracy as the *Multipole Approach*. The violin plots produced by the *Multipole Approach* are very similar for every step and there are no outliers. The *Multipole Approach* still provides the best accuracy for all different dipole moments.

4.2 Experiments with four–layer sphere models

If the Multipole Approach is to be used for estimating brain activity, it needs to be tested with an inhomogeneous 3D model.

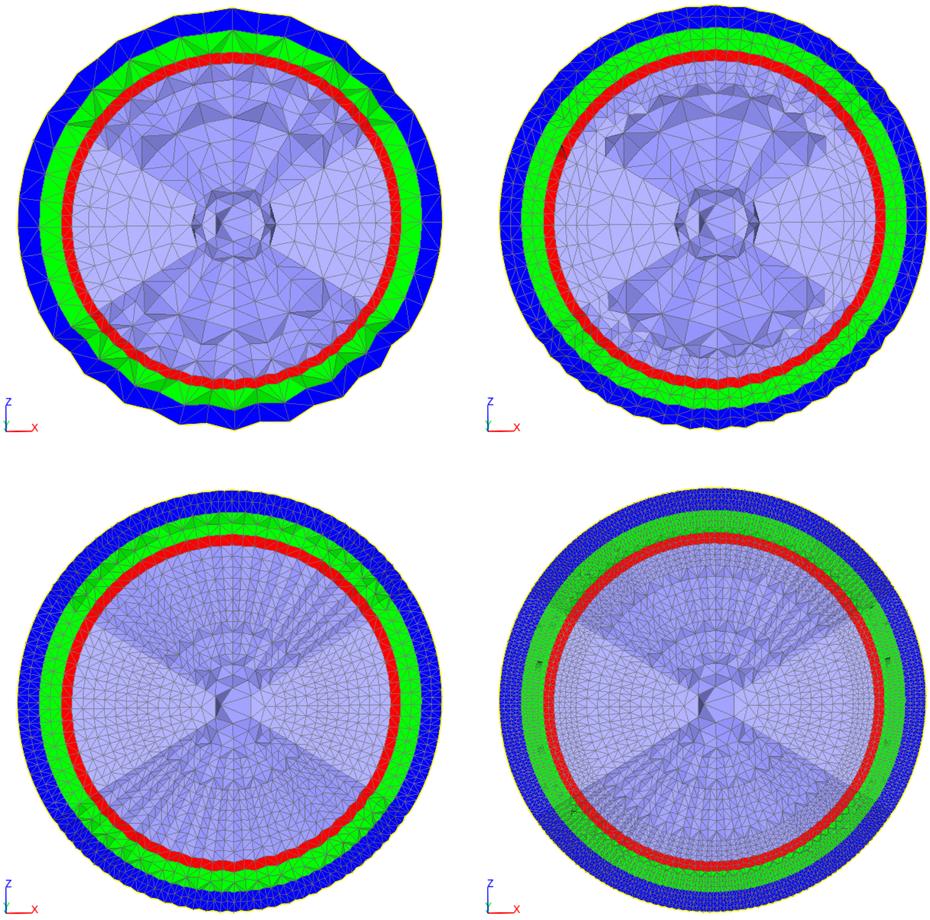

Figure 4.6: Slices of the four-layer 3D sphere models with 8382, 20398, 58488, and 421124 FE nodes.

For this purpose, we construct suitable 3D models and compare the *Multipole Approach* with other contemporary approaches.

Ideally, we would choose a realistic head model and compare the results to a reference solution. However, there are no head models which have a known reference solution.

Thus, we choose a very simplified 3D model: a series of concentrically nested

spheres.
On those models the solution can be computed point wise with a series in expansion developed by De Munck and Peters [58].
We use four spherical layers to represent four different compartments of the human head. We choose several points on the outer surface as electrical sensors to represent EEG electrode locations.
In detail, the model has an outer radius of 2.0 units. There are conductivity jumps at 1.5, 1.6 and 1.8 units. The four layers have an electric conductivity of 0.33 S/m, 1.79 S/m, 0.0042 S/m, and 0.33 S/m respectively, representing an experimental brain, CSF, bone and skin succession. We construct six variants of this model with different mesh resolutions. They consist of 6642, 8382, 20398, 58488 and 421124 nodes, respectively. In all but the highest resolution models, the distance between two finite element nodes is at least 0.2 units due to the coarseness of the mesh. From each mesh to the next finer one, we ensure that the finer one shares the FE nodes of the coarser one, see figure 4.6.

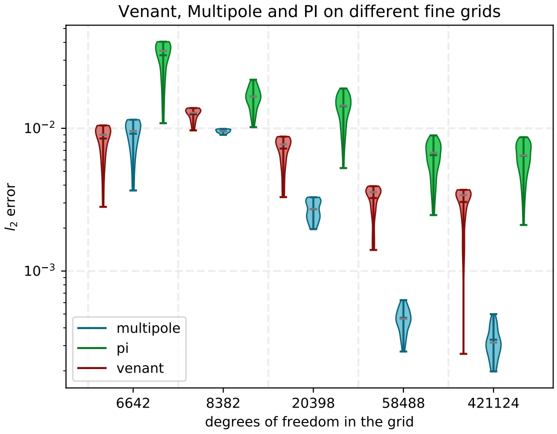

Figure 4.7: Venant, multipole and PI for four different models. The dipole was placed at $(-0.6, 0.0, 0.0)$.

On the meshes we apply P1 Finite Elements in *UG4*. The solver is a gmg–cg with a V-cycle and accuracy 10^{-12}. The strength of the monopoles was computed within *UG4* with the LAPACK QR-algorithm [6]. For the *Multipole Approach* and the *Venant Approach* we made sure that the so-called *Venant Condition* [51, 83, 82, 81] is fulfilled. Specifically, it states that all monopoles used to model the dipole are constrained to one layer of the sphere model.
We place 162 regularly distributed sensor locations onto Finite Element nodes on

the head surface. We compare the results of the *Multipole Approach*, the *Venant Approach* and the *Partial Integration Approach* at these nodes to the point wise solution postulated by De Munck and Peters.

The dipole is placed within the brain compartment. There are three variations of this location: rather close to the middle $(-0.6, 0.0, 0.0)$, a little more outside $(-1.0, 0.0, 0.0)$ and in the vicinity to the border at $(-1.2, 0.0, 0.0)$ (with the sphere center at $(0.0, 0.0, 0.0)$). The third dipole location is deliberately chosen such that in the lower-resolution models, the dipole is located next to a node that borders two distinct conductivity layers. We then compute 47 forward solutions for different moments.

Conventionally, this third dipole position would not be considered eccentric, which is usually around the distance of $2mm$. However, for the *Multipole Approach* the number of FE nodes between the dipole and the conductivity jump, rather than the spatial distance, determines the accuracy of the forward solution. Therefore, the last position can be considered as eccentric.

The results are presented in figure 4.7 to figure 4.9. Specifically, the L_2 error is displayed for all 162 sensor locations and 47 monopole moments with one violin plot. There are five groups of violin plots, one for each grid resolution. Each plot group consists of three items: the results from the *Partial Integration*, the *Venant* and the *Multipole Approach*.

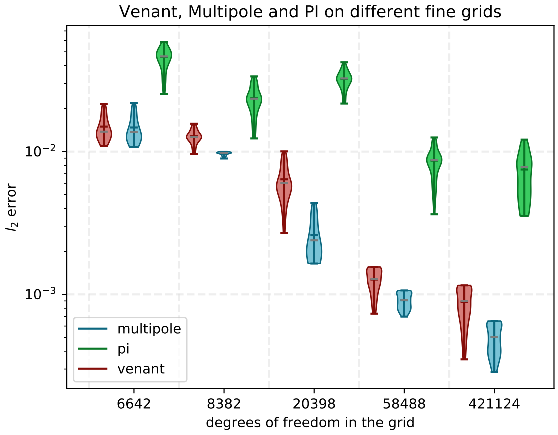

Figure 4.8: Venant, Multipole and PI for four different models. The dipole was placed at $(-1.0, 0.0, 0.0)$.

The first dipole location (see figure 4.7) is near the middle of the sphere. In this configuration, the average L_2 error for the *Multipole Approach* (displayed as a horizontal gray line) is below the average error of the *Venant Approach* and the *Partial Integration Approach*. Moreover, all types of multipole-based forward computations show superior results. The error level of the *Partial Integration* is much higher than that of the *Multipole Approach*, and significantly above the average error of the *Venant*.

The second dipole is placed 0.4 units further laterally. Again, the error of the *Partial Integration Approach* is consistently much higher than the one of the competing approaches, the *Venant* and the *Multipole Approach*. The accuracy spectra of the *Multipole* and *Venant Approach* (see Figure 4.8) overlap partly. However, a brief statistical analysis shows that the results from the *Venant* and *Multipole Approach* differ significantly (pairwise two–sided t–test: $t > 8.0, p < 0.0001$).

The third dipole is located near the conductivity jump (at X–position -1.5) of the innermost compartment. Again the *Partial Integration* level of error is consistently higher than the one of the *Multipole Approach* and overlaps slightly with the level of the *Venant Approach*. The error level from the *Venant Approach* fails to improve on models with a higher resolution. In contrast, the *Multipole Approach* does improve with an increasing grid resolution. The level of accuracy of the *Venant Approach* and the *Multipole Approach* in the grid with 20398 nodes overlap with each other, but the difference is again significant ($t > 5.0, p < 0.0001$).

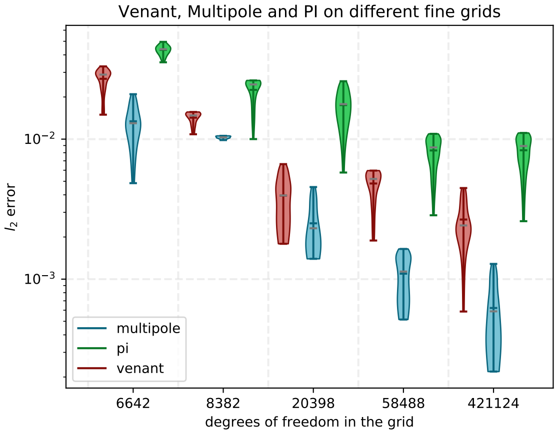

Figure 4.9: Venant, multipole and PI for five different resolutions. The dipole was placed at $(-1.2, 0.0, 0.0)$.

These results indicate that the *Multipole Approach* consistently yields a higher accuracy when computing forward solutions.

4.3 A goal function scan - a manual inverse algorithm

To find out if our forward solution algorithm is suitable for use in inverse computations, we employ a goal function scan.

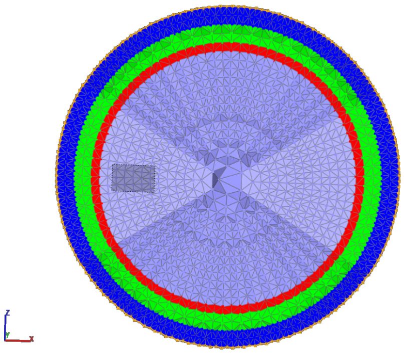

Figure 4.10: Four–layer sphere model with 58488 elements. Jumps are at 1.5, 1.6 and 1.8 and outer radius is 2.0. The patch is displayed in grey in the middle compartment. Its corners are located at $(-0.15, 0.0, -0.75)$, $(0.15, 0.0, -0.75)$, $(-0.15, 0.0, -1.35)$, and $(0.15, 0.0, 1.35)$.

A goal function scan can be understood as a brute force variation of an inverse algorithm, and was proposed by T. Knösche [38].

Numerous dipoles are placed within the head model where brain activity is possible. For each of these dipole locations, forward solutions are computed for moments along the Cartesian directions. Then, we compare the linear combination of the forward solutions with the presented activity at the sensor locations and compare the accuracy with regard to the distance from the reference location.

For our goal function scan, we choose the regular four–layer 3D sphere model and place a 2D patch with corner coordinates $(-0.15, 0.0, -0.75)$, $(0.15, 0.0, -0.75)$, $(-0.15, 0.0, -1.35)$, and $(0.15, 0.0, 1.35)$ inside. We ensure that the cells around this patch are regularly shaped (specifically that they have a similar diameter). This property is optimal on the grid with 58488 nodes, so we continue with this variant. For comparison: during the 3D forward computations, the *Venant Approach* and the *Multipole Approach* yield a similar accuracy spectrum on this grid.

Then we place 264 dipole locations regularly into the 2D patch and compute the FE solution at the sensor locations. This process is repeated three times, using each of the three Cartesian destinations as moments for the dipole respectively.

We compute several reference dipole solutions within the patch by using the De Munck solution of fieldtrip. Those 21 reference solutions are aligned in the middle of the patch and reach from the inside of the ”brain” compartment (X-coordinate:

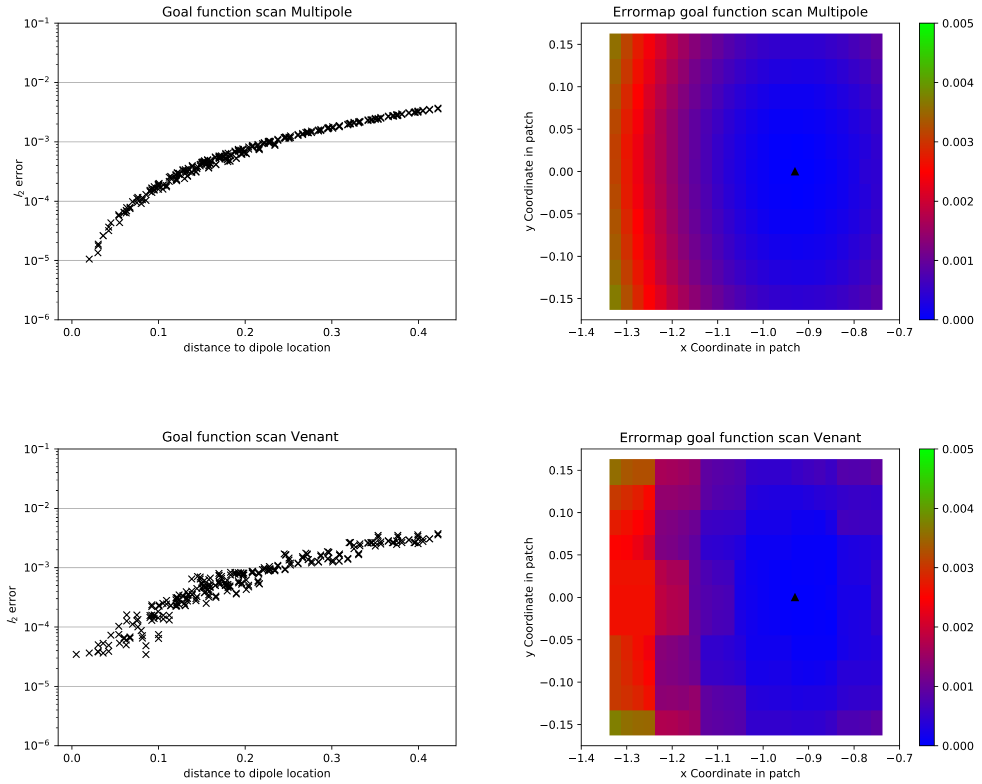

Figure 4.11: l_2 errors for 264 estimated dipole locations to one reference dipole location. The reference dipole was placed at $(-0.93, 0.0, 0.0)$. The dipole moment is $(0.07..., 0.07..., 0.995...)$. Above: Multipole, below: Venant.

-0.75) to the next conductivity jump at the skull layer (X-coordinate: -1.3).

For every dipole location we minimize the l_2 error between the reference dipole solution and any linear combinations of the three computed FE solutions.

Let u_{ref} be a reference solution at the sensor positions. So for any location x_i, we compute the forward solutions $\varphi_{x_i,1}, \varphi_{x_i,2}$ and $\varphi_{x_i,3}$ for the moments in the three Cartesian directions $(1.0, 0.0, 0.0)$, $(0.0, 1.0, 0.0)$ and $(0.0, 0.0, 1.0)$ at the sensor positions. Minimizing the l_2 error against the reference solution u_{ref} then means to minimize the functional

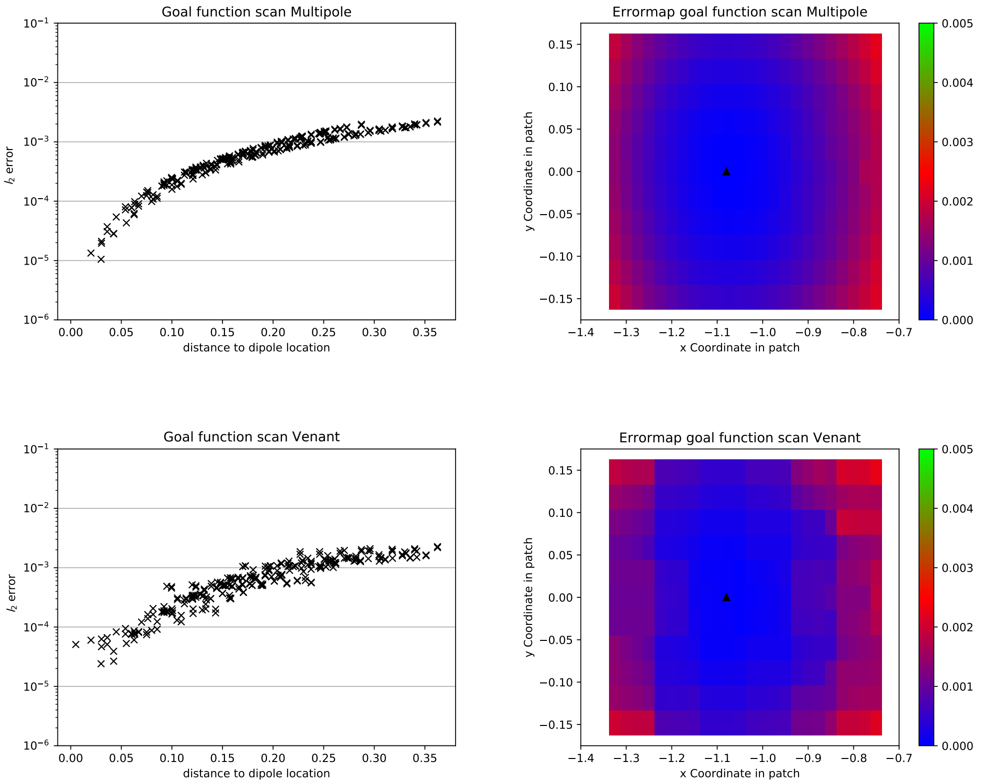

Figure 4.12: like 4.11 but with reference dipole X-coordinate at -1.08. Multipole is above, Venant is below.

$$\left\| u_{\text{ref}} - (\varphi_{x_i,1}, \varphi_{x_i,2}, \varphi_{x_i,3}) \cdot \begin{pmatrix} \alpha \\ \beta \\ \gamma \end{pmatrix} \right\|_2 \tag{4.3.1}$$

for $\begin{pmatrix} \alpha \\ \beta \\ \gamma \end{pmatrix} \in \mathbb{R}^3$. We can do so using a standard orthogonal decomposition. Alternatively, we could use normal equations. However, for these, the condition of the matrix plays an important role for the stability. Thus, orthogonal decomposition is preferable in this case [21].
The results of three representative dipole locations are displayed in figures 4.11, 4.12, 4.13.

The images on the left display localization accuracy with respect to the distance between the estimated and the reference dipole locations. The error range of the *Venant Approach* is similar to the error range of the *Multipole Approach*. For both approaches, the accuracy increases when the distance to the reference dipole decreases. However, the results from those two approaches are rather different in detail.

The *Venant Approach* shows a convergence rate with distinguishable steps. The accuracy for locations of similar distance vary noticeably, and a considerable number of local minima and maxima is produced.

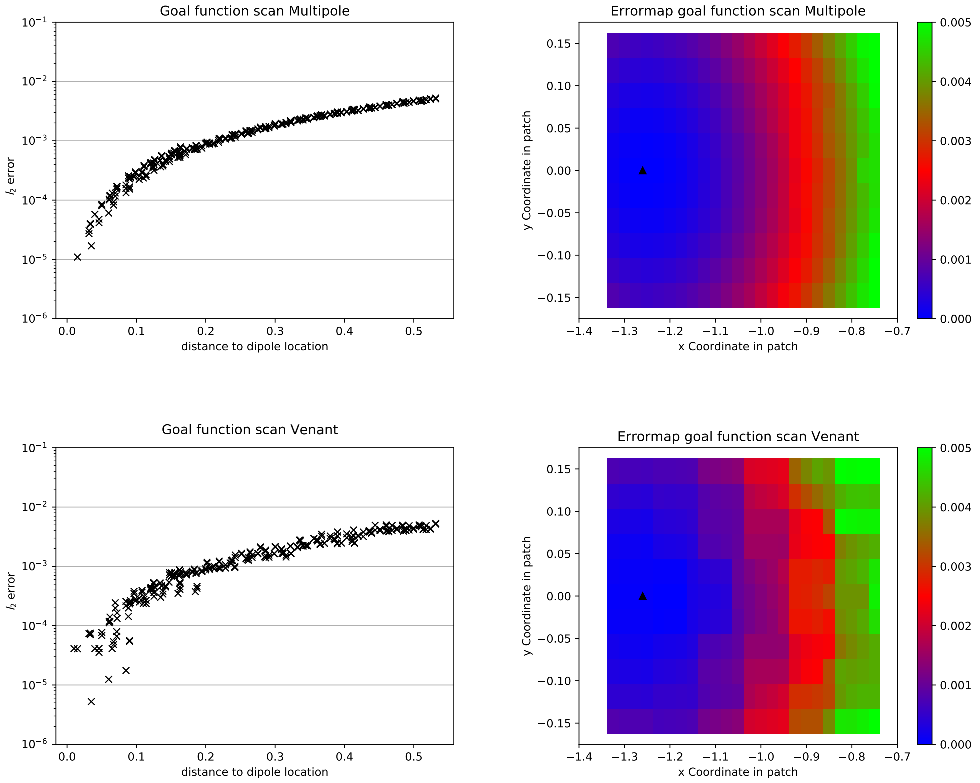

Figure 4.13: l_2 errors between those 264 dipole locations and the real dipole. The reference dipole was placed at $(-1.26, 0.0, 0.0)$ and has dipole moment $(0.06955..., 0.0716161..., 0.9950041...)$. Multipole is above, Venant is below.

In comparison, the *Multipole Approach* converges much more smoothly. The accuracies for locations of similar distance show clustering along one or more converging smooth patterns. Those patterns are similar, especially in figure 4.12. This approach therefore produces local minima and maxima in this kind of plot, but with a smaller amplitude than the artifacts created by the *Venant Approach*.

Inverse algorithms do not deal well with local minima. However, this kind of plot cannot give an accurate understanding about local minima since it compresses a small 2D structure in a 3D model into a 1D representation. To get a better impression about local minima and maxima, we also created an error map. This chart is shown on the right side of the figures 4.11, 4.12, and 4.13.

Those images display the 2D patch as a color-coded map. Visually, there are 264 distinguishable rectangles in this patch. We place one of the 264 dipoles in the middle of each rectangle. Then, we color each rectangle according to the accuracy of this dipole in comparison to the reference dipole.

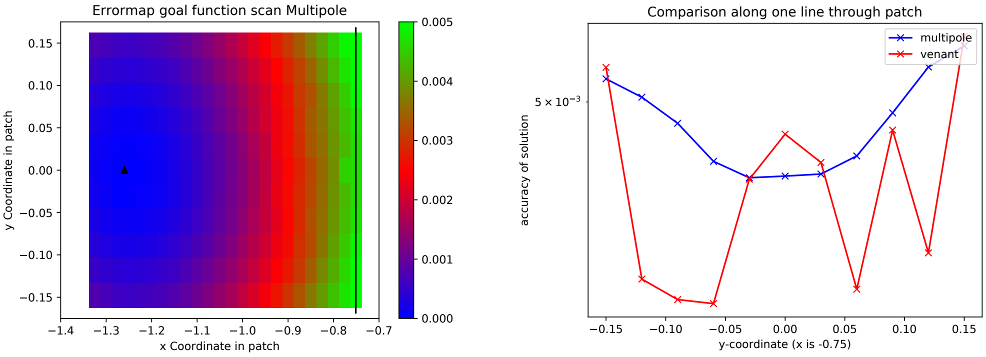

Figure 4.14: We pick the errors along one straight line through the patch 4.13. The line is indicated in the left image on the already shown error map. In the right image you can see the accuracy of the *Venant* (red) and *Multipole* solutions (blue). The coordinate with minimal distance to the original dipole is at $y = 0.0$. The multipole solutions have no local extrema and are minimal around the wanted y-coordinate. The Venant solutions show a lot of local extrema.

On this map, we can see the behavior of the two approaches in detail. The error magnitude decreases from the outside of the model to the reference dipole location (which is indicated by a small black triangle).

The *Venant Approach* shows distinct steps. The steps are clustered around FE nodes, hinting at the cause for the popular recommendation to use the *Venant Approach* only with grid nodes as possible dipole locations. These steps pose the biggest practical problem with the *Venant Approach*. If we imagine a straigt line through the patch and plot the error magnitude along the way, the resulting plot would show local minima and maxima, for example as in figure 4.14. For this reason, this approach should only be used in inverse computations when dipole locations are placed onto FE nodes. However, doing this effectively would require a rather fine grid resolution.

In comparison, the *Multipole Approach* does not show those distinct steps. The error map is very smooth, which – with the same line as before – does not result in locally minimal or maximal error amplitudes. The aforementioned artifacts in the distance vs. accuracy plots are caused by different convergence rates from different directions. To understand this behavior, consider that in the error maps, the areas of identical accuracy levels are oval rather than circular.

Due to the smooth result pattern, the *Multipole Approach* is highly suitable for use in inverse computations, independently of dipole placement. The *Multipole Approach* could reach even higher accuracy on coarser grids, resulting in a lower computational time. This is a highly desirable property for solving the inverse EEG forward problem.

4.4 Pitfalls for Multipole computation

The results presented in the last chapters are consequences of an optimization process. There are several parameters to choose in the *Multipole Approach*, which have been deliberately obscured until now. But in order to yield results with the best possible accuracy, we need to discuss the path to optimize these parameters.

At first, we ensure the fulfillment of the *Venant condition* [51] for the *Multipole Approach*, which – as described in the last chapter – entails placing all monopoles into the same conductivity layer.

There are two additional parameters to configure:

1. The number of monopoles to represent the dipole. The *Venant Approach* implemented in the original SimBio framework [32] and the SimBio-fieldtrip framework [64] determines this number as follows:
   a) first, it finds the FE node closest to the original dipole location,
   b) second, this node and all directly connected neighbor nodes (via an edge or a face) are designated as monopole locations.

   This strategy might lead to problems. With fewer monopoles, there is a chance that the monopole locations are not uniformly distributed around the dipole location. In this case, the dipole potential can't be represented accurately in all directions. Therefore, it makes sense to examine which general numbers of monopole location will yield good results.

   To examine this effect, we modified our algorithm. First, we set a desired number of monopoles. Second, like in SimBio, we select the FE node that is closest to the dipole location. Third, we select all connected FE neighbors to that first node. Fourth (the modification), if the total number of selected monopoles does not reach our desired number, we add any unselected FE nodes that are closest to the original dipole location and within the desired layer.

2. The $\lambda \in \mathbb{R}$, which weighs the penalty term. If λ is too big, the solver for minimizing the functional (3.3.12) favors the penalty term over the multipole conditions. Therefore, the dipole will not be resolved as well as it would be with a smaller λ. Additionally, for a big λ, the multipole conditions might not be fulfilled at all. This edge case is especially unfavorable if the compatibility condition of Neumann problems (in this case, $0 = \sum_{i=1}^{m} q_i$) is not fulfilled. The compatibility condition is part of the multipole conditions. If this condition is not fulfilled, the Finite Element solver is unable to compute a solution. A λ which is too small, on the other hand, might lead to instabilities.

Next, we discuss the parameter settings in the context of the numerical experiments. First, we will see how the choice of the number of monopoles and λ will affect the outcome in the $2d$ uniform conductivity setting. Second, we repeat those computations for the 4layer 3D setting. Finally, we will bring these results into the context of the goal function scan.

4.4.1 The penalty weight and the number of neighbors in 2D experiments

In our first test, we vary the number of monopole locations in the 2D setting.
The *Simbio* module yields a number of 7 monopoles. As visible in figure 4.15 there is only one monopole available to represent the dipole potential towards the upper right and the lower left direction. This will lead to problems, because one node cannot portray a dipole for opposite directions. This setup could be improved if the FE nodes in the upper right and the lower left corner could be employed as well to portray the dipole.

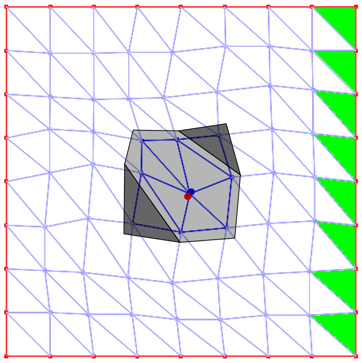

Figure 4.15: The grid used for 2D forward computations with uniform conductivity, explained in figure 4.1. The *Simbio* monopole computation algorithm will only compute the FE nodes within the light grey area. Those are the FE nodes connected with the node of least distance to the dipole location (which is the middle in our case). We fixed the algorithm in such a way that in the next step, the lower left node in the darker gray area will be also chosen as a monopole location (for 8 nodes) and the upper right node in the other darker grey area next (for 9 nodes).

With our modification of the algorithm computing the monopole, the next two chosen locations are exactly these nodes, since they are closer to the dipole location than any other (not previously selected) node.

In this context we compare the forward solutions of 7, 8, 9, and 10 used monopole locations to represent the dipole.

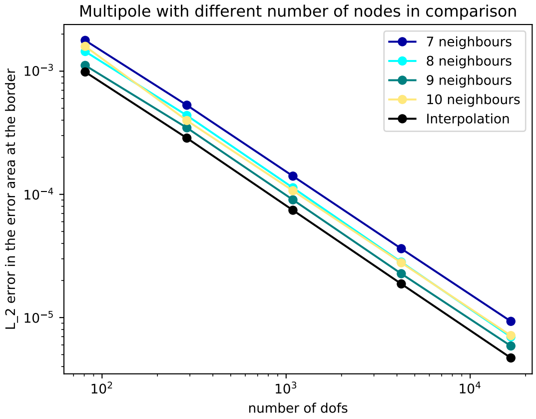

Figure 4.16: Comparison between 7, 8, 9, and 10 FE nodes used as monopole locations for the *Multipole Approach* and interpolation of the analytical solution. We compute the forward solutions for one dipole location and 32 directions and plot the mean L_2-errors on the error area in a convergence plot.

When we compare the mean L_2 errors, we see that all convergence rates are similar. The number of monopoles mainly affects the convergence offset. The optimum for our grid is a number of 9 monopole locations.

There is an intuitive explanation for this result. If we choose too few locations, there might be areas without a monopole between the dipole location and the border of the domain. Therefore, in this area the electric field will be more distorted. If we choose too many locations, the distance between the chosen monopole location and the location where the error is computed is too close. Therefore, the electric field will be more distorted in this case as well.

Consequently, there is a number of monopole locations leading to optimal results. In our 2D case with a relatively regular grid, the number is 9.

We repeated this optimum search with different values for λ as weights for the penalty term.

Values for λ in the range of $1e-4$ to $1e-16$ [1] yield similar results. The values of $\lambda = 0.01$ and $\lambda = 0.1$ did not produce good results.

---

[1] We here use the common scientific notation with $1e-3 = 0.001$, $1e-4 = 0.0001$ to be able to distinguish between those of multiples of 10.

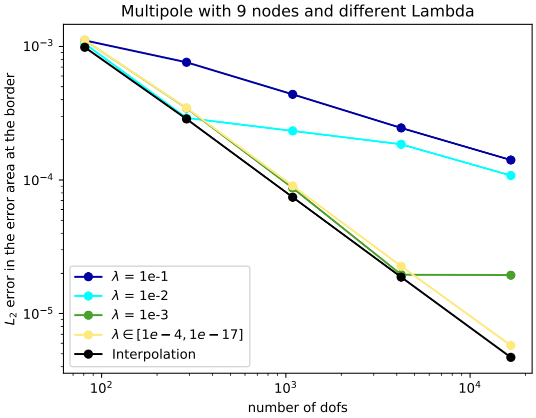

Figure 4.17: Comparison between the *Multipole Approach* for different penalty weights and interpolation of the real solution in a violin plot for 32 moments

$\lambda = 1e-3$ is notable because it yields results similar to values of $\lambda \in [1e-4, 1e-16]$ but stops converging early. This happens when the distance between the monopole locations and the dipole are in the same order of magnitude as lambda.

This observation implies that there is a simple heuristic for choosing an optimal λ for 2D computation: any value of $\lambda \in [1e-4, 1e-16]$, together with 9 monopole locations should be optimal.

Our next step is to examine if there is a similar simple heuristic for the 3D case as well.

4.4.2 Forward experiments in 3D with the penalty term and the number of neighbours

First, we repeat the experiments of Section 4.2 while using a wide array of different λ.

We specifically vary λ in the powers of 10 between $1e+2$ and $1e-16$ and also 0. With λ values above 0.1, the forward computations are unstable and fail to be completed. Even for the choice of 0.01 and 0.001, some dipole configurations lead to failing computations.

The reason for this instability lies with the solver of problem (3.3.12). A big λ causes the optimization to be biased more towards the penalty term than towards the multipole conditions. Since the necessary condition $0 = \sum_{i=1}^{m} q_i$ is part of the multipole conditions, neglecting them causes the solution to fail.

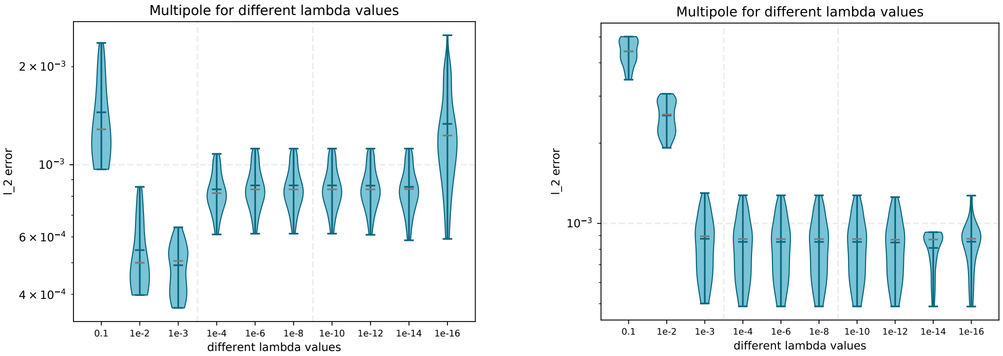

Figure 4.18: Comparison between the *Multipole Approach* on a four–layer grid with 58488 elements. In the left image are the errors for a case where there are not enough neighbors to the dipole location. This is the case at $(-0.7, 0.0, 0.0)$. Here, the choice of $\lambda = 0.001$ is the best. In the right image are the errors for a case where there are enough neighbors to the dipole location. This is the case at $(-1.0, 0.0, 0.0)$. Here any choice for $\lambda \in [1e-3, 1e-16]$ seems to be good.

The value of $\lambda = 0$ also yields unstable results.
We do not plot the unstable configurations (λ bigger then 0.1 and equal to 0), we focus on the influence from λ values for stable λ and from the number of monopole locations.
We can distinguish two general cases:

1. the *Simbio*–neighbor computation yields a sufficient number of monopole locations.
2. the *Simbio*–neighbor computation yields an insufficient number of monopole locations.

In the first case, a $\lambda \in [1e-3, 1e-10]$ provides good results with similar accuracy to each other (at least if there is a successful solution for $1e-3$). Even if the dipole location moves to the conductivity jump, a $\lambda \in [1e-3, 1e-10]$ yields a favorable accuracy.
The second case is more interesting. Here, if we choose a $\lambda = 0.001$ we obtain a slightly better accuracy than in the case of a $\lambda \in (1e-3, 1e-10)$. If we add additional monopole locations, the accuracy levels are overall higher.
Next, we examine the optimum of monopole locations, and show possible pitfalls for using the *Multipole approach* in an inverse setting.

4.4.3 Goal function scan

The two parameters, λ and the number of monopoles, will also affect inverse solutions. To examine this effect, we compute the goal function scan with a set of different parameters.

We choose $\lambda = 1e - 8$ for a start.

In the first scenario, we use the *Simbio* search algorithm for computing monopole locations. For most dipole locations, this algorithm yields a sufficient number of neighboring grid nodes. In the remaining cases, optimizing the forward solutions yields outliers (see figure 4.19). In our model, there are four critical FE nodes: three within the brain compartment, and one directly at the border. For the last case, the *Venant Condition* also contributes to the distortion.

Thus, an inverse algorithm solver cannot work properly to compute the location of global minimal accuracy. It will be disturbed be all the local minima around the outliers. In order to make the *Multipole Approach* fit for use in inverse computation, this issue needs to be remedied.

The second setting involves a mitigation strategy. If the *Simbio* algorithm selects an insufficient number of monopole locations, we increase the weight of the penalty term λ to 0.001. This value of λ was established to be optimal for this condition during the previous experiments. This strategy ends up ameliorating the problem, but cannot completely solve it (see figure 4.20). The outliers decrease in magnitude but are still visible. The discontinuities and local minima continue to pose a hindrance to inverse algorithms.

For the third scenario, we modified the *Simbio*–based algorithm of neighbor selection. If the selected number of monopole locations was lower than predetermined, we added the closest nodes until the number was reached. The results for 8, 13 and 16 monopole locations are pictured in 4.21.

Refining this successful scenario, we focus on the seemingly optimal number of $11 - 13$ monopole locations. Results from goal function scans for three different dipole locations are pictured in 4.22.

These results show a continuous error surface with no apparent outliers even in critical dipole locations. Especially the dipole location affected by the *Venant Condition* produces favorable results as well.

In light of these results, we suggest to always employ our modified monopole location algorithm, and to fill up to a number of $11 - 13$ neighbor nodes when computing the *Multipole Approach.*

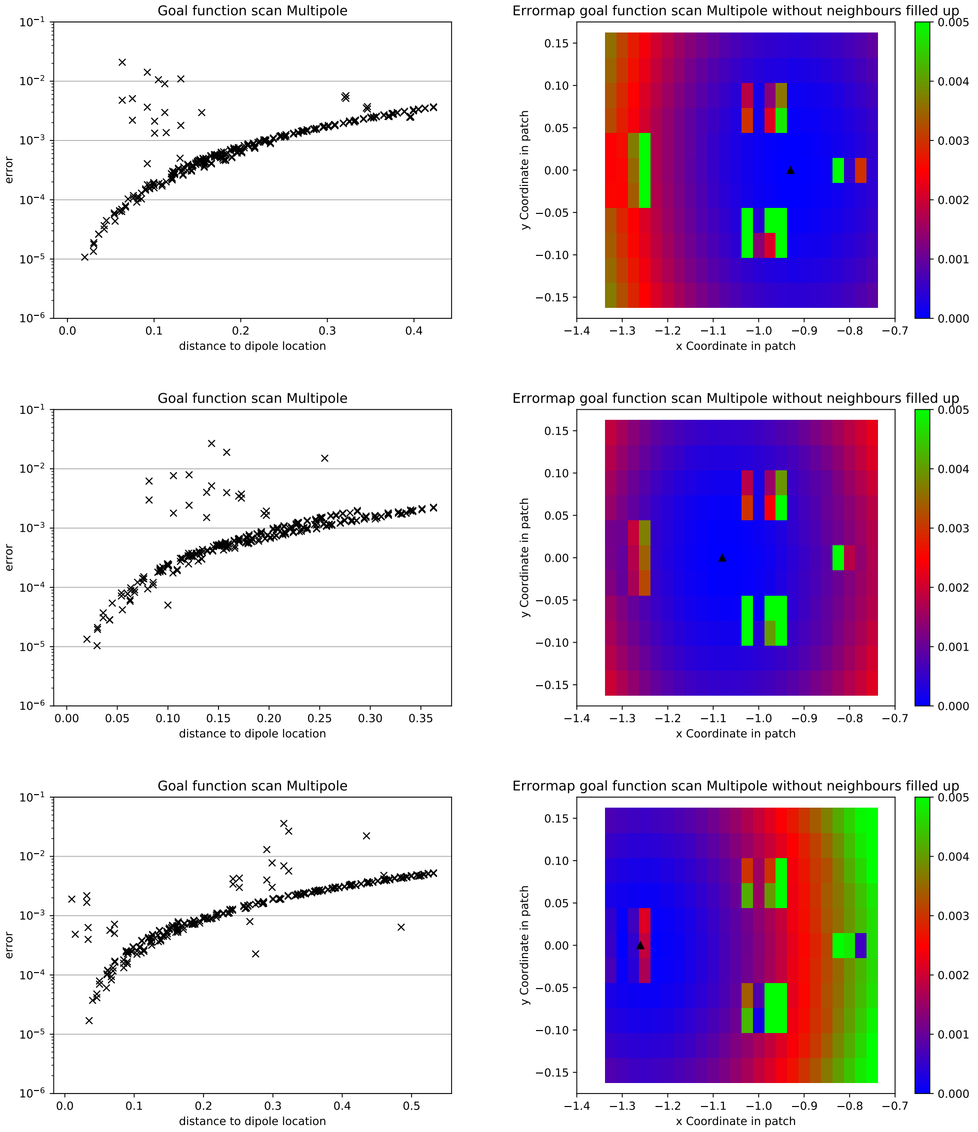

Figure 4.19: l_2 errors between those 264 dipole locations and the reference dipole. From top to bottom we use the same configurations as figures 4.11, 4.12, 4.13.

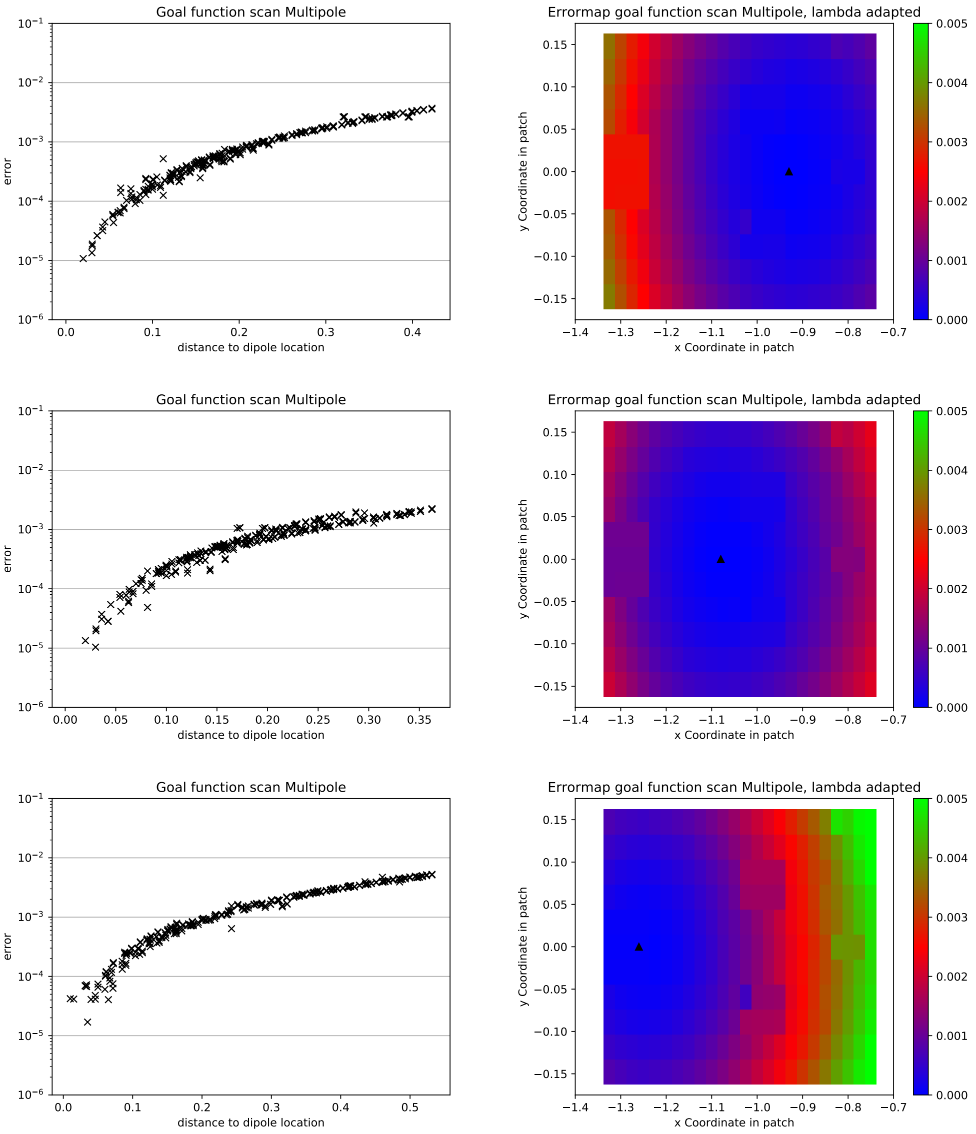

Figure 4.20: l_2 errors between those 264 dipole locations and the reference dipole. From top to bottom we use the same configurations as figures 4.11, 4.12, 4.13. Multipole with $\lambda = 0.001$ at those locations, where fewer than 13 monopole locations were computed.

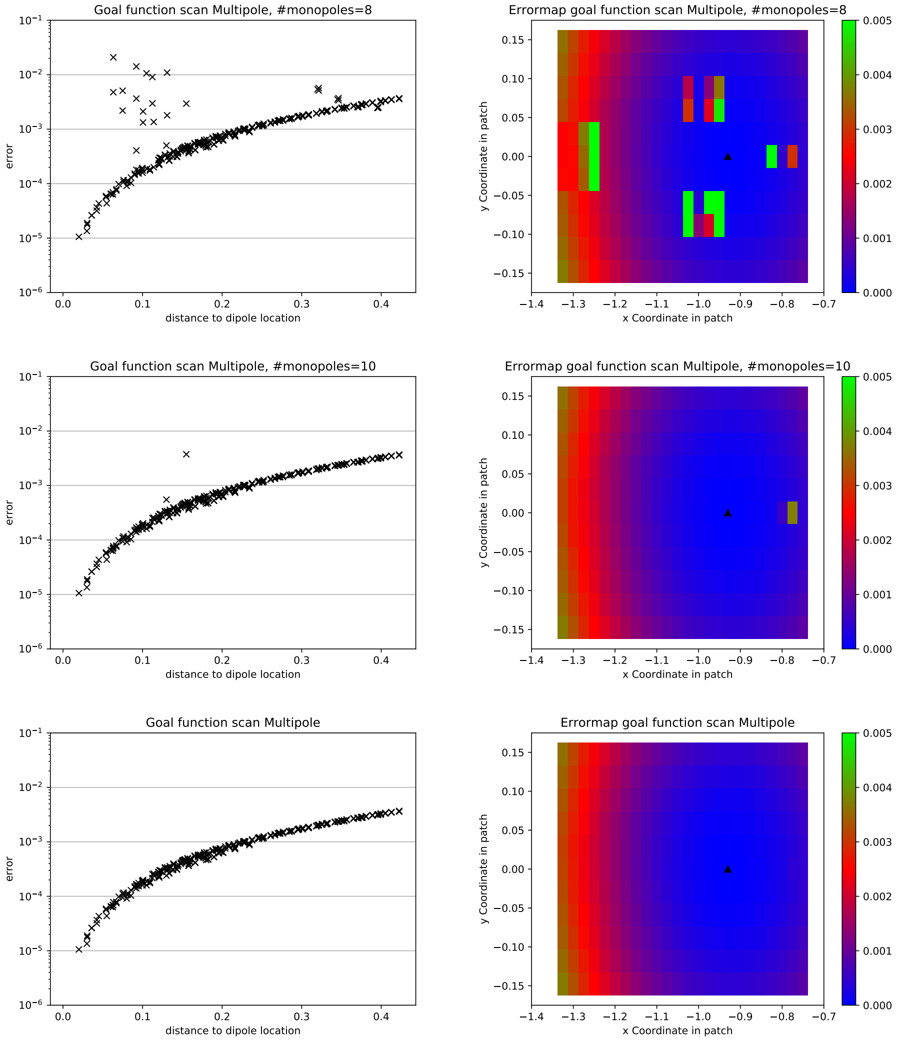

Figure 4.21: l_2 errors between those dipole locations and the reference dipole. We computed such, that we had at least 8 monopole locations in the upper computations, at least 10 in the middle one and 13 in the last one. We used the same dipole setting as in figure 4.11.

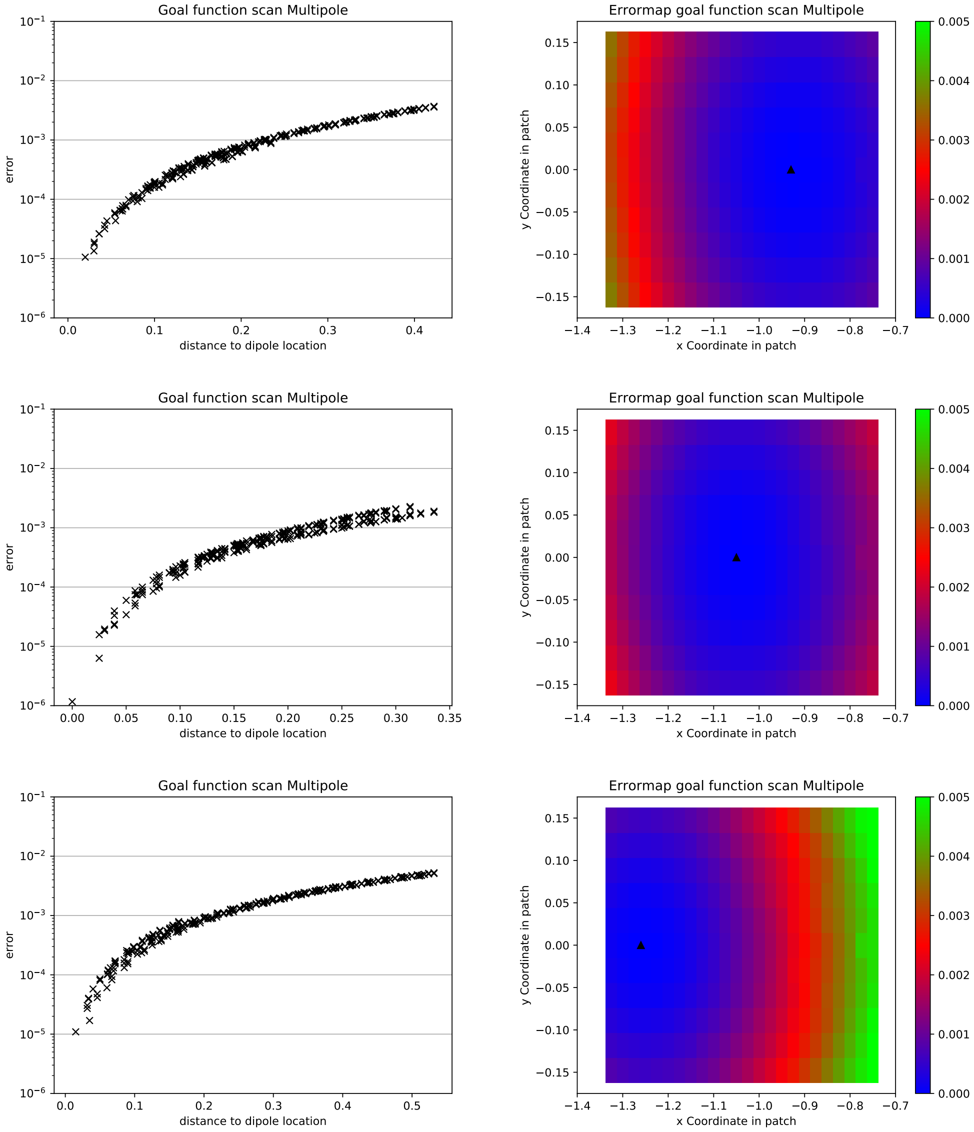

Figure 4.22: l_2 errors between those dipole locations and the reference dipole. From top to bottom we use the same configurations as figures 4.11, 4.12 and 4.13. For the Multipole we add more locations (of minimal distance), if fewer than 13 locations are computed in the first case.

4.5 Results of numerical computations with the classical errors

In established studies for EEG forward computations, the RDM and the MAG error measures are used to judge the accuracies of approaches to solve the EEG forward problem. Specifically, those measures deal with different characteristics of the accuracy [52].

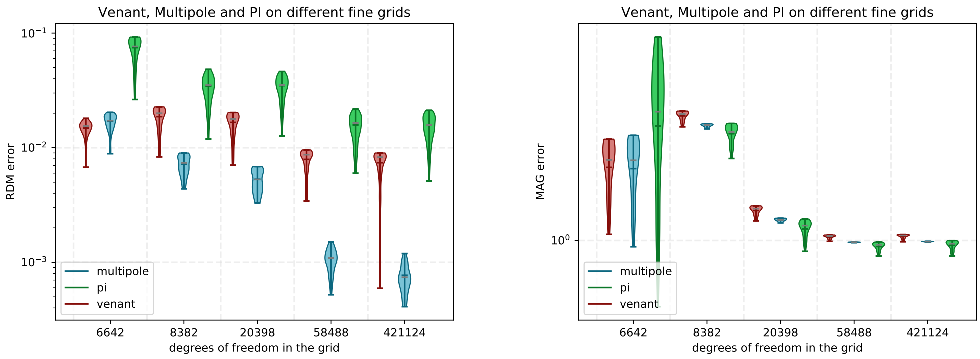

Figure 4.23: Venant, multipole and PI for five different models. The dipole was placed at $(-0.6, 0.0, 0.0)$.

Let u_{sens} describe the discrete values of the FE solution at a certain number of m sensor positions and u_{DM} the discrete values of a De Munck and Peters sphere solution. We then compare those in terms of the RDM and MAG.
RDM is an abbreviation for *relative difference measure* and the error is defined by

$$RDM(u_{\text{sens}}, u_{\text{DM}}) := \left\| \frac{u_{\text{sens}}}{\|u_{\text{sens}}\|_2} - \frac{u_{\text{DM}}}{\|u_{\text{DM}}\|_2} \right\|_2 .$$

It is a measure for the topographic error and bounded from above by 2.
MAG is an abbreviation for *magnitude error*. It is defined by

$$MAG(u_{\text{sens}}, u_{\text{DM}}) := \left\| \frac{u_{\text{sens}}}{u_{\text{DM}}} \right\|_2 .$$

In contrast to the RDM and the l_2 error, it has 1 as the optimal value.
We have already computed forward solutions for the *Venant Approach*, the *Multipole Approach* and the *Partial Integration Approach* on several sphere models in chapter

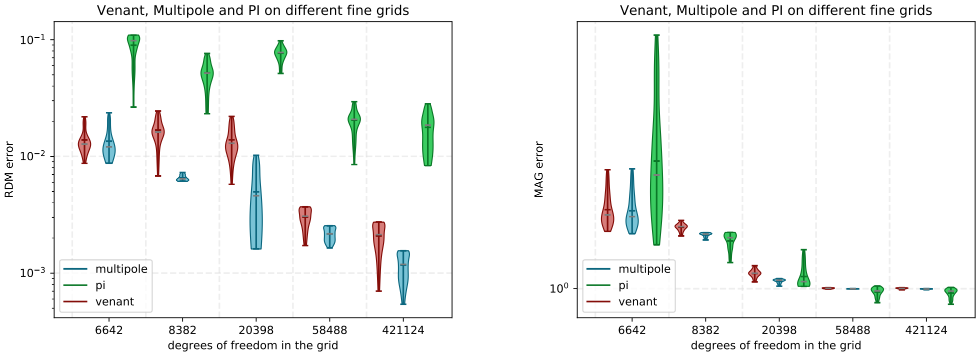

Figure 4.24: Venant, multipole and PI for 4 different models. The dipole was placed at $(-1.0, 0.0, 0.0)$.

4.2. In this context, we can revisit the results at the sensor positions. But instead of computing the l_2 error, this time we compute the RDM and the MAG error. Whereas the RDM error displays analogous behavior as the l_2 error presented in chapter 4.2, the MAG error shows a different distribution.

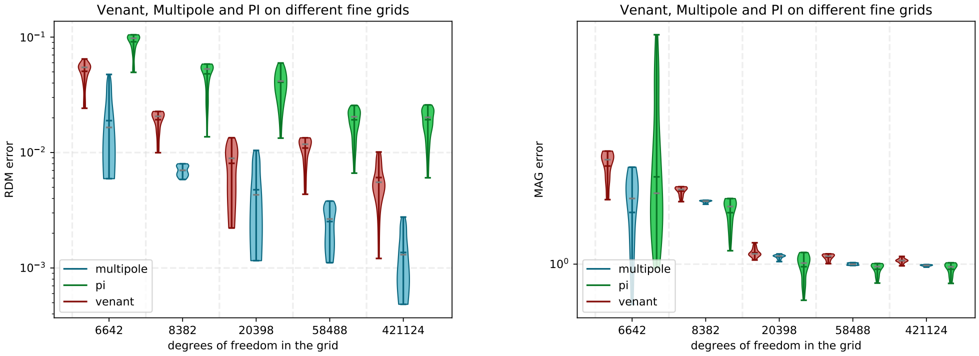

Figure 4.25: Venant, multipole and PI for 4 different models. The dipole was placed at $(-1.2, 0.0, 0.0)$.

The MAG error of all three approaches converges to 1 the finer the grid gets. Notably, the *Multipole Approach* shows the smallest error variance, and the fastest convergence with increasing grid resolution. This behavior is independent of the location of the dipole. Even if there are not many FE nodes between the dipole location and the next conductivity jump, the MAG error converges to 1.

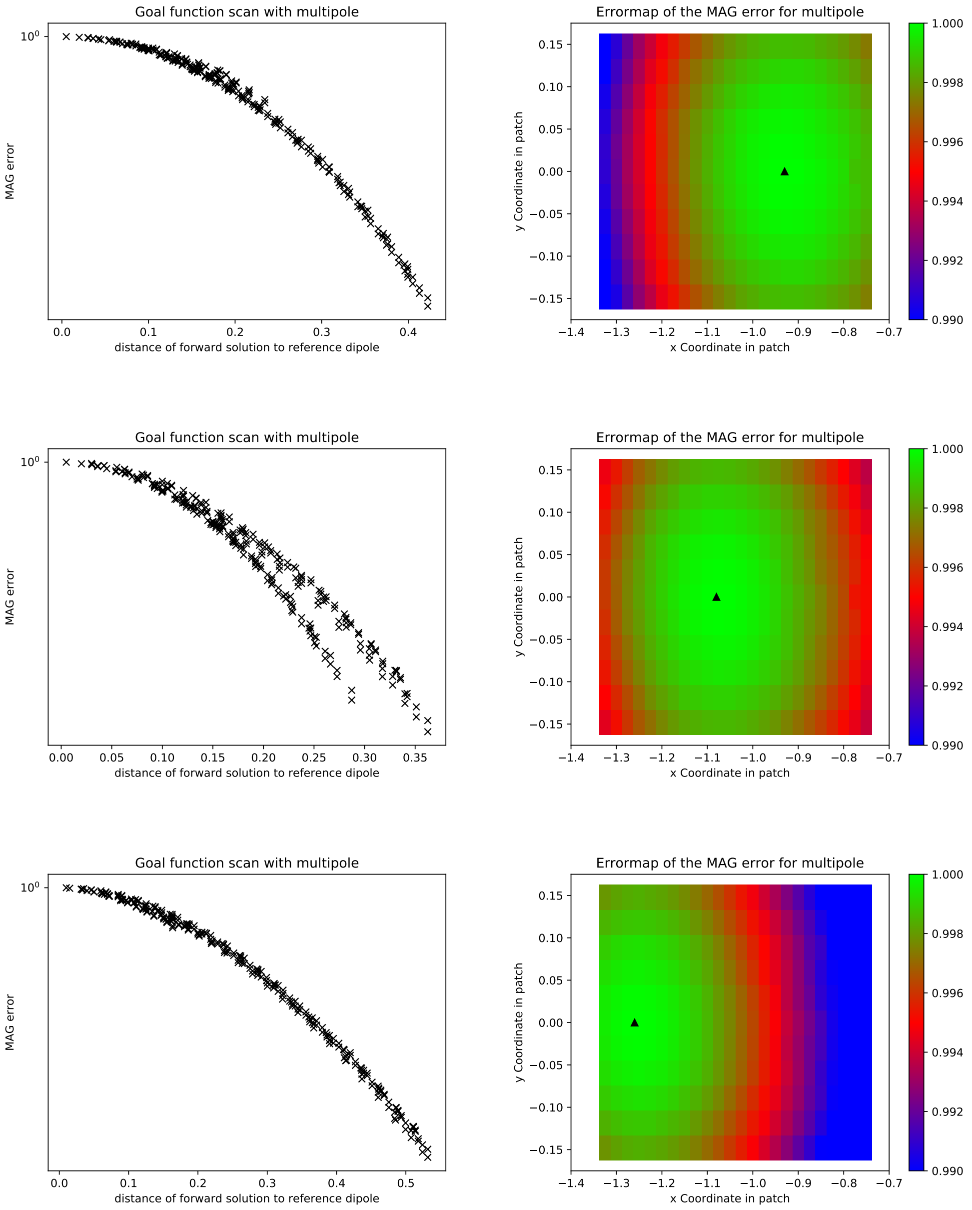

Figure 4.26: MAG errors between those 264 dipole locations and the real dipole. We used from top to bottom the same dipolar settings as in 4.11, 4.12 and 4.13.

We also can compute the RDM and MAG errors for the goal function scan. Here, we can compute the minimum linear combination we get out of minimizing the functional (4.3.1) and afterwards use this forward solution to compute the RDM and the MAG error.

We compute the MAG error for the *Multipole Approach*. Here, we can clearly see that error development of the accuracy is not circular but rather elliptic, which explains the two different converging lines in the middle plot and some bulkier looking parts of 4.26.

We compare the RDM measures for the forward solutions of the *Venant Approach* and the *Multipole Approach*.

We plot the results of the RDM error in relation to the distance between the reference solution on the left side and the minimizing forward solution or an error map of the RDM error on the right side. Figures 4.27 show the the *Multipole Approach* and 4.29 the *Venant Approach*.

The images of the *Venant Approach* show a heavily scattered behavior. We can see distinct steps in the error map. However, the behavior in the distance-to-accuracy plot on the left shows a much wilder and unstructured picture. Here, a search for a global minimal value will definitively be hindered by the existence of local minima. Thus, we cannot employ the *Venant Approach* as is for inverse calculations.

We have to point out again that we used the *Venant Approach* contrary to its normal usage: we did not place the dipole location onto a FE node.

On the other hand we have a very smooth behavior for the *Multipole Approach*. Here, we can observe again the elliptic accuracies around the original dipole location in the error maps, which lead to the bulkier parts in the distance-to-accuracy plot on the left. However, an inverse solver will not be disturbed by this, since there are no local minima along any line through the patch, where the solver will look for a global minimum. Therefore, the *Multipole Approach* can be used for inverse computations with the modifications of the last chapters.

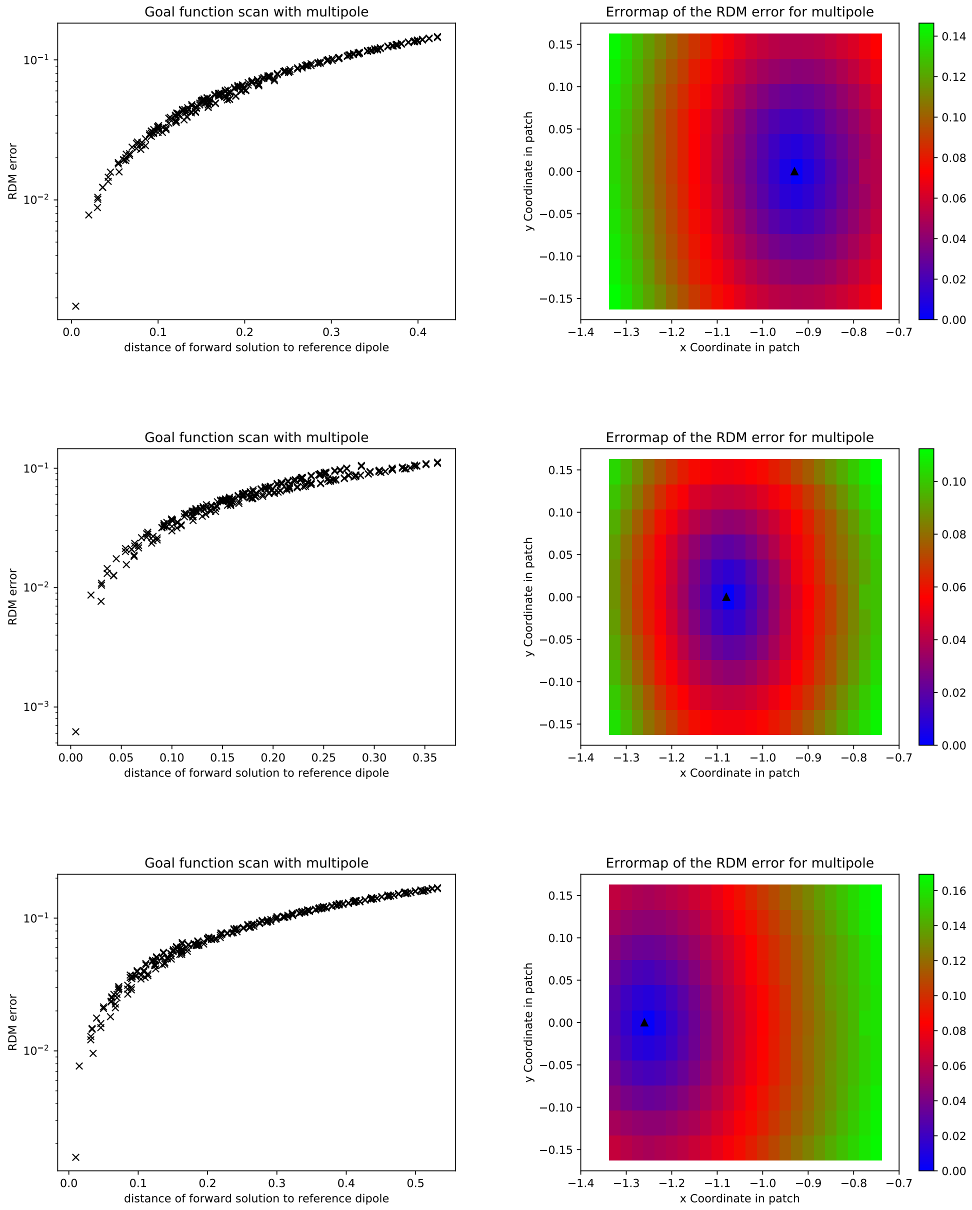

Figure 4.27: RDM errors between those 264 dipole locations and the real dipole for the *Multipole Approach*. We used the same dipole settings as in 4.11, 4.12 and 4.13.

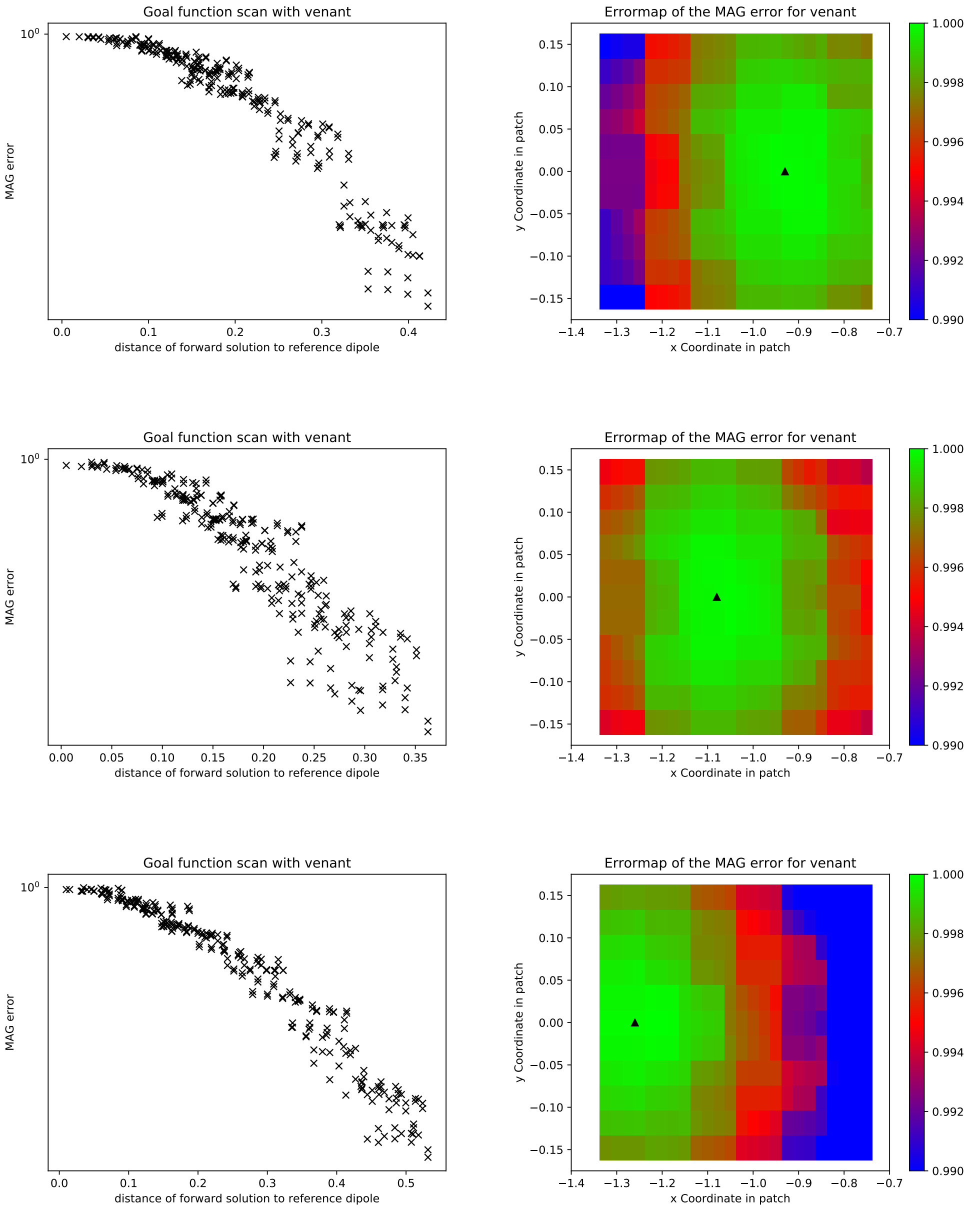

Figure 4.28: MAG errors between those 264 dipole locations and the real dipole for the *Venant Approach*. We used the same dipole settings as in 4.11, 4.12, and 4.13.

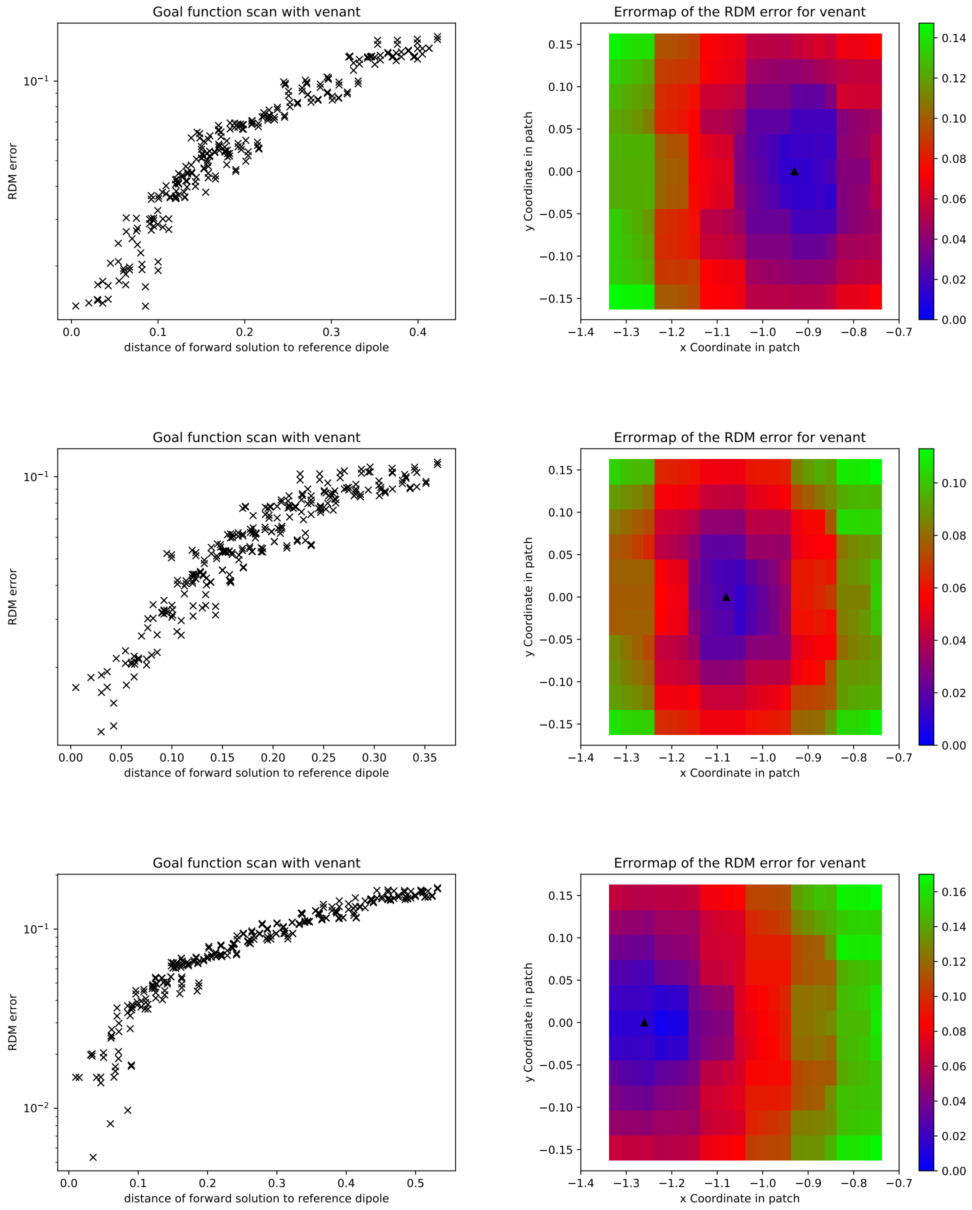
Goal function scan with venant

Errormap of the RDM error for venant

Goal function scan with venant

Errormap of the RDM error for venant

Goal function scan with venant

Errormap of the RDM error for venant

Figure 4.29: RDM errors between those 264 dipole locations and the real dipole for the *Venant Approach*. We used the same dipole settings as in 4.11, 4.12, and 4.13.

5 Summary

The aim of this dissertation was to expand the *Venant Approach* both theoretically and practically to use it for EEG/MEG forward computations. The approach substitutes the dipolar right–hand side with a distribution of monopoles. The monopoles are placed on the FE grid nodes adjacent to the dipole location. Monopole strengths are computed by solving a system of seven linear equations with added penalty conditions [18].

It is established that the *Venant Approach* is – so far – one of the best method for forward computations [44, 53]. Its use in inverse computations is successful as long as the source is located on FE nodes. If not, some forward solution artifacts impede the optimization process for dipole localization.

In this dissertation we proved the existence and uniqueness of a solution for such a substitution with the help of established theory about partial differential equations. The solution exists, if the monopole strengths equals zero, i.e. $0 = \sum_{i=1}^{m} q_i$ and the conductivity fulfills $\sigma \in C^2(B_i)$ for $B_i := B_{r_i}(x_i)$ such that $B_{r_i} \cap B_{r_j} = \emptyset$ for $i \neq j$. These conditions also apply to the *Partial Integration Approach* [79]. However, in contrast to the *Partial Integration Approach*, any approach based on the substitution of a dipole with a distribution of monopoles does have a solution within the function spaces $L^q(\Omega)$ for $1 \leq q \leq 2$, including $L^2(\Omega)$.

The motivation of the *Venant Approach* was described rather sparsely in the original paper [18]. We decided to derive this approach from the ground up. We used a *Multipole Expansion* to ensure that the potential of the electrical dipole and the potential of the monopole expansion are as similar as possible. This path led to our proposed method, the *Multipole Approach.* With this approach, the monopoles are placed upon the neighboring FE nodes, like with the *Venant Approach.* However, we now have ten conditions in contrast to the formerly seven to compute the monopole strengths, requiring us to solve a system of ten linear equations. Additionally, we also added penalty conditions.

This approach shares the first four conditions with the *Venant Approach*, but differs considerably in the remaining conditions.

For theoretical purposes, we derived an error estimator based on the difference of the computed potentials to an analytical solution.

We applied the new *Multipole Approach* in several numerical experiments. After some parameter optimization, this algorithm yielded favorable results for three different types of computations.

There are two parameters to optimize for the *Multipole Approach*: the weight of the penalty term λ, which is shared with the *Venant Approach*, and additionally, the number of locations for the placements of monopoles.

The first experiment involved computing the forward solutions on a 2D grid with uniform electric conductivity. On this grid we used the *Partial Integration Approach*, the *Venant Approach* and the *Multipole Approach* to compute electric field potentials. These potentials were compared to the interpolated analytical solution. We set up two different dipole locations, each with 47 different dipole moments. The results show a quadratic convergence rate for the *Multipole Approach*, whereas the *Partial Integration Approach* and the *Venant Approach* display linear convergence rates. Furthermore, the *Multipole Approach* seems to be less prone to artifacts than its competitors if the dipole is not located on a FE node.

The second experiment involved computing the forward solutions on 3D sphere models with four different conductivity layers. On these grids, we used the *Partial Integration Approach*, the *Venant Approach* and the *Multipole Approach* to compute electric field potentials. These potentials were compared to the De Munck sphere solution potential computed with fieldtrip [64]. We set up five different dipole locations, each with 47 different dipole moments. The results show that the *Multipole Approach* yielded a consistently higher level of accuracy than the *Partial Integration Approach* or the *Venant Approach.*

The third and final experiment involved computing goal function scans on the same model as before. We placed a 2D patch with 264 different dipole locations inside the model. We used the *Venant Approach* and *Multipole Approach* to compute the forward solution for each dipole with moments pointing along the three Cartesian directions. Then we computed the error to the De Munck sphere solution at each location with 20 reference dipoles. The results show that the *Multipole Approach* yielded a very smooth error surface, especially in comparison to the rough and artifact-ridden result from the *Venant Approach.* These experiments indicate that the *Multipole Approach* is highly suitable for use in inverse computations.

The computations so far have been rather sterile. Even a four-layer sphere model is only a rough model for a real human head. Therefore, the results of our numerical experiments can only be hints at the possible superiority of the *Multipole Approach* in a clinical setting.

Nonetheless, the *Multipole Approach* promises to be an interesting new option for source modeling in FEM based source analysis.

If the *Multipole Approach* fulfills its promises, it offers the possibility to improve localization of EEG measurements. It could directly be used on studies that were abandoned due to imprecise localization. It could also enable the examination of subtle activation patterns that were previously tainted by localization artifacts. With future implementations, our approach may also be used in more general settings that deal with localized electrical fields, such as material science or applied

chemistry.
Also, if a different source model is studied; for example if people want to study a quadrupole or a different load source [69]; the *Multipole Approach* can be easily adapted with a multipole expansion of the electric potential of the load source.
The *Multipole Approach* could make brain research a little easier and ultimately could help to understand and cure brain disorders.

6 Appendix A: programming the algorithm

The core function to compute the EEG forward problem with the *Multipole Approach* is a computation of the monopole locations and their strengths. The specific implementation for the location calculation depends on the software framework. However, if those locations are known, the algorithm for the strength calculation is always identical and can be roughly described as such:

1. compute the location of the 11–13 nearest FE nodes to the dipole location
2. for these monopole locations compute the Matrix $(V, W)^T$, where V is the matrix of 3.3.9 and W the matrix of 3.3.11
3. compute the right hand side $(\overrightarrow{t}, 0)^T$ with $\overrightarrow{t}$ described in 3.3.9
4. compute the solution $\overrightarrow{q}$ of the least square problem
$$\left\| \begin{pmatrix} V \\ W \end{pmatrix} \overrightarrow{q} - \begin{pmatrix} t \\ 0 \end{pmatrix} \right\|_2$$
5. use the computed solution $\overrightarrow{q}$ like
$$(J_h)_j = \left\{ \begin{array}{ll} q_j, & \text{if } x_j \in \{x_1, \dots, x_m\} \\ 0, & \text{else} \end{array} \right.$$
as discretization.

This leads to the algorithm described in pseudocode as follows:

Algorithm 1 Multipole

```
Given Moment $\overrightarrow{M}$ and location $x_0$ of dipole, The Finite Element Grid $(N, E, T, C)$.
procedure MULTIPOLE
    Compute at least 13 nearest neighbours $x_1, \dots, x_{13}$ of $x_0$ in $N$
    with $X$ compute matrix $V$ of equation 3.3.9
    with $X$ and $\lambda = 1e - 8$ compute Matrix $W$ of Gleichung 3.3.11
    with $\overrightarrow{M}$ compute vector $t$ of equation 3.3.9
    solve $\left\| \begin{pmatrix} \overrightarrow{t} \\ 0 \end{pmatrix} - \begin{pmatrix} V \\ W \end{pmatrix} \overrightarrow{q} \right\| \rightarrow min$
```

6.1 Implementation in UG4

The *Multipole Approach*, the *Venant Approach* and the *Partial Integration Approach* exist as prototypes within the UG4 framework in the plugin konnekfem [80, 68].

The C++ software library UG4 provides a fully-featured framework for Finite Element computations. In contrast to standard FE problems, our setting requires a preliminary step: the regularization of the EEG forward problem. This is an uncommon piece of functionality that needs to be implemented for each of the three approaches.

The segment that needed to be changed for this purpose was the discretization routine. We developed the classes *Blurred Disc* and *PIDisc* based on the class *IElementDisc*, along with some helper classes like the class *dipole*.

To ensure data encapsulation, UG4 provides a framework in the script language Lua [36], out of which only a certain set of functions can be called. We restrict ourself to describing those methods, which will be used for computing a forward solution. The technical realization within the classes is practically described before and not of interest for this documentation.

Before starting to use any approach, we first need to define a domain that the FE solution is computed on. This is accomplished by defining a tetrahedral grid as the discretized domain. For this purpose, we build sphere models in the UG4 format, which has the ending *.ugx*. In out case, the sphere models contain several subsets: one for each conductivity layer.

6.1.1 The class *dipole*

The class *dipole* consists of two *MathVector* instances: the vector *m_position*, which describes the position of the dipole, and the vector *m_moment* which describes the moment of the dipole. Both vectors are of the type *MathVector*, which is an internal UG4 class, and implements a mathematical vector.

Both vectors will be needed for the right hand side discretization.
Furthermore, there are several methods that control the dipole's position and moment. The method

```
settestdipole_different_moments(
        int i,
        const char* momentfile,
        int k,
        const char* positionfile)
```

is used if one wants to compute several forward computations with different dipoles in a loop.
The method is called with a momentfile and a positionfile, both of which are *.txt* files. Each line describes one position or moment of a dipole. The three coordinates of the position or moment are represented with floating–point numbers, separated by a space.
The method selects the ith moment in the momentfile and the kth position in the positionfile to define a dipole.

6.1.2 The class *Blurred_Disc* to compute the *Multipole* and the *Venant Approach*

The class *Blurred_Disc* can compute either the *Venant* or the *Multipole Approach.* The constructors in those classes are written so that there is no more need for additional configuration. There are several constructors implemented. The easiest setup is to call:

```
Blurred_Disc(
        const char* functions,
        const char* subsets,
        dipole <TDomain::dim> dip,
        Gridfunction<TDomain,TAlgebra>).
```

In this constructor, *functions* is a *char** that is required by the the base class *IElemDisc.* It needs to be set to " c " to function properly. *subsets* should be a *char** with the name of the subset in which the dipole is located. If there are several subsets possible, all can be listed but need to be in one *string* seperated by a ",".
dip is an instance of the helper class *dipole.*
The last parameter is the object representing the Finite Element vector of the right–hand side. Its type is *GridFunction.*

With this minimal configuration, *Blurred_Dipole* computes the Multipole right–hand side discretization for 13 monopole locations and a λ of $1e-8$ for the penalty term. This will automatically happen in the call of " assemble_linear" in the Lua code.
The method

```
set_neighbours(int number_of_neighbours)
```

determines how many monopole locations *number_of_neighbours* are used to represent the dipole. The selection starts with the FE node closest to the dipole, and continues in increasing geometrical distance.
Software libraries like simbio or fieldtrip use a different routine for the selection of the monopole locations. If this behavior is desired, calling the following method is recommended:

```
set_with_fieldtrip( int number_of_neighbours=1).
```

If no parameter is supplied, the default value is 1. In this case, the simbio monopole selection is used. This means that the monopole selection consists of two types of FE nodes: (1) the node closest to the dipole, and (2) all nodes directly connected to (1). If the supplied parameter *number_of_neighbours* is larger than 1, the algorithm will additionally use a third type of FE nodes: nodes of increasing geometrical distance to the dipole. The search radius for these nodes is increased until the specified number of nodes is reached.
Furthermore, the parameter *lambda* can be adjusted with the call:

```
set_lambda( double lambda).
```

If the Venant discretization is preferred the call

```
set_venant(bool)
```

is needed after initialization with the boolean value of true. With venant, the calls of *set_lambda* and *set_neighbours* are the same as for multipole. However, *set_with_fieldtrip* will always just use the SimBio/fieldtrip neighbor computations without adding any FE nodes up.

6.1.3 The class *PI_Disc* to compute Partial Integration

The *Partial Integration Approach* can be initialized with a call of

```
PI_Disc(
        const char* functions,
        const char* subsets,
        dipole <TDomain::dim> dip,
        Gridfunction<TDomain,TAlgebra>).
```

The supplied parameters are identical to the previous section in both naming and function.
Since the *Partial Integration Approach* does not require parameters, no additional methods are necessary.

6.1.4 Error computations with UG4

If forward computations are conducted with either the *Multipole Approach*, the *Venant Approach* or the *Partial Integration Approach*, the results are returned via an instance of GridFunction.
The errors at the sensor locations are not available immediately. To establish error levels, a class named *errors_to_fieldtrip* can be used. This class has an empty constructor.
A call to *read_sensors_from_file(sensortextfile)* from this class provides support for virtual sensors which are automatically used as targets for the following forward computations. The sensorfile is a text file. The first line denotes the total number of sensors. Each following line describes one sensor position: three separate floating–point numbers for X, Y, and Z coordinates, separated by a space. Unfortunately, computational restrictions require that only existing FE nodes can be used as sensor positions. To extract FE node positions from an .ugx head model, we wrote a convenient script in python.
When the instance of *errors_to_fieldtrip* is initiated and the sensors are set, the gridfunction of the forward solution needs to be read by calling *read_gridfunction(Gridfunctionname)*. The values of the *GridFunction* at the virtual sensors can then be written to a csv–file with a call of *write_gridfunction_to_csv(csvfilename)*
The next step is to compare the results to those of an analytical De Munck sphere solution, and to plot the differences.

6.2 Implementation in Fieldtrip

In Fieldtrip, the computations for the Venant approach was already implemented as described in [84] by default. Our only change consisted of a different weight computation to implement the *Multipole Approach*.
For this purpose, we wrote two new routines:

(1) *sb_rhs_multipole*, and the sub function (2) *sb_calc_multipole_loads*. Those modified files will hopefully included into fieldtrip in the future. If the multipole approach is desired over the *Venant Approach*, the function name *sb_rhs_venant* can be changed to *sb_rhs_multipole* whenever it is called in an existing fieldtrip script.
Note that fieldtrip may not always allow using 11–13 monopole locations.

7 Appendix B: *Adaptive Finite Element Methods* and the *Multipole Approach*

We have developed an improvement of the old *Venant Approach* making it possible for FE Methods to be used for the EEG forward problem.
However, FE also has some drawbacks. The rule of the thumb is that the approximation (and the error) improves for a finer resolution of the grid. Since finer grids need longer computational time, we have to find a sufficient grid with has a good balance between resolution and accuracy.
The key question to find such a grid is thus: How finely resolved does the grid need to be?
An answer to this question could be the so–called *Adaptive Finite Element Methods*, which start on a coarse grid and use an estimation to the accuracy to refine the grid only where it is necessary.
As explained in chapter 2.1, we consider the weak solution formulation of the model problem 3, which was

Problem 7. *Let Ω_l be a discretization of the domain Ω. Find $u \in$ a finite element space $V(\Omega_l)$, such that*

$$\int_{\Omega} \sigma \nabla u \nabla v dx = \int_{\Omega_l} f v dx \textit{ for any } v \in V.$$

Now we do not want to create Ω_{l+1} out of Ω_l with refining all elements (hexahedra or tetrahedra). We just want to refine those elements where the accuracy would improve the most.
Thus, to employ adaptive FE Methods on this problem, we need an error estimator. It reveals a cell wise estimation for the error of a solution $u_l \in V(\Omega_l)$. We also need a marking strategy to decide, which elements will be refined, and a refinement strategy to compute a Ω_{l+1} out of Ω_l.
The algorithm is very straight forward from that point on.
First, we solve the problem and compute a solution $u_l \in V(\Omega_l)$. Second, for every cell $T \in \Omega_l$ we will compute an error estimator using the solution u_l.
We are either interested on the error in the L_2–norm with $\|u - u_h\|_{L_2(\Omega)}$ or the energy–norm $\|u - u_h\|_{\sigma,\Omega} := \sqrt{a(u - u_h, u - u_h)}$, where a is the continuous bilinear form (2.1.4) coming from the problem 4.

Third, when all the estimators for each cells and, thus, also the estimator for the whole solution are computed, we can decide on which element to refine. The fourth and final step is to perform the grid refinement.
There is a particular error estimator for the energy error, which was first described by Babuška and Rheinbold in 1967 ([7]):
Let $T \in \Omega_l$, then the error estimator is given by

$$\mathcal{E}^2(u_h, T) := h_T^2 \|r(u_h)\|^2_{L^2(T)} + h_T \|j(u_h)\|^2_{L^2(\partial T \setminus \partial\Omega)}, \tag{7.0.1}$$

where the interior and the jump residuals are defined by

$$\begin{aligned} r(u_h) &= f + \operatorname{div}(\sigma \nabla u_h) \\ j(u_h) &= [\sigma \nabla u_h]_S, \end{aligned}$$

with $[]_S$ symblizes the jump on the edge S. To compute the whole error for the whole solution u_l, we summarize over all cells

$$\mathcal{E}^2(u_h, \Omega_l) := \sum_{T \in \Omega_l} \mathcal{E}^2(u_h, T).$$

The first proven property of this error estimator is its efficiency and reliability, which are important in the context of AFEM as this bounds the accuracy from above and below.

Theorem 5. *([7]) The error estimator 7.0.1 is efficient and reliable with an upper and a lower bound.*
There exist $C_1, C_2 \in \mathbb{R}$ such that

$$\begin{aligned} \|u - u_h\|^2_{\alpha,\Omega} &\leq C_1 \mathcal{E}^2(u_h, T) \\ C_2 \mathcal{E}^2(u_h, T) &\leq \|u - u_h\|^2_{\alpha,\Omega} + osc^2_{\mathcal{T}}(u) \end{aligned}$$

with the element oscillation

$$osc_{\mathcal{T}}(v, T) = \|h(r(v) - P_{2n-2} r(v))\|_{L^2(T)} + \|h^{1/2} h(j(v) - P_{2n-1} j(v))\|_{L^2(T)}$$

(and P_i means the polynomial L^2–Projections).

It was possible to prove that the error estimator will give convergence [56]. However, the most important aspect – whether the estimator showed an improved performance in relation to the number of elements (quasi-optimality) – was still an open question at this point.
Quasi-optimality for the 2D case was proven by Binev, Dahmen, DeVore [11]. The proof for the n dimensional case (for $n \in \mathbb{N}$) followed in 2007 by Stevenson [76].

It is important to note, that this quasi–optimality is reaches using *Dörfler Marking* [24] for the marking strategy and *bisection* as refinement stategy.
In summary, a AFEM can be described by four modules:
SOLVE: compute a forward solution of 3
ESTIMATE: compute the error estimator (7.0.1)
MARK: use *Dörfler Marking* selecting elements that exceed a predefined threshold of relative local error [24]
REFINE: refine the selected elements through bisection.
We refer to [61, 60] for a deeper understanding to the AFEM.
If we want to apply AFEM to our case, we require regularization since the error estimator fails to work with a mathematical dipole.

There are some cases in which the refinement goal is neither the L_2 nor the energy norm. Instead, the error is minimized with regard to a functional. This strategy is called *Goal–Oriented Adaptive Finite Element Methods* [9, 55].
In addition to the standard AFEM approach, the adjoint problem – provided by the functional – is also computed in this case. For this adjoint problem we have the same prerequisites as for the original problem. Thus, a standard AFEM can be computed on the adjoint problem.
For a goal–oriented AFEM, both approaches are mixed. Error estimators are computed for both the original and the adjoint problems. After comparing the optimization results from each approach, the more favorable refinement method can be chosen at every step [55].
An AFEM will typically equi–distribute the error estimation over the whole domain. However, we are unable to measure the electric potential throughout the entire head. Instead, we are limited to sensor positions on the head surface. For this reason it would be ideal to minimize the error for exactly these positions. We can understand this goal as employing a functional.
The quantity of interest for the EEG forward problem is the functional

$$F_{adjoint} = \sum_{x \in X_{sens}} \delta_x,$$

with X_{sens} defined by 2.0.1.
This will give us the adjoint problem

Problem 8. *Find* $u \in \{v \in H^{-1}(\Omega) | \int_\Omega \eta v dx = 0\}$*, such that*

$$\int_\Omega \sigma \nabla u \nabla v dx = \sum_{x \in X_{sens}} \delta_x v \textit{ for any } v \in V.$$

n the following section, we will adapt the Standard AFEM, a GoAFEM and other adaptive approaches to our problem and review them numerically.

7.1 Adaptive Experiments

So far we only have considered standard FE theory for the EEG forward problem. When attempting to apply an adaptive strategy to this theory, we have to overcome certain problems.
Even if FE computations are applicable, the new right–hand side $J_{\text{monopoles}}$ of 3.0.1 is still not in $L_2(\Omega)$. The error estimator computes the L_2–Norm on all elements of the discretized domain. This can not be done with $J_{\text{monopoles}}$.

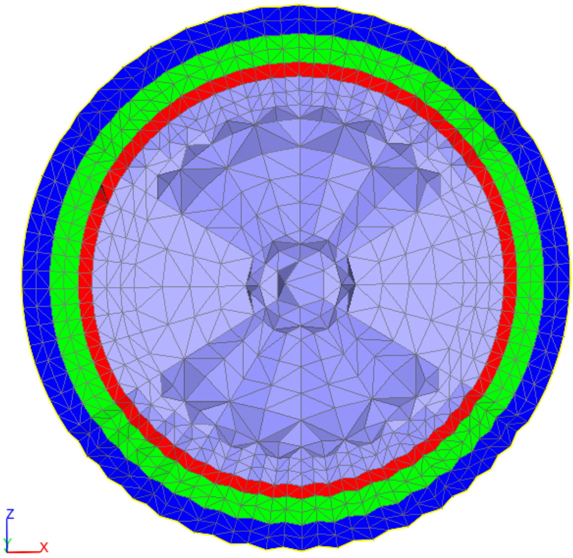

Figure 7.1: Slices of the four–layer 3D sphere model with 20398 FE nodes, which was used for adaptive computations.

Instead of concentrating on theory, we choose a rather heuristic approach to use AFEM in numerical experiments with the *Multipole Approach*, as this will show us the usage in practice.
We choose the 3D sphere model grid of chapter 4 (with 20398 FE nodes) as the base grid.
We try five different kinds of heuristics:

1. global refinement on one grid
2. normal adaptive procedure with a modified error estimator after Babuška
3. adjoint adaptive computations

4. goal–oriented computations
5. standard adaptive procedure with a modified right–hand side (e.g. [61, 60])

In every experiment, we place the dipole at the grid coordinates $(-1.0, 0.0, 0.0)$ and compute the forward solutions for 50 different dipole moments, similar to the 3D sphere model forward computations in chapter 4. In contrast to the six different grids in that model, we now use only one grid that gets refined adaptive.

We apply the adaptive strategy of choice up to five times, or until we reach a number of 600000 Finite Element nodes.

We compare the accuracy of these numerical experiments with the results of the sphere model from Chapter 4, and use violin plots for comparison.

For a more convenient visualization, we summarize the accuracy of the 50 forward computations on the grids with 20398, 58488 and 421124 from Chapter 4 as a grey block with upper and lower limit in black and the median indicated with a grey line. We henceforth call those three grids (4A), (4B) and (4C).

If the adaptive scheme would be better than the 3D forward computations on the sphere models of chapter 4, the accuracy values would lie in the lower part of the gray area or even below.

The accuracy of the adaptive numerical experiments is pictured with violin plots, where we enclosed values into one violin if the number of nodes was sufficient close enough.

For the global refinement as well as the adjoint refinement and the adaptive computation on the substitution of the right–hand side, the refinement is independent of the exact moment and thus, the algorithm decides to refine the same cells for every of the 50 moments.

For the normal adaptive and the goal–oriented procedure this is not the case. Here a different number of cells is refined in the same step for different moments. However, the number of cells is in a certain range. Therefore, to produce good images, we decide to do a k-means clustering beforehand and cluster for the normal adaptive procedure into seven clusters. We decided the number of clusters by looking at a scatter plot.

However, using the AFEM with the *Multipole Appoach* in a practical setting comes with technical limitations.

Firstly, the adaptive refinement procedure in ug4 only supports the refinement of hanging nodes. The standard AFEM, on the other hand, uses refinement by bisection or completion and will not produce hanging nodes [61, 60].

Secondly, the choice is limited by the working memory and processing speed of the computing platform. For this reason, we focus our efforts on smaller models and stop refining when 600.000 nodes are reached.

Despite these limitations, the numerical computations are valuable to compare different approaches of adaptivity to each other.

7.1.1 Global refinement

In chapter 4, we approximated a refinement strategy by using several sphere models. Now we are refining one grid globally to be able to understand how global refinement affects the error propagation.

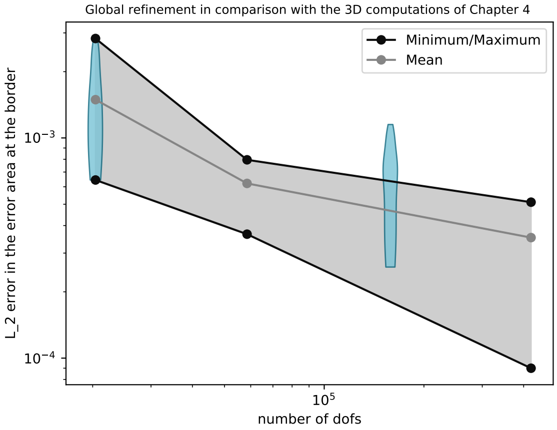

Figure 7.2: Accuracy of global refinement pictured with two blue violin plots.

Global refinement yields two grids: the base grid (A) with 20398 FE nodes, and the grid with 158494 FE nodes (B) after one refinement. A second refinement would exceed our node limit of 600000 FE nodes and is skipped for that reason.

We observe that the accuracy for grid (B) is overall slightly smaller than for grid (A). However, both result patterns show considerable overlap. Furthermore, the numerical computations of chapter 4 on grid (4B) are slightly more accurate than on grid (B).

Thus, we see that global refinement does have an impact on accuracy, but not in the desired direction.

7.1.2 Standard AFEM

As mentioned before, we can not apply the error estimator 7.0.1 to elements that contain monopoles. Therefore, we define a small exclusion radius around the monopole locations of $1e-5$. Elements within this radius are refined at every step, but are excluded from the global error estimation.

As apparent from the results, there is no real error reduction using the standard AFEM. Results are mostly planar, independent of the number of refinements with

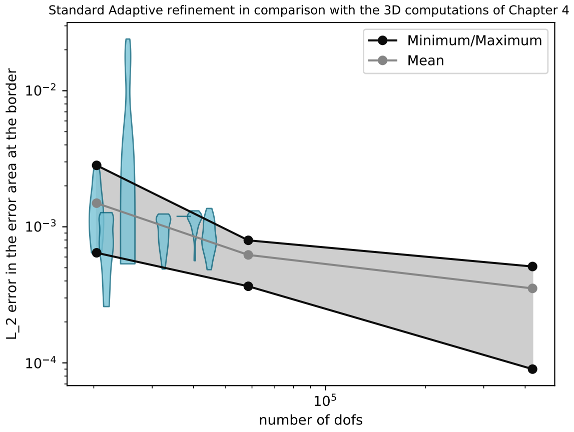

Figure 7.3: Accuracy of normal adaptive procedure pictured with blue violin plots.

some outliers in both directions. As a result, most of the error spectrum overlaps with the results from chapter 4 (signified by the grey area).

When we visualize the refinement of the grid, we can see the reason for this kind of behavior.

As we already predicted during the error estimation in Chapter 3.4, the error is the biggest around the dipole location and decreases towards the boundary of the domain (with uniform conductivity). Since we have constant conductivity within this layer, the error estimator shows the largest values right around the dipole location. Thus, as expected, most of the refinement occurs in the vicinity of the monopole locations.

However, this will have no effect on the overall error. We are not actually interested in minimizing the overall error, but rather only at the sensor locations.

7.1.3 Goal–oriented AFEM

Goal–oriented Finite Element methods aim to compute adaptive with regard to a functional.

As functional of interest we already identified

$$F_{adjoint} = \sum_{x \in X_{sens}} \delta_x,$$

with X_{sens} defined by 2.0.1.

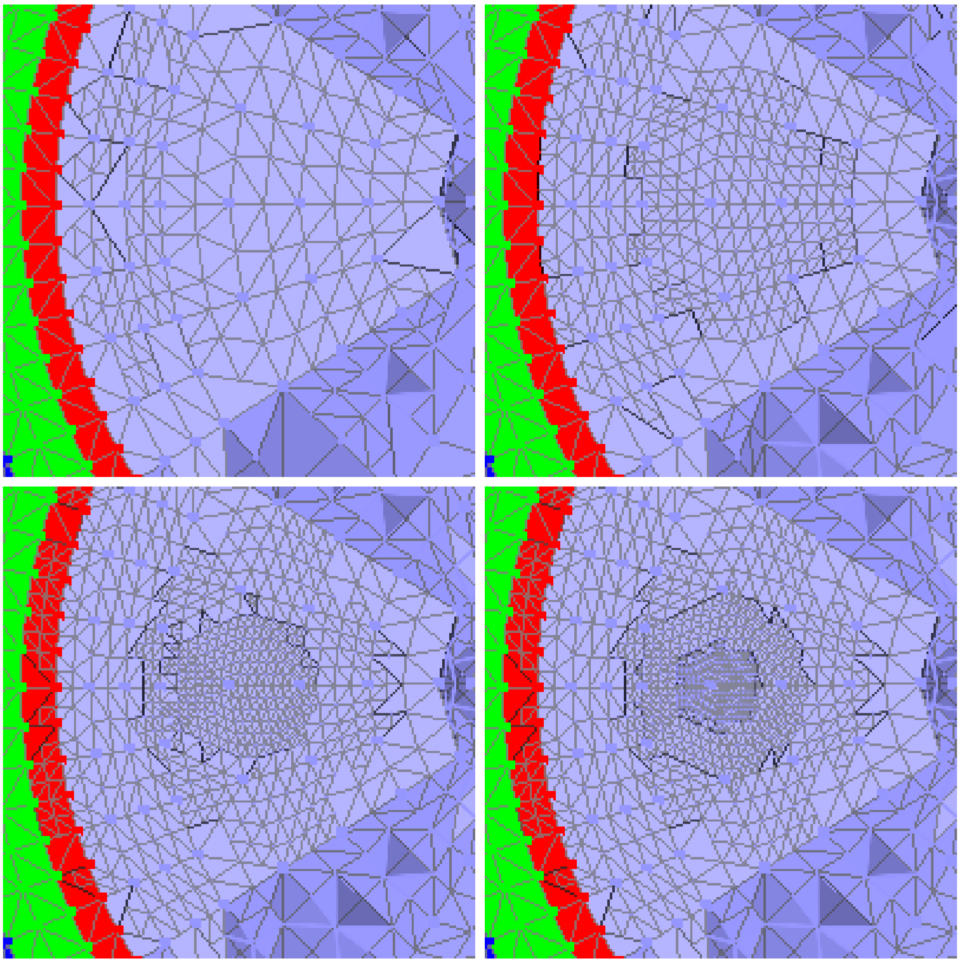

Figure 7.4: Normal adaptive procedure on the grid in four steps. The dipole was placed at $(-1.0, 0.0, 0.0)$.

X_{sens} is a discrete set, therefore, we again have a finite sum over dirac delta distributions.

The GOAFEM practically computes two adaptive schemes: one for the original problem and one for the adjoint problem.

Therefore, we first take a look into the adjoint problem and into its behavior in an adaptive context.

7.1.3.1 Adjoint AFEM

The adjoint problem substitutes the right-hand side of the PDE with the functional:

Problem 9. *Find* $u \in \{v \in H^{-1}(\Omega) | \int_\Omega \eta v dx = 0\}$*, such that*

$$\int_\Omega \sigma \nabla u \nabla v dx = \sum_{x \in X_{sens}} \delta_x v \textit{ for any } v \in V.$$

The right-hand side is thus, again, not in L_2 and we helped ourselves with a small fix.
Firstly, we assume that every sensor is placed on a FE node in the grid.
Secondly, we have to consider the compatibility condition for *Neumann* problems, which requires that the integral over the right-hand side needs to be zero.
Therefore, we weigh every summand of the functional with 1 and -1 in alternation. The last sensor is assigned a value such that$\sum_{x \in X_{sens}} f(x) = 0$.

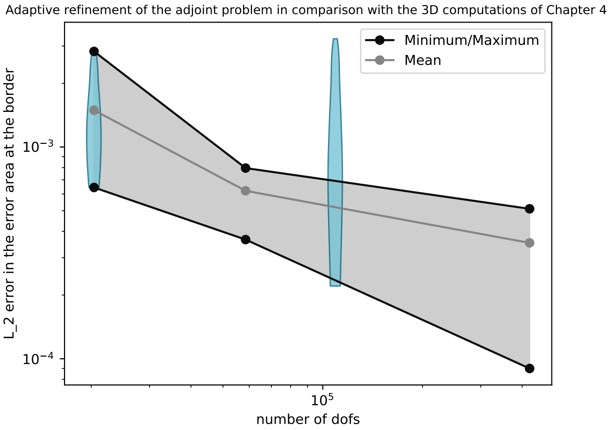

Figure 7.5: Accuracy of adjoint adaptive procedure pictured with two blue violin plots.

The adaptive scheme on the adjoint problem will not lead to big enhancements in accuracy. When actually computing it, side effects cause the error distribution to be spread out beyond the results from chapter 4 (i.e., grey box).
This problem becomes more obvious when we again visualize the grid refinement: it mostly takes place in the vicinity of the sensor locations.
Since those are located directly on the surface, the deviations between a perfect sphere and the actual model are causing a larger model error.
The shape of a practical spherical model for use in FE will always deviate from a perfect sphere because FE methods require a discretization. Thus we have to use tetrahedra with a boundary that approximates a spherical surface.

More tetrahedra could be used to have a finer approximation – however this also would require more tetrahedra inside of the model and this contradicts the idea to start on a coarse grid with AFEM.

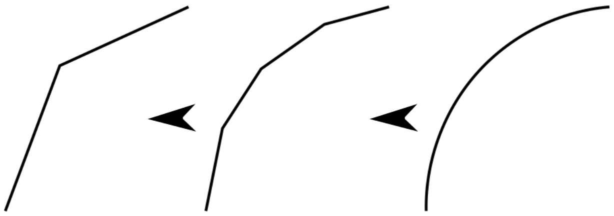

Figure 7.6: A sketch of how a slice of the surface can approximate the surface of a sphere. Every line stands for the edge of one tetrahedra.

Therefore, we can not improve the error levels substantially by using this scheme.

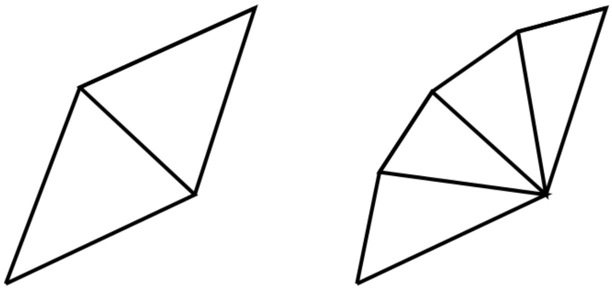

Figure 7.7: When we approximate the border smoother and choose the same refinement points in the rest of the sphere as FE nodes, the tetrahedra will get pointier and the grid will not be as regular as before, which is not desirable for FEM.

7.1.3.2 Goal–oriented computations

When we use the goal-oriented adaptive FEM as described in [55], we always encounter one problem: When the algorithm compares error estimators to select either the standard error estimator or the adjoint variant for refinement, it always picks the standard refinement. This happens because the standard error estimator always implies a bigger gain from refinement.
This issue leads to results as shown in figure 7.3.
To address this problem, we decided to implement a small adjustment: we refine in alteration between standard and adjoint error estimators, starting with an adjoint

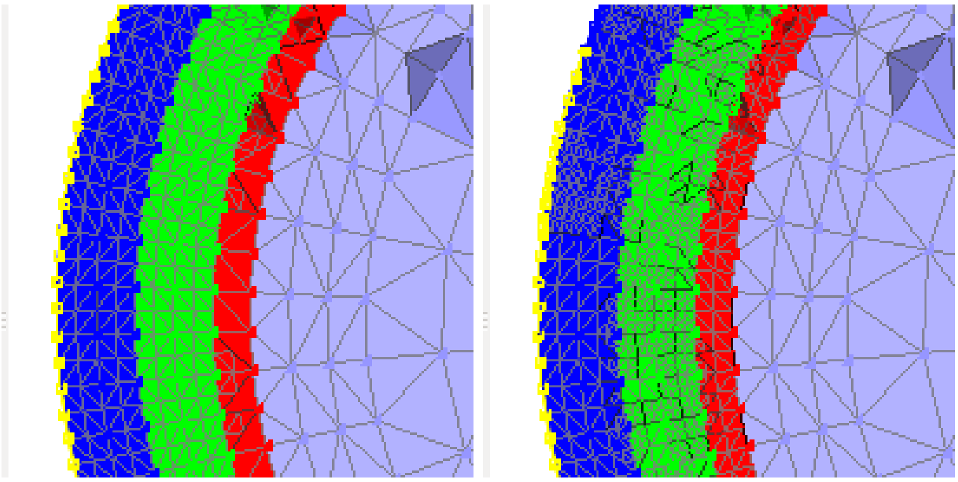

Figure 7.8: Adjoint procedure on the grid in four steps. The dipole was placed at $(-1.0, 0.0, 0.0)$.

step.

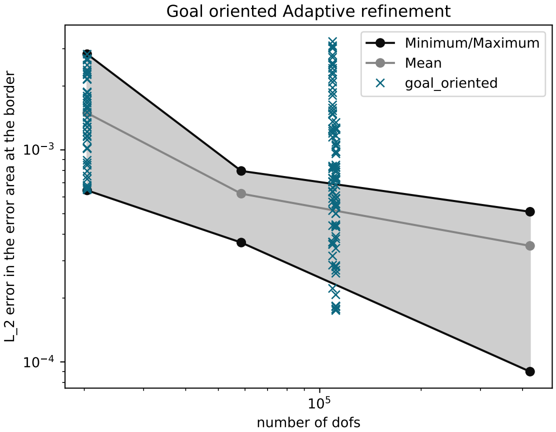

Figure 7.9: Accuracy of the goal–oriented adaptive procedure with adjoint and standard AFEM in alteration pictured with blue scattered x.

For the results from this scheme, we use a scattered plot instead of a violin plot because the adaptive refinement will lead to approximately the same number of FE nodes. But we can still see horizontal clusters with the naked eye but cannot determine, the number of distinct clusters.

Most of the computed solutions reach an accuracy not better than on the grids (4A)-(4C) and fit into the grey area or above.

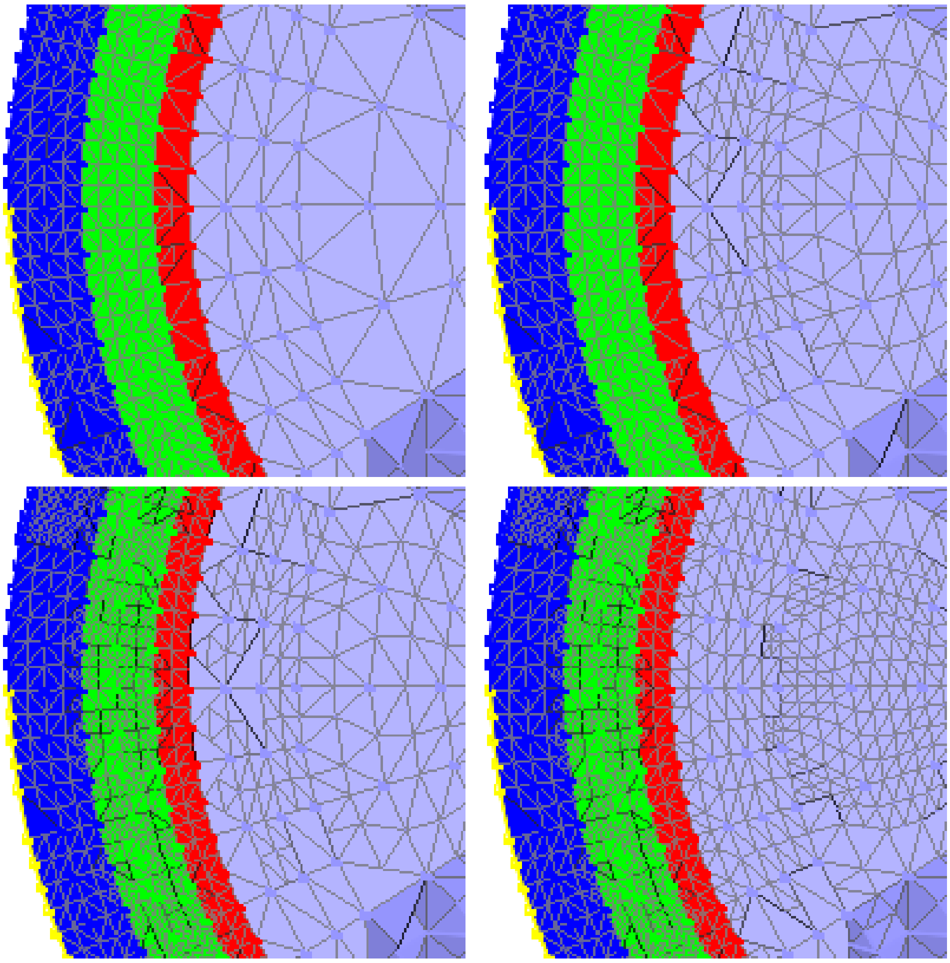

Figure 7.10: goal oriented adaptive procedure on the grid in four steps. The dipole was placed at $(-1.0, 0.0, 0.0)$.

When we look at how those refinements are done, we can see that the refinements are a mix by the refinements of standard adaptive and adjoint adaptive scheme.

Thus, we do not get any improvement over the standard adaptive and adjoint adaptive refinement.

7.1.4 Computing with a new right–hand side

All previous adaptive computations did not reach improvements in accuracy. Therefore, we want to try something else.

Instead of computing the AFEM for the EEG forward problem we might want to concentrate on the grid. We acknowledge that the interesting part happens in the compartment of the brain, which we will call $\Omega_{\mathrm{b}} \subset \Omega$.

We define a new right–hand side as

$$J_{\text{adaptive}}(x) = \begin{cases} 1, \text{if } x \in \Omega_{\mathrm{b}} \\ 0, \text{else} \end{cases} . \tag{7.1.1}$$

This right–hand side is in $L_2(\Omega)$. Then we apply the AFEM with the error estimator according Babušca [7]. We then compute the accuracy of the *Multipole Approach* on this grid.

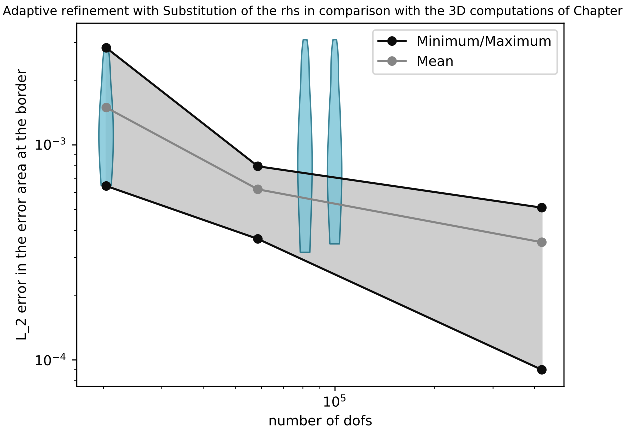

Figure 7.11: Accuracy of the AFEM used on the substituted right–hand side pictured with three blue violin plots.

This scheme does not lead to better results. In fact, we will get two additional violin plots independently of the moment. The violin plots are just horizontal to the right from the first one and have a slightly higher amplitude.

We cannot see any meaningful change in terms of accuracy - neither in a positive nor a negative direction.

We visualize the refinement again. With a substituted right–hand side, the algorithm decides to refine within the conductivity jumps. So between the middle of

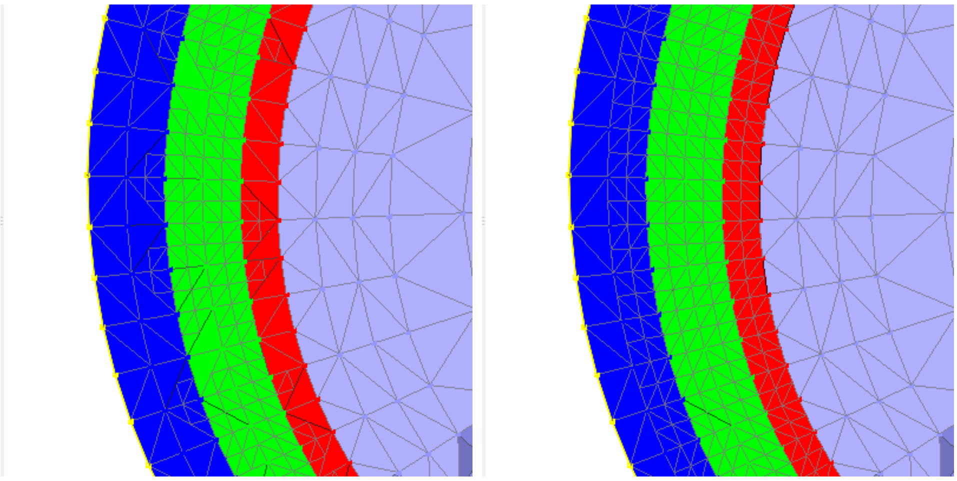

Figure 7.12: refinement of AFEM with a substituted right–hand side. The dipole was placed at $(-1.0, 0.0, 0.0)$.

the tissue compartment to the lower border of the CSF compartment all cells will be refined. However, the inner part of the sphere is not refined. The boundary is not refined either.

7.1.5 Conclusion of the numerical experiments for the adaptive FE methods

When applying the proposed adaptive schemes, we encountered several problems:

1. Model errors due to necessary approximation of the domain boundary
2. Model errors due to necessary approximation of conductivity jumps
3. Error Estimation for the dipolar right–hand side in the EEG forward problem is not possible
4. Error Estimation for the monopolar right–hand side in the adjoint problem is not possible
5. Unfinished adaptive procedures in UG4

Each of the tested schemes encounter one or more of this limitations.
However, the grids we designed for the 3D computations work well. and accuracy convergence with these is faster than with global refinement.
Therefore, we can use the generation of those grids as a guideline for the creation of grids to compute the EEG forward problem in general.

When generating the sphere models we control the number of tetrahedra within ProMesh [67]. In the first step, we define an approximation of sphere surfaces consisting of a certain number of triangles. In the second step we nest those sphere surfaces. For the outer shells we use finer resolutions than for the inner ones. In the third and final step, we use the help of a triangulation algorithm called TetGen [73] to generate a 3D model. We use more sphere surfaces than the number of compartments to ensure a good triangulation. However, each compartment boundary is also one of the nested surfaces.

To get sphere models with a better resolution and more finite element nodes, we progressively increase the resolution of surfaces from the outside towards the center. Additionally, for the finer models we subdivided the model into even more sphere surfaces 4.6.

With this generation process, we obtain sphere models which have relatively regular tetrahedra. The exact positions of the FE nodes of each coarse model are preserved in the finer models.

From this and the results of the numerical experiments, we conclude the following steps for constructing good grids for the EEG forward problems:

- ensure that the grid surface is sufficiently smooth and approximates the original surface very well
- ensure that the conductivity jumps are of a sufficient resolution
- ensure that you have sufficiently regular cell elements

However, the experiments so far gave no indications as to what “sufficiently” means in this context.

Bibliography

[1] R.A. Adams. *Sobolev Spaces.* Academic Press, New York, u.a., 1975.

[2] R.A. Adams and J. Fournier. "Cone Conditions and Properties of Sobolev Spaces". In: *J. o. Math. Anal. a. Appl.* 61 (1977), pp. 713–734.

[3] H.W. Alt. *Lineare Funktionalanalysis.* 5. überarb. Springer, Berlin [u.a.], 2006.

[4] K. Amunts, G. Schlaug, A. Schleicher, H. Steinmetz, A. Dabringhaus, P. Roland, and K. Zilles. "Asymmetry in the Human Motor Cortex and Handedness". In: *NeuroImage* 4 (1996), pp. 216–222. DOI: `10.1006/nimg.1996.0073`.

[5] R. Anandakrishnan, C. Baker, S. Izadi, and A. Onufriev. "Point Charges Optimally Placed to Represent the Multipole Expansion of Charge Distributions". In: *PLOS one* 8 (2013). DOI: `10.1371/journal.pone.0067715`.

[6] E. Anderson, Z. Bai, C. Bischof, S. Blackford, J. Demmel, J. Dongarra, J. Du Croz, A. Greenbaum, S. Hammarling, A. McKenney, and D. Sorensen. *LAPACK Users' Guide.* Third Edition. Philadelphia, PA: Society for Industrial and Applied Mathematics, 1999.

[7] I. Babuška and W. Rheinbold. "Error Estimates for adaptive finite elements computations". In: *SIAM J. Numer. Anal* 15 (1978), pp. 736–754.

[8] W. Bechtel. *Mental Mechanisms: Philosophical Perspectives on Cognitive Neuroscience.* Taylor & Francis Group, 2008.

[9] R. Becker and R. Rannacher. "an optimal control approach to aposterori error estimation in finife element methods". In: *Acta Numerica* (2001), pp. 1–102.

[10] J. Bermúdez. *Cognitive Science: An Introduction to the Science of the Mind.* Cambridge University Press, 2014.

[11] P. Binev, W. Dahmen, and R. DeVore. "Adaptive finite element methods with convergence rates". In: *Numer. Math.* 97 (2004), pp. 219–268.

[12] D. Braess. *Finite Elemente: Theorie, Schnelle L Ser Und Anwendungen in Der Elastizit Tstheorie (Springer-Lehrbuch) (German Edition).* Springer, 1992.

[13] D. Braess. *Finite Elements: Theory, Fast Solvers, and Applications in Solid Mechanics.* Cambridge University Press, 2007.

[14] S. Brenner and R. Scott. *The mathematical Theroy of Finite Element Methods.* Text in Applied Mathematics, Vol. 15. New York: Springer, 2008.

[15] R. Brette and A. Destexhe, eds. *Handbook of Neural Activity Measurement.* Cambridge University Press, 2012.

[16] K. Brodmann. *Vergleichende Lokalisationslehre der Grosshirnrinde. In ihren Principien dargestellt auf Grund des Zellenbaues.* Johann Ambrosius Barth Verlag Leipzig, 1909.

[17] K. Brodmann. [Public Domain] via Wikimedia Commons. Source: [16]. 2017.

[18] H. Buchner, G. Knoll, M. Fuchs, A. Rienäcker, R. Beckmann, M. Wagner, J. Silny, and J. Pesch. "Inverse localization of electric dipole current sources in finite element models of the human head". In: *Electroencephalography and clinical Neurophysiology* 102 (1997), pp. 267–278.

[19] J. -. H. Cho, J. Vorwerk, C. H. Wolters, and T. R. Knösche. "Influence of the head model on EEG and MEG source connectivity analyses". In: *NeuroImage* 110 (2015). DOI: `10.1016/j.neuroimage.2015.01.043`.

[20] P.G. Ciarlet. *The finite element method for elliptic problems.* Studies in Mathematics and its Applications, Vol. 4. Amsterdam: North-Holland, 1978, pp. xix+530.

[21] W. Dahmen and A. Reusken. *Numerik für Ingenieure und Naturwissenschaftler (Springer-Lehrbuch) (German Edition).* Springer, 2008.

[22] M. Dannhauer, B. Lanfer, C.H. Wolters, and T.R. Knösche. "Modeling of the Human Skull in EEG Source Analysis". In: *Human Brain Mapping* 32.9 (2011). DOI: 10.1002/hbm.21114, PMID: 20690140, pp. 1383–1399.

[23] Dhp1080, svg adaptation by Actam, and modified by A. Hanrath. *Derived Neuron schema with no labels, Licensed under CC-BY-SA 3.0.* Wikimedia Commons.

[24] W. Dörfler. "A convergent adaptive algorithm for Poisson's equation". In: *SIAM Journal on Numerical Analysis* 33.3 (1996), pp. 1106–1124.

[25] D. Draaisma. *Disturbances of the Mind.* Cambridge University Press, 2009.

[26] F. Drechsler, Wolters C.H., T. Dierkes, T. Si, and L. Grasedyck. "A full subtraction approach for finite element method based source analysis using constrained Delaunay tetrahedralisation". In: *Neuroimage* 46 (2009), pp. 1055–1065.

[27] A. Ern and J.-L. Guermond. *Theory and Practice of Finite Elements.* Springer Science & Business Media Berlin, 2013.

[28] L. Evans. *Partial differential equations.* Graduate studies in mathematics. American Mathematical Society, Providence, 1998.

[29] H. Gardner. *The Mind's New Science: A History of the Cognitive Revolution.* Basic Books, 1987.

[30] S. Gauggel and M. Herrmann. *Handbuch der Psychologie: Handbuch der Neuro- und Biopsychologie: BD 8*. Hogrefe-Verlag, 2008.

[31] D. Griffiths. *Introduction to electrodynamics*. 3rd. Addison Wesley, 1999.

[32] SimBio Development Group. *SimBio - A Finite element toolbox for Calculation of EEG/MEG Forward and Inverse Problems*. online, https://www.mrt.uni-jena.de/simbio, accessed Aug 15. 2019.

[33] M. Hämäläinen, R. Hari, R. Ilmoniemi, J. Knuutila, and O. Lounasmaa. "Magnetoencephalography - theory, instrumentation, and applications to non-invasive studies of the working human brain". In: *Rev. Mod. Phys.* 65 (1993), pp. 413–497.

[34] M. Hämäläinen and R. Ilmoniemi. "Interpreting magnetic fields of the brain: minimum norm estimates". In: *Medical & Biological Engineering & Computing* 32.1 (1994), pp. 35–42. DOI: `10.1007/BF02512476`.

[35] J. Hunter. "Matplotlib: A 2D graphics environment". In: *Computing In Science & Engineering* 9.3 (2007), pp. 90–95.

[36] R. Ierusalimschy, L. de Figueiredo, and W. Celes. "Lua – an extensible extension language". In: *Software: Practice & Experience* 26.6 (1996), pp. 635–652.

[37] S. Izadi. "Optimal Point Charge Approximation: from 3-Atom Water Molecule to Million-Atom Chromatin Fiber". PhD thesis. Virginia Polytechnic Institute and State University, 2016.

[38] T. Knösche. *Solutions of the neuroelectromagnetic inverse problem: An evaluation Study, PhD Thesis*. Netherlands : University of Twente, 1996.

[39] H. Köstler. "Akkurate Behandlung von Singularitäten bei partiellen Differentialgleichungen". Diploma Thesis. Lehrtuhl für Informatik 10, Friedrich–Alexander–Universität Erlangen–Nürnberg, 2003.

[40] J. Kybic, M. Clerc, T. Abboud, O. Faugeras, R. Keriven, and T. Papadopoulo. "A common formalism for the integral formulations of the forward EEG problem". In: *IEEE Trans. Med. Imag.* 24.1 (2005), pp. 12–18.

[41] J. Kybic, M. Clerc, O. Faugeras, R. Keriven, and T. Papadopoulo. "Generalized head models for MEG/EEG: boundary element method beyond nested volumes". In: *Phys. Med. Biol.* 51 (2006), pp. 1333–1346. DOI: `doi:10.1088/0031-9155/51/5/021`.

[42] W-Ch. Lee, H. Huang, G. Feng, J. Sanes, E. Brown, P. So, and E. Nedivi. Wikimedia Commons CC BY 2.5. Source: Dynamic Remodeling of Dendritic Arbors in GABAergic Interneurons of Adult Visual Cortex. Lee WCA, Huang H, Feng G, Sanes JR, Brown EN, et al. PLoS Biology Vol. 4, No. 2, e29. doi:10.1371/journal.pbio.0040029, Figure 6f, slightly altered (plus scalebar, minus letter "f".) 2017.

[43] S. Lew, D. Sliva, M.-S. Choe, P. Grant, Y. Okada, C. Wolters, and M. Hämäläinen. "Effects of sutures and fontanels on MEG and EEG source analysis in a realistic infant head model". In: *NeuroImage* 76 (2013), pp. 282–293. DOI: `10.1016/j.neuroimage.2013.03.017`.

[44] S. Lew, C.H. Wolters, T. Dierkes, C. Röer, and R.S MacLeod. "Accuracy and run–time comparison for different potential approaches and iterative solvers in finite element method based EEG source analysis". In: *Appl. Numer. Math.* 59.8 (2009). http://dx.doi.org/10.1016/j.apnum.2009.02.006, NIHMSID 120338, PMCID: PMC2791331, pp. 1970–1988.

[45] A. Louis. *Inverse und schlecht gestellte Probleme.* B.G. Teubner Stuttgart, 1989.

[46] A. Love. *A Treatise on the Mathematical Theory of Elasticity (Dover Books on Engineering).* Dover Publications, 2011.

[47] F. Lucka, S. Pursiainen, M. Burger, and C. Wolters. "Hierarchical Bayesian Inference for the EEG Inverse Problem using Realistic FE Head Models: Depth Localization and Source Separation for Focal Primary Currents". In: *NeuroImage* 61(4) (2012), pp. 1364–1382.

[48] A. Lutz and B. Kerzin. *Barry Kerzin meditating with EEG for neuroscience research.* [Public domain] via Wikimedia Commons. 2017.

[49] M.Gazzaniga, R. Ivry, and G. Mangun. *Cognitive Neuroscience: The Biology of the Mind (Fourth Edition).* W. W. Norton & Company, 2013.

[50] J.C. Maxwell. "A Dynamical Theory of the Electromagnetic Field". In: *IPhil. Trans. R. Soc. Lond.* 155 (1865), pp. 459–512.

[51] T. Medani, D. Lautru, Z. Ren, D. Schwartz, and G. Sou. "Modelling of Brain Sources Using the Modified Saint Venant's Method in FEM Resolution of EEG Forward Problem". In: *Conference IEEE EMBS Conference on Neural Engineering 2015.* 7th International IEEE EMBS Conference on Neural Engineering. Montpellier, France, Apr. 2015.

[52] J. W. H. Meijs, O. W. Weier, M. J. Peters, and A. Van Oosterom. "On the numerical accuracy of the boundary element method (EEG application)". In: *IEEE Trans. Biomed. Eng.* 36 (1989), pp. 1038–1049. DOI: `10.1109/10.40805`.

[53] T. Miinalainen, A. Rezaei, D. Us, A. Nüßing, C. Engwer, C.H. Wolters, and S. Pursiainen. “A realistic, accurate and fast source modeling approach for the EEG forward problem”. In: *NeuroImage* 184 (2018), pp. 56–67. DOI: `https://doi.org/10.1016/j.neuroimage.2018.08.054`.

[54] R. v. Mises. “On Saint Venant’s principle”. In: *Bull. Amer. Math. Soc.* 51 (1945), pp. 555–562.

[55] M. Mommer and R. Stevenson. “A Goal-Oriented Adaptive Finite Element Method with Convergence Rates”. In: *SIAM J. Numer. Anal.* 47(2) (), pp. 861–886. DOI: `https://doi.org/10.1137/060675666`.

[56] P. Morin, R. Nochetto, and K. Siebert. “Convergence of Adaptive Finite Element Methods”. In: *SIAM Review* 44 (2002), pp. 631–658.

[57] J. De Munck, B. van Dijk, and H. Spekreijse. “Mathematical dipoles are adequate to describe realistic generators of human brain activity”. In: *IEEE Trans. Biomed. Eng.* 35(11) (1988), pp. 960–966.

[58] J. De Munck and M. Peters. “A Fast Method to Compute the Potential in the Multisphere Model”. In: *IEEE Trans. Biomed. Eng* 40(11) (1993), pp. 1166–1174.

[59] S. Murakami and Y. Okada. “Contributions of principal neocortical neurons to magnetoencephalography and electroencephalography signals”. In: *J Physiol.* 575 (2006), pp. 925–936. DOI: `10.1113/jphysiol.2006.105379`.

[60] R. Nochetto. “Why Adaptive Finite Element Methods Outperform Classical Ones”. In: *Proceedings of the International Congress of Mathematicians* (2010), pp. 2805–2833. DOI: `10.1142/9789814324359_0168`.

[61] R. Nochetto, K.G. Siebert, and A. Veeser. “Theory of adaptive finite element methods: an introduction”. In: *Multiscale, Nonlinear and Adaptive Approximation* (2009), pp. 409–542.

[62] P. Nunez. “Localization of brain activity with electroencephalography.” In: *Adv Neurol.* 54 (1990), pp. 39–65.

[63] J. Oden and J. Reddy. *An Introduction to the Mathematical Theory of Finite Elements (Dover Books on Engineering).* Dover Publications, 2012.

[64] R. Oostenveld, P. Fries, E. Maris, and J.M. Schoffelen. “FieldTrip: open source software for advanced analysis of MEG, EEG, and invasive electrophysiological data”. In: *Computational Intelligence and Neuroscience* 2011.156869 (2011), pp. 1–9.

[65] R. Pascual-Marqui. “Standardized low resolution brain electromagnetictomography (sLORETA): technical details”. In: *Methods Find Exp Clin Pharmacol.* 24 (2002), pp. 5–12.

[66] R. Pascual-Marqui, C. Michel, and D. Lehmann. "Low resolution electromagnetic tomography: a new method for localizing electrical activity in the brain". In: *Int J Psychophysiol.* 18 (1994), pp. 49–65.

[67] S. Reiter. *ProMesh – a flexible interactive meshing software for unstructured hybrid grids in 1, 2, and 3 dimensions.* In preparation.

[68] S. Reiter, A. Vogel, I. Heppner, M. Rupp, and G. Wittum. "A massively parallel geometric multigrid solver on hierarchically distributed grids". In: *Computing and Visualization in Science* 16.4 (2013), pp. 151–164. DOI: `10.1007/s00791-014-0231-x`.

[69] J. Riera, T. Ogawa, T. Goto, A. Sumiyoshi, H. Nonaka, A. Evans, H. Miyakawa, and R. Kawashima. "Pitfalls in the dipolar model for the neocortical EEG sources". In: *Journal of Neurophysiology* 108.4 (2012). PMID: 22539822, pp. 956–975. DOI: `10.1152/jn.00098.2011`.

[70] A. Rodriguez, J. Camano, R.Rodriguez, and A. Valli. "A posteriori error estimates for the prooblem of electrostatics with a dipole source". In: *Computers and Mathematics with Applications* 48 (2014), pp. 464–485. DOI: `10.1016/j.camwa.2014.06.017`.

[71] B. de Saint-Venant. *Memoire sur la torsion des prismes: avec des considérations sur leur fléxion ainsi que sur l'équilibre intérieur des solides élastiques en général, et des formules pratiques pour le calcul de leur résistance à divers efforts s'exerçant simultanément.* S.l., 1853.

[72] J. Sarvas. "Basic mathematical and electromagnetic concepts of the biomagnetic inverse problem". In: *Physics in Medicine & Biology* 32.1 (1987), p. 11.

[73] H. Si. "TetGen, a Delaunay-Based Quality Tetrahedral Mesh Generator". In: *ACM Trans. Math. Softw.* 41.2 (Feb. 2015), 11:1–11:36. DOI: `10.1145/2629697`.

[74] M. Stenroos. "Integral equations and boundary-element solution for static potential in a general piece-wise homogeneous volume conductor". In: *Physics in Medicine and Biology* 61.22 (2016), N606–N617. DOI: `10.1088/0031-9155/61/22/n606`.

[75] M. Stenroos and J. Sarvas. "Bioelectromagnetic forward problem: isolated source approach revis(it)ed". In: *Phys.Med.Biol.* 57 (2012), pp. 3517–3535.

[76] R. Stevenson. "Optimality of a standard adaptive finite element method". In: *Found. Comput. Math.* 7 (2007), pp. 245–269.

[77] G. Stodart. *Frontpiece in James Maxwell.* [Public Domain] via wikimedia commons. Source: The Scientific Papers of James Clerk Maxwell. Ed: W. D. Niven. New York: Dover, 1890. 2017.

[78] W. Tryon. *Cognitive Neuroscience and Psychotherapy: Network Principles for a Unified Theory.* Academic Press, 2014.

[79] A. Valli. "Solving an electrostatics–like problem with a current dipole source by means of the duality method". In: *Applied Mathematics Letters* 25 (2012), pp. 1410–1414.

[80] A. Vogel, S. Reiter, M. Rupp, A. Nägel, and G. Wittum. "UG 4 - A Novel Flexible Software System for Simulating PDE Based Models on High Performance Computers". In: *Computation and Visualisation in Science* (2012). submitted and accepted.

[81] J. Vorwerk. *Comparison of Numerical Approaches to ther EEG Forward Problem.* Diploma Thesis, Westfälische Wilhelms–Universität Münster. 2011.

[82] J. Vorwerk, J.-H. Cho, S. Rampp, H. Hamer, T.R. Knösche, and C.H. Wolters. "A Guideline for Head Volume Conductor Modeling in EEG and MEG." In: *NeuroImage* 100 (2014), pp. 590–607.

[83] J. Vorwerk, M. Clerc, M. Burger, and C.H.Wolters. "Comparison of Boundary Element and Finite Element Approaches to the EEG Forward Problem". In: *Biomedical Engineering* 57.Suppl.1 (2012), pp. 795–798. DOI: `10.1515/bmt-2012-4152`.

[84] J. Vorwerk, R. Oostenveld, M. Piastra, L. Magyari, and C. Wolters. "The FieldTrip-SimBio pipeline for EEG forward solutions". In: *BioMedical Engineering OnLine* 17.1 (2018), p. 37. DOI: `10.1186/s12938-018-0463-y`.

[85] C. Wolters. *Influence of Tissue Conductivity Inhomogeneity and Anisotropy on EEG/MEG based Source Localization in the Human Brain.* Vol. 39. MPI Series in Cognitive Neuroscienece. MPI of Cognitive Neuroscience, Dissertation. 2003.

[86] C. Wolters, A. Anwander, G. Berti, and U. Hartmann. "Geometry–adapted hexahedral meshes improve accuracy of finite–element–method–based EEG source analysis". In: *IEEE Transactions on Biomedical Engineering* 54 (2007), pp. 1446–1453.

[87] C. Wolters, H. Köstler, C. Möller, J. Härdtlein, and A. Anwander. "Numerical approaches for dipole modeling in finite element method based source analysis". In: *International Congress Series* 1300 (2007), pp. 189–197.

[88] C. Wolters, H. Köstler, C. Möller, J. Härdtlein, L. Grasedyck, and W. Hackbusch. "Numerical Mathematics of the Subtraction Method for the Modeling of a current Dipole in EEG Source Reconstruction using Finite Element Head Models". In: *SIAM J of Sci.Comp* 30 (2007), pp. 24–25.